eXPRESS Polymer Letters Vol.6, No.2 (2012) 95
Available online at www.expresspolymlett.com
DOI: 10.3144/expresspolymlett.2012.10

Editorial corner – a personal view
Sunlight stimulated repeated self-healing

*M. Q. Zhang**

Materials Science Institute, Sun Yat-sen (Zhongshan) University, Guangzhou 510275, P. R. China

The sun provides limitless power for earth. Solar energy has been harnessed in many aspects. For example, plants live on photosynthesis induced by sunlight. With respect to the products made from polymers, however, sunlight is recognized to be an undesirable factor responsible for aging.

Fortunately, anything which is negative can be turned to positive. In case photoreversible bonds are introduced to macromolecular chains, damages in polymers can be self-healed under sunlight stimulus. Because the use of light is clean, cheap and readily available, such an unconscious way of remending is obviously advantageous.

In a recent proof-of-concept experiment of our laboratory [J. Mater. Chem., DOI: 10.1039/C1JM13467A], a novel coumarin derivative was synthesized and attached to a conventional covalently bonded polymer (i.e. polyurethane) as photosensitive crosslinker. Upon mechanical damage, the crosslinkages (i.e. coumarin dimers) of polyurethane network preferentially cleave returning to original coumarin moieties. Then, these coumarin moieties can be reconnected by illumination of 350 nm UV light (a major component of sunlight). The entire cycle is fully reversible. By using this habit, broken polyurethane are repeatedly re-bonded under sunlight, without the necessity of any catalyst, healing agent or surface treatment.

The research on photochemical self-healing has only just begun and is still in infancy. In principle, reversible photochemical reaction is hard to proceed in solid polymer for structural application because molecular motion is restricted. The key issues seem to be that (i) the photosensitive segments on the fractured surface should be mobile enough, which favors wetting and diffusion of molecules at the solid-solid contact of the damaged parts to meet the molecular level movement requirement of crack healing; and (ii) macroscopic flow of the material should be prohibited during crack healing, maintaining load-bearing capacity of the material.

Repeated damages are very common in daily life, like scratches on cars made by automatic brush washing and those on touch screens by fingernails. Although exterior paint that obscures scratches was developed by automotive industry, it works due to heating of the sun rather than photochemistry. Only fine scratches appearing in the form of plastic deformation can be recovered. In contrast, the sun stimulated photoreversible reaction is able to rebond completely damaged polymeric materials, despite the healing efficiency in terms of mechanical strength restoration is not that satisfactory for the moment. Evidently, the strategy is promising for developing a variety of next generation coatings, films and sheets to meet aesthetic, structural and functional requirements.

Prof. Dr. Ming Qiu Zhang
Member of International Advisory Board

*Corresponding author, e-mail: ceszmq@mail.sysu.edu.cn

eXPRESS Polymer Letters Vol.6, No.2 (2012) 96–106
Available online at www.expresspolymlett.com
DOI: 10.3144/expresspolymlett.2012.11

Mechanical properties of PET composites using multi-walled carbon nanotubes functionalized by inorganic and itaconic acids

A. May-Pat[1*], *F. Avilés*[1], *P. Toro*[2], *M. Yazdani-Pedram*[3], *J. V. Cauich-Rodríguez*[1]

[1]Centro de Investigación Científica de Yucatán, A.C., Unidad de Materiales, Calle 43 # 130, Col. Chuburná de Hidalgo, 97200, Mérida, Yucatán, México
[2]Facultad de Ciencias Físicas y Matemáticas, Universidad de Chile, Santiago, Chile
[3]Facultad de Ciencias Químicas y Farmacéuticas, Universidad de Chile, Santiago, Chile

Received 13 June 2011; accepted in revised form 18 August 2011

Abstract. Multi-walled carbon nanotubes (MWCNTs) were oxidized by two different acid treatments and further functionalized with itaconic acid (IA). The functionalized MWCNTs were used to fabricate Poly(ethylene terephthalate) (PET) composites by melt mixing. The presence of functional groups on the surface of the treated MWCNTs was confirmed by infrared spectroscopy and thermogravimetric analysis. The MWCNTs oxidized with a concentrated mixture of HNO_3 and H_2SO_4 exhibited more oxygen containing functional groups (OH, COOH) but also suffer larger structural degradation than those oxidized by a mild treatment based on diluted HNO_3 followed by H_2O_2. PET composites were fabricated using the oxidized-only and oxidized followed by functionalization with IA MWCNTs. PET composites fabricated with MWCNT oxidized by mild conditions showed improved tensile strength and failure strain, while harsh MWCNT oxidation render them overly brittle.

Keywords: *polymer composites, nanocomposites, mechanical properties, MWCNTs, itaconic acid*

1. Introduction

Poly(ethylene terephthalate) (PET) is a semicrystalline polymer which has good mechanical properties, chemical resistance, thermal stability, melt viscosity, and spinnability (ability to be spun, e.g. in the form of fibers). PET has been used in diverse fields such as food packaging, film technology, automotive, electrical, beverages and containers, and textile fiber industries, and even in the biomedical field as Dacron [1, 2]. A way to further improve the properties of this commodity polymer is through the formation of a nanocomposite, which can be achieved by the addition of nanoclays, carbon nanotubes or other nanostructures. Nanocomposite materials often possess a combination of physical properties that are not present in conventional polymer matrix composites. Because of their high aspect ratios, adding low concentrations of carbon nanotubes (CNTs) into a polymer matrix can improve the mechanical, thermomechanical and electrical properties of these polymer composite materials [3, 4]. Two key issues necessary to achieve superior performance in CNT filled polymer composites are an homogeneous distribution and dispersion of the CNTs inside the polymer matrix and a strong interaction between the CNTs and matrix. One of the most common methods used to disperse CNTs in a thermoplastic polymer matrix is melt blending [5]. Melt blending is a convenient method to produce CNT based composites given its cost effectiveness

*Corresponding author, e-mail: amay@cicy.mx

and ease of production, with the additional advantage of being a solvent-free process [6, 7]. The use of this polymer processing technique to fabricate CNT-polymer composites has been reported for a large variety of polymers, including PMMA, polyolefins (PE, PP), polyamides, polyesters (PET, PBT), polyurethanes, and polystyrene [8–10]. Melt blending, however, may be limited to low CNT concentrations due to the high viscosity of the composites at high nanotube loadings and problems of dispersing the nanotubes for high CNT concentrations [11]. Regarding the issue of promoting interfacial interactions between the CNT and thermoplastic polymer matrices, the most common procedures used for covalent attachment of reactive groups to the CNT surface are treatments based on inorganic acids [5, 12]. Usually, the nanotubes are refluxed with a nitric acid solution or a mixture of nitric and sulfuric acid, sometimes concurrently with the application of high power sonication [5, 13, 14]. These oxidative treatments usually result in formation of surface reactive groups, such as hydroxyl, carbonyl and carboxylic acid, with the drawback of producing CNT structural damage and length shortening [15]. Oxidation of multiwalled carbon nanotubes (MWCNTs) starts at the tips and gradually moves towards the central part of the tube, but, if the acid concentration is too high or the exposure time is long, some of the layers can be substantially roughened or even removed successively [15–17]. Another method which has been less explored to promote chemical bonding between CNTs and thermoplastic polymers is CNT functionalization with organic acids [18, 19]. For the case of MWCNT/PET composites, only scant research has been conducted on the functionalization of carbon nanotubes with organic acids and compounds [20–22]. Jin and coworkers [21] functionalized MWCNTs with acetic anhydride, which resulted in good dispersion of MWCNTs in a PET matrix, as well as an increased tensile strength and elastic modulus. Yoo *et al*. [22] functionalized MWCNTs with benzyl and phenyl isocyanates, and found that the resulting nanocomposites showed improved dispersion of nanotubes in the PET matrix. Improved mechanical properties were found in the nanocomposites fabricated with MWCNT-phenyl isocyanate because of the favorable presence of π–π interaction. Regarding itaconic acid, this organic compound has been used as compatibilizer for blends of thermoplastic polymers [23, 24]. Yazdani-Pedram *et al.* [23] used PP functionalized with itaconic acid as compatibilizer in blends of PP/PET. They found that the presence of modified PP improves the tensile mechanical properties of PP/PET blends. Sailaja and Seetharamu [24] used grafted low density polyethylene (LDPE) with itaconic acid in mixtures of LDPE/starch and found that LDPE/starch blends compatibilized by itaconic acid exhibited better mechanical properties as compared to their uncompatibilized counterparts. Research on functionalization of CNTs with itaconic acid for polymer composites was not found in the literature search conducted by the authors.

Therefore, the aim of the present work is to modify the surface of MWCNTs by the introduction of hydroxyl groups through treatments based on nitric and sulfuric acids, as well as itaconic acid (IA). In particular, the influence of a mild and an aggressive acid oxidation and the effect of a subsequent functionalization of the MWCNTs with IA on the tensile mechanical properties of MWCNT/PET composites is investigated.

2. Materials and methods

2.1. Materials

The MWCNTs used in this work were purchased from Bayer MaterialScience (Leverkusen, Germany). The CNT product (Baytubes C150P®) consist of MWCNTs synthesized by chemical vapor deposition with high purity (~95%), an outer mean diameter of 13–16 nm, inner diameter of ~4 nm and average length of 1–4 μm [15]. Nitric acid (HNO_3, 68% v/v), sulfuric acid (H_2SO_4, 98% v/v) and itaconic acid were purchased from Sigma Aldrich Corporation (Milwaukee, USA). The polymer used in this work is CLEARTUF 8006 Polyester Resin ('M & G Group' Polymers USA, LLC). CLEARTUF 8006 is a high molecular weight polyethylene terephthalate thermoplastic polymer with intrinsic viscosity of 0.80 dl/g and a melting point of 250°C.

2.2. Oxidation of MWCNTs

Chemical oxidation was carried out using two acid treatments, one ('mild') which is expected to be gentle with the MWCNTs surface and cause minimum structural damage and a second one which is significantly more aggressive. The 'mild' treatment consisted of oxidizing the nanotubes with nitric

Table 1. Identification of chemical treatments investigated in this work

Label	Treatment
A	Untreated (as-received)
B	HNO_3 (3.0 M) followed by H_2O_2 (30% v/v)
C	Mixture of HNO_3 (68% v/v) and H_2SO_4 (98% v/v)
D	Treatment B + Itaconic acid
E	Treatment C + Itaconic acid

acid (3.0 M) followed by hydrogen peroxide [14]. The 'aggressive' treatment was conducted using a concentrated combination of nitric (68% v/v) and sulfuric (98% v/v) acids. Table 1 illustrates the treatments carried out. Label 'A' is used for as-received (untreated) MWCNTs, taken as a reference. Treatment 'B' is used for MWCNTs treated with nitric acid (3.0 M) followed by H_2O_2. This treatment was conducted by mechanically stirring the CNTs in the nitric acid for 15 min, and then sonicating the CNTs/HNO_3 solution for 2 h in a conventional ultrasonic bath. After exhaustive washing of the CNTs with distilled water, the nitric acid was replaced with hydrogen peroxide (30% v/v) and the process was repeated. For treatment 'C', the as-received MWCNTs were mixed with sulfuric (20 ml) and nitric (20 ml) acids, in concentrations of 98 and 68% v/v respectively, and initially sonicated for 10 min. The mixture was then refluxed for 1 h at 140°C. Acid oxidized MWCNTs were finally obtained by washing and filtering the mixture with distilled water and then drying in a vacuum oven at 60°C for 48 h.

2.3. Functionalization with itaconic acid

The oxidized MWCNTs (treatments B and C in Table 1) were further functionalized with itaconic acid as follows. First, oxidized MWCNTs were dispersed in 20 ml of acetone for 10 min in a conventional ultrasonic bath. After 10 min, itaconic acid (3.0 g), p-toluenesulfonic acid as catalyst (0.2 g) and 80 ml of acetone were added to the initial MWCNT/acetone mixture and stirred under reflux for 3 h at 60°C. After this, the functionalized nanotubes were washed, filtered with acetone and then dried at 60°C in a vacuum oven to constant weight. An identical procedure with IA was conducted for MWCNTs that were previously oxidized by treatments B and C. The MWCNTs functionalized by IA that had been previously oxidized by treatment B were labeled as 'D', while those that were previously oxidized by treatment C were labeled as 'E' (see Table 1). A schematic of the proposed reaction between the CNT, IA and PET is shown in Figure 1. Overall, it is expected that the COOH groups generated on the CNT surface are more prone to form strong bonding with the C=O groups of PET than the OH ones, due to their ability to induce dimer formation. However, ester formation is also possible.

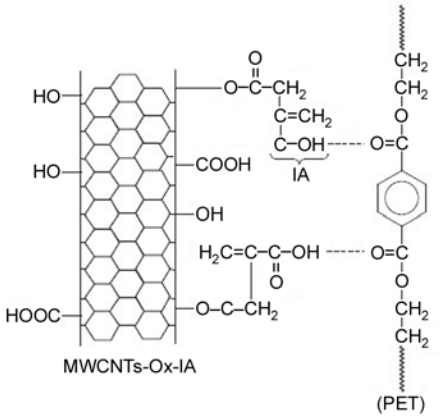

Figure 1. Proposed reaction between IA, MWCNTs and PET

2.4. Preparation of MWCNT/PET composites

MWCNT/PET composites were fabricated by melt blending. Initially, PET powder was dried at 120°C for 24 h in a convection oven. Nanocomposites of 0.5 wt% were prepared by melt mixing the MWCNTs and PET powder in a Banbury mixing chamber (Plasticorder PL330, G.W. Brabender, Hackensack, NJ, USA.), with a volumetric capacity of 50 cm^3 at 250°C. The mixing process was performed in two continuous steps. First, the MWCNT/PETs powder material was placed inside the chamber and mixed for 5 min at 20 rpm. The mixing speed was then increased to 60 rpm for 5 min more. The PET/MWCNTs composite material was then laminated by compression molding into thin sheets of 110 × 110 × 1.0 mm. The lamination process was performed at 270°C in a laboratory press with temperature control (Carver Laboratory Press) using 2 tons of pressure for 20 min and then water-cooled down to room temperature. After lamination, dog-bone-shaped tensile samples were cut from the 1 mm thick sheet with the geometry according to ASTM D638 standard [25].

2.5. Characterization

2.5.1. Characterization of functionalized MWCNTs

Infrared spectroscopy of as-received and chemically functionalized MWCNTs was conducted using a Fourier transform infrared spectrometer (FT-IR) Nicolet-Protege 460, in the spectral range from 4000 to 500 cm^{-1}. FT-IR spectra were obtained using KBr discs containing a very small amount of MWCNTs.

Thermogravimetric analysis (TGA) was conducted in nitrogen atmosphere with a heating rate of 10°C/min using a Perkin–Elmer TGA7 equipment within a temperature range of 50–750°C. The TGA was repeated three times to yield reproducible results.

The morphology of the acid-MWCNTs was observed using an FEI-TITAN transmission electron microscope (TEM) operated at 300 kV and registered near the Scherzer focus. TEM samples were prepared on lacey carbon grids using dispersion in an ultrasonic bath for 30 minutes.

2.5.2. Characterization of nanocomposites

Tensile properties of MWCNT/PETs composites were determined according to the ASTM D638 standard using type IV specimens [25]. Tensile tests were conducted in a Shimadzu AGI-100 universal testing machine equipped with a 500 N load cell and using a cross-head speed of 5 mm/min. Ten replicates for each nanocomposite material investigated were tested.

The fracture surfaces specimens of the tested nanocomposites were examined by using a JEOL 6360LV scanning electron microscope (SEM), after coating the surface with a thin layer of gold.

3. Results and discussion

3.1. Characterization of MWCNTs

3.1.1. FT-IR spectroscopy

FTIR spectroscopy was used to confirm the presence of hydroxyl, carboxyl as well as itaconic acid units on the surface of MWCNTs. As seen in Figure 2A, the IR spectrum of as-received MWCNTs shows characteristic bands due to O–H stretching vibration at 3440 cm^{-1}, C=C stretching at 1629 cm^{-1} as well as O–H bending (~1400 cm^{-1}) and C–O stretching (~1116 cm^{-1}). The spectrum of oxidized MWCNTs by using the mild treatment (Figure 2B) shows additional absorption bands at 1736 cm^{-1} due to carbonyl stretching vibration of hydrogen bonded –COOH groups as well as an increase of the relative intensity of OH groups, confirming the presence of different type of hydroxyl groups on the surface of the MWCNTs. The spectrum of MWCNTs oxidized by treatment C (Figure 2C) is similar to that of the mild treatment (Figure 2B) but the band corresponding to C–O stretching is more intense and better resolved. This suggests that although the same functional groups are generated for both oxidation treatments (B and C), a larger number of such functional groups should be present in the MWCNTs oxidized by the method C. Functionalization of oxidized MWCNTs by itaconic acid (Figures 2D and 2E) show an increase in the relative intensity of the band in the region 3130 cm^{-1} due to –OH groups. The C=O absorption bands characteristic of carboxyl functional groups (–COOH) of itaconic acid is now markedly observed around 1707–1730 cm^{-1}, which confirm the success of the functionalization treatment with itaconic acid.

3.1.2. Thermogravimetric analysis

TGA in nitrogen atmosphere was conducted for all MWCNTs examined in Table 1, as well as for IA. The thermograms obtained are presented in Figure 3. It is observed that the most thermally stable material is the as-received MWCNTs (A), which loses only about 1% weight after being heated to 750°C. This high thermal stability is due to the low content of amorphous carbon in the as-received material. When a mild oxidation is conducted on the MWCNTs (B), the amount and rate of weight loss is very similar to that of the as-received material, indicating that no or very few amorphous carbon has been generated because of the acid treatment. The harsh oxidation treatment (C), on the other hand, significantly degrades the graphitic structure of the MWCNTs by converting it to amorphous carbon, which is evident by the pronounced weight loss observed early in its TGA curve. Below 150°C evaporation of adsorbed water is expected. The pronounced weight loss observed between ~150 and 350°C are attributed to elimination of hydroxyl and carboxylic functionalities present on the surface of the oxidized MWCNT probably due to dehydration and decarboxilation [16, 17]. The fact that the weight loss in this temperature range is markedly greater

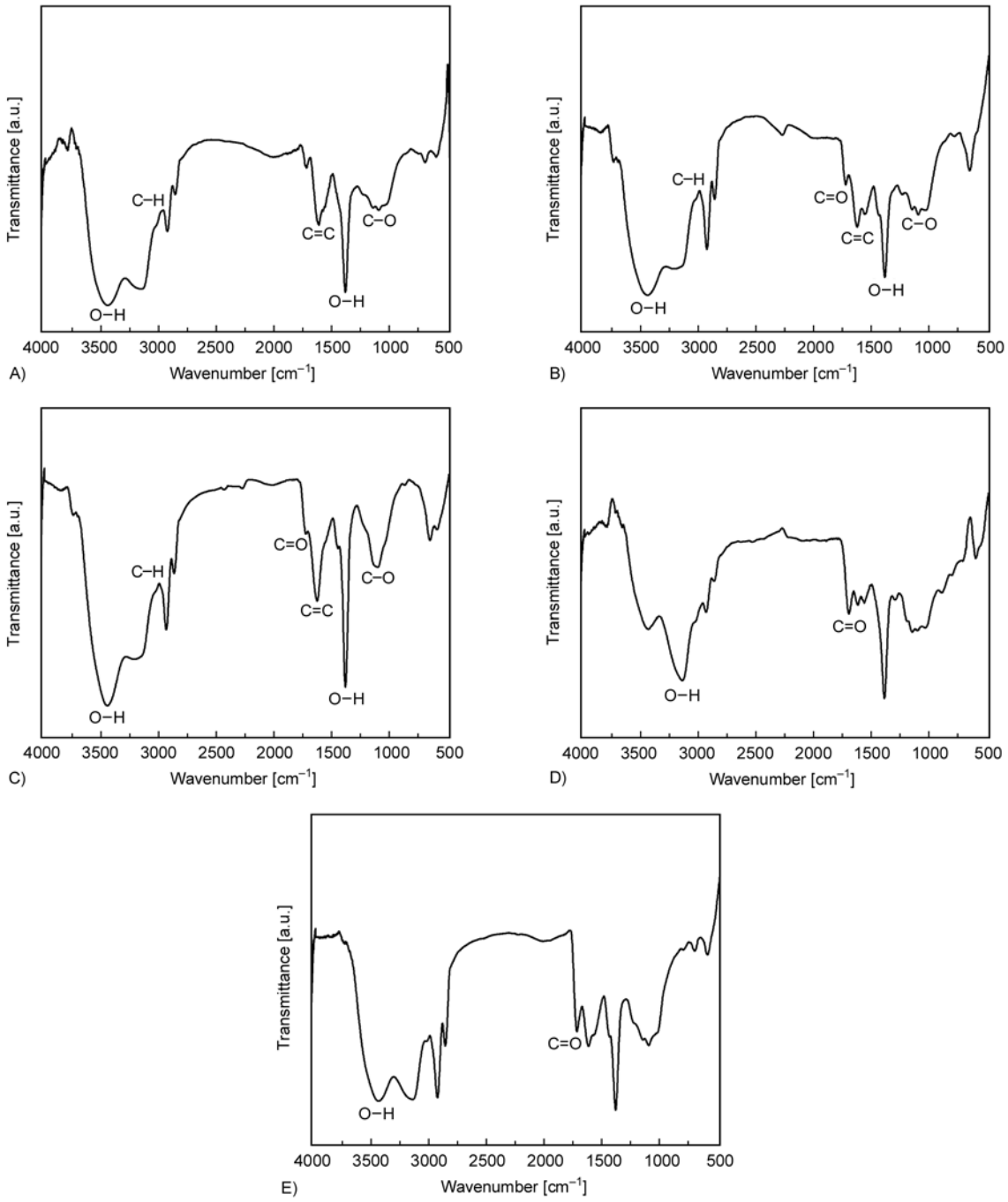

Figure 2. FT-IR spectra of MWCNTs. Treatment A, B, C, D and E refer to Table 1.

for sample C than B indicates that a larger number of functionalities are present in the MWCNTs oxidized by the aggressive treatment, with respect to the ones oxidized under mild conditions. For temperatures above 350°C, a large amount of weight is lost by MWCNTs oxidized by treatment C, which indicates that this treatment has converted part of the CNT graphitic structure to amorphous carbon, which is thermally oxidized slightly above 350°C.

The MWCNTs that were functionalized by IA after oxidation present a distinctive behavior. For the MWCNTs previously oxidized by treatment B and then functionalized by IA (D), a marked weight loss occurs around 200°C, which matches with the decomposition of the IA (see curve for IA in Figure 3). After thermal decomposition of the IA bonded to the CNT, the curve of sample D follows a slope (rate of weight loss) similar to that of the

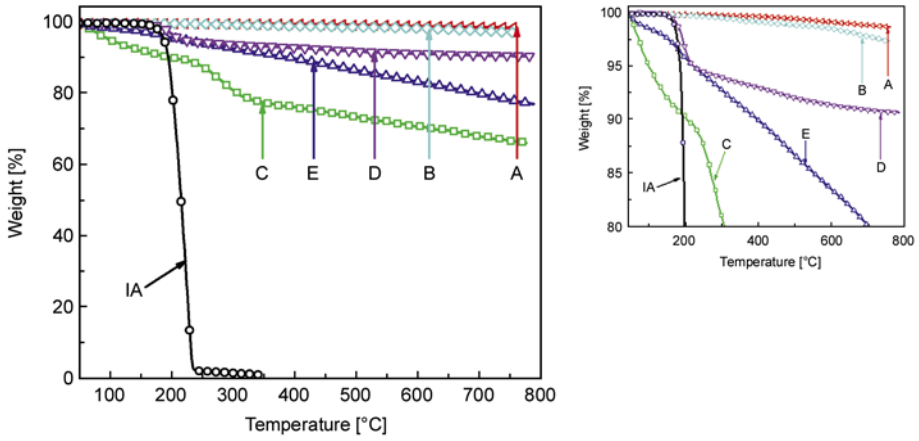

Figure 3. TGA curves of MWCNTs samples. Labels refer to Table 1.

curve corresponding to the sample that was only oxidized with the same treatment (B). The behavior of the MWCNTs that were functionalized with IA after oxidation with an aggressive acid treatment (samples E) was different. In this case, a larger weight loss was observed with respect to samples oxidized by treatment D for all temperature ranges examined. The rate of weight loss (slope of the curve) is markedly smaller for samples E than for C before 350°C, but after 350°C both slopes were similar. The smaller mass loss of sample E compared to sample C may suggest that some of the amorphous carbon generated during the harsh CNT oxidation by method C is physically removed during the subsequent treatment with IA. This will be further examined in connection to the mechanical properties of the composites in section 3.2.1.

Therefore, from the TGA analysis it is concluded that an aggressive acid oxidation treatment (such as C) generates a larger concentration of functional groups on the surface of the MWCNTs with respect to a milder oxidation treatment (B), but also destroys a great deal of the graphitic structure converting it to amorphous carbon. The TGA curves of MWCNTs that were functionalized with IA confirm the presence of IA on the CNT, which is indicative of an adequate functionalization process.

3.1.3. Transmission electron microscopy

TEM analysis of the as-received (A) and oxidized samples (B and C) is shown in Figure 4. No images are presented for treatments with IA since no new particular features are expected after functionalization with IA. Figure 4a reveals the morphology of an individual as-received multi-walled carbon nanotube. The as-received material is featured by the characteristic graphitic layers arranged in a coaxial cylindrical fashion. Some amorphous carbon is observed at the outermost layers and structural defects are also present in the as-received material. The morphology of the MWCNTs oxidized by a sequential treatment based on diluted HNO_3 followed by H_2O_2 (treatment B, Figure 4b) is similar to that of the as-received MWCNTs, indicating that structural damage is either absent or small. For the MWCNTs oxidized by the concentrated mixture of HNO_3 and H_2SO_4 (treatment C), the CNTs exhibit severe structural damage, as shown in Figure 4c. This concentrated mixture of acids causes conversion of the original graphitic structure to amorphous carbon with the consequent increase in CNT roughness and waviness as observed in Figure 4c. In this case, the damage reaches even the inner nanotube walls. Treating the MWCNTs with a concentrated mixture of HNO_3 and H_2SO_4 causes severe etching of the graphitic surface of the CNT, leading to defective tubes with a large population of disordered sites and amorphous carbon. These TEM observations are consistent with the thermal degradation evidenced by the thermogram of treatment C in Figure 3. On the other hand, the MWCNT oxidation with a mild treatment such as B yielded no or few structural damage, which is also consistent with the TGA findings. However, FT-IR analysis (Figure 2) suggests that more functional groups are present on MWCNTs oxidized by treatment C than for B. For the improvement of the composite mechanical properties, structurally pristine CNTs with a large density of functionalities are desirable. In our case, MWCNTs oxidized by treatment C have a large

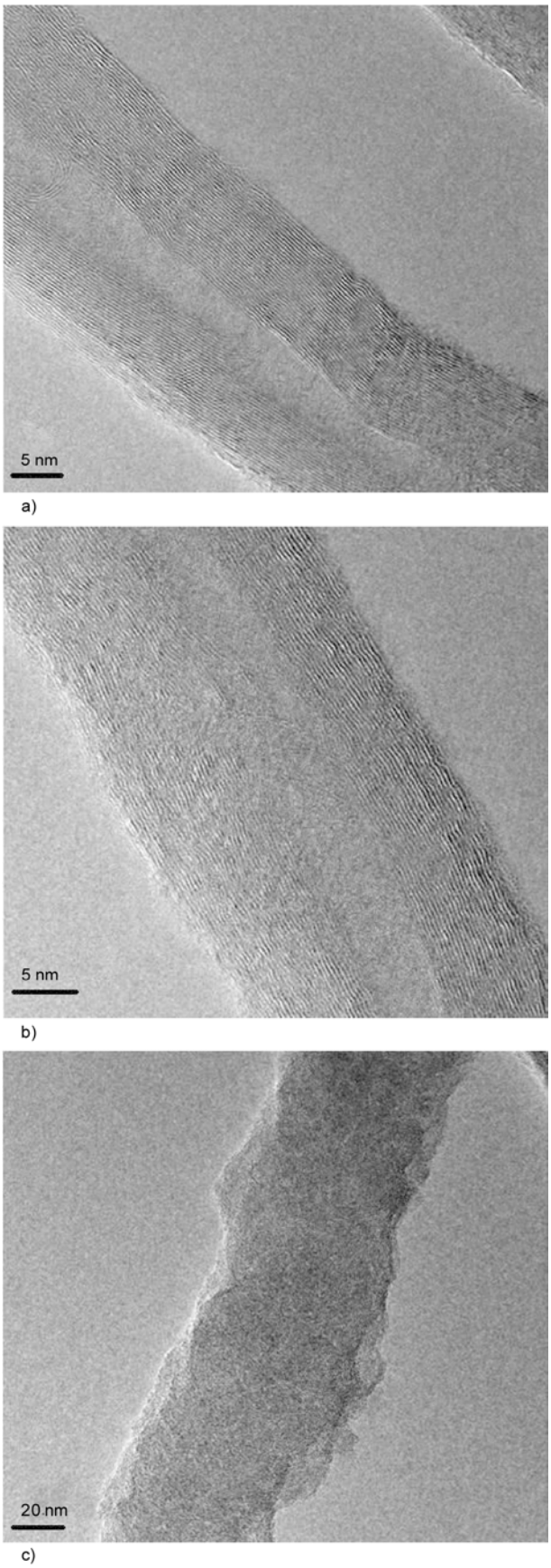

Figure 4. TEM of MWCNTs. a) As-received (A), b) oxidized by HNO_3 followed by H_2O_2 (B), c) oxidized by a concentrated mixture of HNO_3 and H_2SO_4 (C).

number of OH and COOH functionalities, but also are severely damaged. On the other hand, the MWCNTs oxidized by treatment B were not severely damaged by the oxidizing treatment, but they also have less density of functional groups than those oxidized by treatment C. The effect of these competing factors on the mechanical properties of the composites fabricated with these MWCNTs will be examined in the next section.

3.2. Characterization of nanocomposites

3.2.1. Tensile properties

The tensile stress-strain curves of pure PET and the examined MWCNT/PET composites at 0.5 wt% loading are presented in Figure 5. Table 2 presents a summary of the measured mechanical properties, where average and standard deviations are reported. The stress-strain curves and measured mechanical properties (Table 2) are similar for MWCNT/PET composites which used as-received MWCNTs (MWCNT/PETs-A) to those of PET, motivating the need of CNT functionalization. The absence of significant improvements in the mechanical properties

Table 2. Mechanical properties of tested MWCNT/PET composites

Sample	Tensile strength [MPa]	Elastic modulus [GPa]	Failure strain [%]
PET	33.9±7.06	1.54±0.04	2.22±0.49
MWCNT/PETs-A	34.1±6.48	1.47±0.09	2.35±0.43
MWCNT/PETs-B	50.0±5.30	1.58±0.06	3.45±0.45
MWCNT/PETs-C	–	–	–
MWCNT/PETs-D	23.4±6.32	1.39±0.15	2.40±0.93
MWCNT/PETs-E	26.9±5.16	1.48±0.14	2.43±0.72

– = Not possible to measure

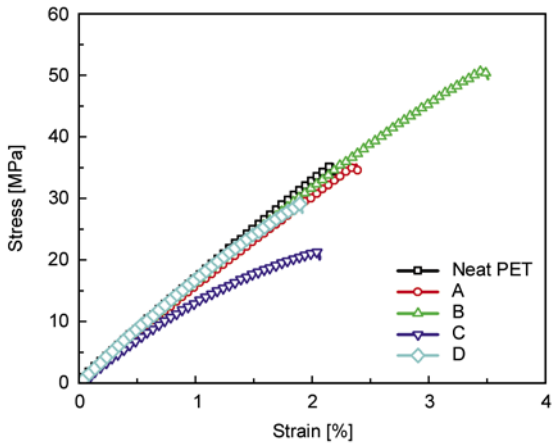

Figure 5. Representatives stress-strain curves for PET and PET nanocomposites. Labels A to E refer to Table 1.

of the as-received CNT composites may be the result of aggregation, as well as poor interfacial interaction between the as-received MWCNTs and PET. Quite different properties are obtained for the composites whose CNTs were only oxidized by HNO_3 followed by H_2O_2 (MWCNT/PETs-B). With respect to neat PET, these composites showed an increase in the strength and failure strain of 47 and 55% (based on averages) respectively, although the improvement in elastic modulus may not be statistically significant. The large improvement in the tensile properties of the MWCNT/PETs-B composites is attributed to the improved dispersion of MWCNTs inside the matrix (which will be further examined by SEM) and improved interactions between the MWCNTs and PET mostly by hydrogen bonding, enhancing the interfacial bonding. The PET-composites that utilized MWCNTs treated by the concentrated mixture of nitric and sulphuric acids (treatment C) were not possible to manufacture in the form of tensile coupons (indicated by dash lines in Table 2). These composites were very brittle and cracked in many pieces immediately after releasing from the press used for compression molding. This behavior, which was very distinctive from the rest of the composites, confirms that the MWCNTs treated by treatment C contain a large number of (COOH) functionalities and that such functionalities are interacting with the PET matrix (through C=O) to render the composites increased brittleness and affecting its processability. These composites may also be more thermally conductive (which influence the processing parameters), since it has been shown that MWCNTs treated by strong mixtures of nitric and sulfuric acids generate a large number of hydroxyl and carboxyl functional groups which increases the thermal conductivity of the CNTs and their composites [26]. The nucleating effect of the functionalized nanotubes during the PET melt compounding [27] may also be a contributing factor for its brittleness.

The composites prepared with IA-functionalized MWCNTs (D and E) did not show improvements in their mechanical properties with respect to the neat PET. With respect to PET, the tensile strength of both composites (D and E) reduced, and the elastic modulus and failure strain remained practically unchanged, see Table 2. The decrease in tensile strength (and decreasing trend in elastic modulus)

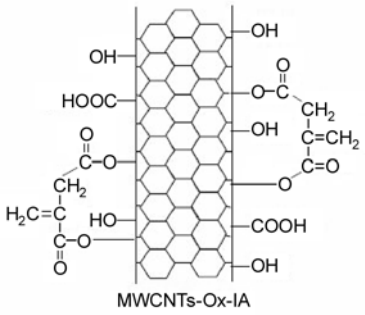

Figure 6. Possible ester formation on IA functionalized MWCNTs

of these composites could be explained by reduced interactions between the functionalized CNTs and the PET matrix and the presence of agglomerations. This would mean that a second scenario to that initially proposed in Figure 1, is also possible, which is depicted in Figure 6. Accordingly, the itaconic acid may react with the hydroxyl groups present on the acid oxidized surface of the CNT by forming ester bonds. This reduces the effective number of hydroxyl functionalities available for bonding the CNT to the polymer, leaving a hydrophobic CNT which is difficult to disperse in the hydrophilic PET.

3.2.2. Scanning electron microscopy

Figure 7 shows SEM fracture surfaces of MWCNT/PET composites whose CNTs were functionalized by treatments A, B, D and E. The CNTs seem moderately well dispersed in all composites in Figure 7. Although clear differences are difficult to discern among the figures, some particular features were observed depending on the treatment. For the non-treated composites (MWCNT/PETs-A), Figure 7a, a few small aggregates of MWCNTs appeared systematically during the SEM analysis. For this composite, MWCNTs are also seen protruding the fracture plane (plane of the SEM image) suggesting a large occurrence of CNT pullout, which is consistent with a weak interfacial bonding between the nanotubes and PET. The scenario was different for MWCNT/PETs-B composites, Figure 7b. For these composites, imaging the MWCNTs in the composite was markedly more difficult than for the rest of the samples, and the few CNTs that could be imaged appeared covered by the polymer, as seen in Figure 7b. We believe that this particular feature relates to a better dispersion into the PET matrix, as a consequence of the oxidative treatment used. MWCNTs

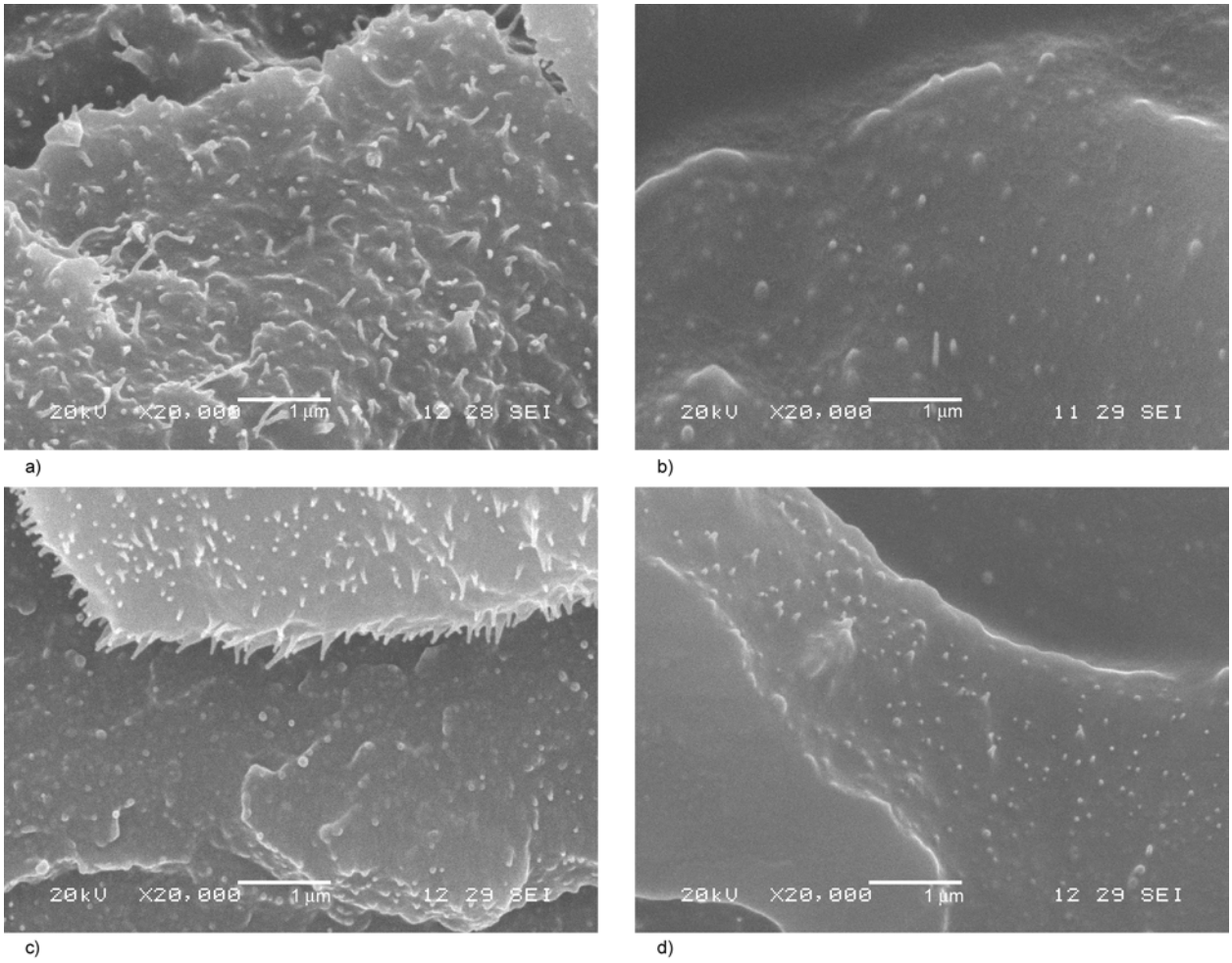

Figure 7. SEM images of fractured nanocomposites. (a) MWCNT/PETs-A, (b) MWCNT/PETs-B, (c) MWCNT/PETs-D, (d) MWCNT/PETs-E. Labels refer to Table 2.

oxidized by treatment B also appeared wrapped by the PET matrix, which suggests good interfacial bonding. This finding is consistent with the results of the tensile tests, where enhanced mechanical properties were obtained for this treatment. Figures 7c and 7d show fracture surfaces of MWCNT/PET composites which used MWCNTs functionalized by IA after acid oxidation by mild (Figure 7c) and harsh (Figure 7d) conditions (treatments D and E in Table 2). For both cases, MWCNTs are seen clearly and moderately well dispersed into the PET matrix, but not covered by the polymer as in the case of Figure 7b.

4. Conclusions

The influence of two acid oxidation methods and further functionalization with itaconic acid to functionalize the surface of MWCNTs and improve the mechanical properties of PET composites has been examined. Two routes for acid oxidations employing inorganic acids were examined, a mild one based on a sequential treatment of diluted nitric acid and hydrogen peroxide, and an aggressive one based on a concentrated mixture of nitric and sulfuric acids. Oxidizing by the mild experimental conditions proposed herein generate hydroxyl and carboxyl functional groups on the CNT surface with minimum CNT damage, which produces enhanced mechanical properties of MWCNT/PET composites. When the oxidation uses concentrated acids, a larger density of functional groups is generated, with the concomitant damage of the CNT structure. The composites manufactured using the MWCNTs oxidized by this aggressive route are overly brittle, to the extent that compromises its practical use.

For PET composites, sequential functionalization of the MWCNTs with IA after CNT oxidation is not recommended, since the OH groups of the IA may bond to similar acidic groups existent on the oxidized MWCNTs, reducing the density of function-

alities available on the MWCNT surface for hydrogen bonding with the ester groups of PET. A simple oxidation of the MWCNTs using nitric acid and hydrogen peroxide in mild experimental conditions is enough to significantly improve the tensile properties of the composite.

Acknowledgements

This work is part of an international project between Mexico and Chile (CIAM) sponsored by CONACYT-Mexico (projects No. 105567 and 79609) and CONICYT-Chile (project FONDECYT No.1090260). The authors also wish to thank Santiago Duarte and Dr. Arturo Ponce for the SEM and TEM analyses.

References

[1] Van Krevelen D. W.: Properties of polymers, Elsevier, Amsterdam (1997).

[2] Cowie J. M. G.: Polymers: chemistry and physics of modern materials. Taylor and Francis Group, Boca Raton (2008).

[3] Kim J. K., Park H. S., Kim S. H.: Multiwall-carbon-nanotube-reinforced poly(ethylene terephthalate) nanocomposites by melt compounding. Journal of Applied Polymer Science, **103**, 1450–1457 (2007).
DOI: 10.1002/app.25377

[4] Zhu Z., Wang R., Dong Z., Huang X., Zhang D.: Morphology, crystallization, and mechanical properties of poly(ethylene terephthalate)/multiwalled carbon nanotubes composites. Journal of Applied Polymer Science, **120**, 3460–3468 (2011).
DOI: 10.1002/app.33438

[5] Ma P-C., Siddiqui N. A., Marom G., Kim J-K.: Dispersion and functionalization of carbon nanotubes for polymer-based nanocomposites: A review. Composites Part A: Applied Science and Manufacturing, **41**, 1345–1367 (2010).
DOI: 10.1016/j.compositesa.2010.07.003

[6] Jin Z., Pramoda K. P., Goh S. H., Xu G.: Poly(vinylidene fluoride)-assisted melt-blending of multi-walled carbon nanotube/poly(methyl methacrylate) composites. Materials Research Bulletin, **37**, 271–278 (2002).
DOI: 10.1016/S0025-5408(01)00775-9

[7] Anoop A. K., Agarwal U. S., Rani J.: Carbon nanotubes-reinforced PET nanocomposite by melt-compounding. Journal of Applied Polymer Science, **104**, 3090–3095 (2007).
DOI: 10.1002/app.25674

[8] Du J-H., Bai J., Cheng H-M.: The present status and key problems of carbon nanotube based polymer composites. Express Polymer Letters, **1**, 253–273 (2007).
DOI: 10.3144/expresspolymlett.2007.39

[9] Sorrentino A., Vertuccio L., Vittoria V.: Influence of multi-walled carbon nanotubes on the β form crystallization of syndiotactic polystyrene at low temperature. Express Polymer Letters, **4**, 339–345 (2010).
DOI: 10.3144/expresspolymlett.2010.43

[10] Jin Z., Pramoda K. P., Xu G., Goh S. H.: Dynamic mechanical behavior of melt-processed multi-walled carbon nanotube/poly(methyl methacrylate) composites. Chemical Physics Letters, **337**, 43–47 (2001).
DOI: 10.1016/S0009-2614(01)00186-5

[11] Bikiaris D., Vassiliou A., Chrissafis K., Paraskevopoulos K. M., Jannakoudakis A., Docoslis A.: Effect of acid treated multi-walled carbon nanotubes on the mechanical, permeability, thermal properties and thermo-oxidative stability of isotactic polypropylene. Polymer Degradation and Stability, **93**, 952–967 (2008).
DOI: 10.1016/j.polymdegradstab.2008.01.033

[12] Pötschke P., Bhattacharyya A. R., Janke A.: Carbon nanotube-filled polycarbonate composites produced by melt mixing and their use in blends with polyethylene. Carbon, **42**, 965–969 (2004).
DOI: 10.1016/j.carbon.2003.12.001

[13] Saito T., Matsushige K., Tanaka K.: Chemical treatment and modification of multi-walled carbon nanotubes. Physica B: Condensed Matter, **323**, 280–283 (2002).
DOI: 10.1016/S0921-4526(02)00999-7

[14] Avilés F., Cauich-Rodríguez J. V., Moo-Tah L., May-Pat A., Vargas-Coronado R.: Evaluation of mild acid oxidation treatments for MWCNT functionalization. Carbon, **47**, 2970–2975 (2009).
DOI: 10.1016/j.carbon.2009.06.044

[15] Avilés F., Ponce A., Cauich-Rodríguez J. V., Martínez G. T.: TEM examination of MWCNTs oxidized by mild experimental conditions. Fullerenes, Nanotubes and Carbon Nanostructures, **20**, 49–55 (2012).
DOI: 10.1080/1536383X.2010.533308

[16] Datsyuk V., Kalyva M., Papagelis K., Parthenios J., Tasis D., Siokou A., Kallitsis I., Galiotis C.: Chemical oxidation of multiwalled carbon nanotubes. Carbon, **46**, 833–840 (2008).
DOI: 10.1016/j.carbon.2008.02.012

[17] Rosca I. D., Watari F., Uo M., Akasaka T.: Oxidation of multiwalled carbon nanotubes by nitric acid. Carbon, **43**, 3124–3131 (2005).
DOI: 10.1016/j.carbon.2005.06.019

[18] Wang M., Pramoda K. P., Goh S. H.: Enhancement of interfacial adhesion and dynamic mechanical properties of poly(methyl methacrylate)/multiwalled carbon nanotube composites with amine-terminated poly(ethylene oxide). Carbon, **44**, 613–617 (2006).
DOI: 10.1016/j.carbon.2005.10.001

[19] Lee S. H., Cho E. N. R., Jeon S. H., Youn J. R.: Rheological and electrical properties of polypropylene composites containing functionalized multi-walled carbon nanotubes and compatibilizers. Carbon, **45**, 2810–2822 (2007).
DOI: 10.1016/j.carbon.2007.08.042

[20] Gao Y., Wang Y., Shi J., Bai H., Song B.: Functionalized multi-walled carbon nanotubes improve non-isothermal crystallization of poly(ethylene terephthalate). Polymer Testing, **27**, 179–188 (2008).
DOI: 10.1016/j.polymertesting.2007.09.012

[21] Jin S. A., Yoon K. H., Park Y-B., Bang D. S.: Properties of surface-modified multiwalled carbon nanotube filled poly(ethylene terephthalate) composite films. Journal of Applied Polymer Science, **107**, 1163–1168 (2008).
DOI: 10.1002/app.27153

[22] Yoo H. J., Jung Y. C., Cho J. W.: Effect of interaction between poly(ethylene terephthalate) and carbon nanotubes on the morphology and properties of their nanocomposites. Journal of Polymer Science Part B: Polymer Physics, **46**, 900–910 (2008).
DOI: 10.1002/polb.21424

[23] Yazdani-Pedram M., Vega H., Retuert J., Quijada R.: Compatibilizers based on polypropylene grafted with itaconic acid derivatives. Effect on polypropylene/polyethylene terephthalate blends. Polymer Engineering and Science, **43**, 960–964 (2003).
DOI: 10.1002/pen.10079

[24] Sailaja R. R. N., Seetharamu S.: Itaconic acid – grafted – LDPE as compatibilizer for LDPE – plasticized Tapioca starch blends. Reactive and Functional Polymers, **68**, 831–841 (2008).
DOI: 10.1016/j.reactfunctpolym.2007.12.003

[25] ASTM D638-10: Standard test method for tensile properties of plastics (2002).

[26] Wang J., Xie H., Xin Z., Li Y.: Increasing the thermal conductivity of palmitic acid by the addition of carbon nanotubes. Carbon, **48**, 3979–3986 (2010).
DOI: 10.1016/j.carbon.2010.06.044

[27] Anoop-Anand K., Agarwal U. S., Jospeh R.: Carbon nanotubes induced crystallization of poly(ethylene terephthalate). Polymer, **47**, 3976–3980 (2006).
DOI: 10.1016/j.polymer.2006.03.079

eXPRESS Polymer Letters Vol.6, No.2 (2012) 107–119
Available online at www.expresspolymlett.com
DOI: 10.3144/expresspolymlett.2012.12

Analysis of car shredder polymer waste with Raman mapping and chemometrics

B. Vajna[1], *B. Bodzay*[1], *A. Toldy*[2], *I. Farkas*[1], *T. Igricz*[1], *Gy. Marosi*[1*]

[1]Department of Organic Chemistry and Technology, Faculty of Chemical Technology and Biotechnology, Budapest University of Technology and Economics, H-1111 Budapest, Budafoki út 8., Hungary
[2]Department of Polymer Engineering, Faculty of Mechanical Engineering, Budapest University of Technology and Economics, H-1111 Budapest, Műegyetem rkp. 3., Hungary

Received 15 June 2011; accepted in revised form 29 August 2011

Abstract. A novel evaluation method was developed for Raman microscopic quantitative characterization of polymer waste. Car shredder polymer waste was divided into different density fractions by magnetic density separation (MDS) technique, and each fraction was investigated by Raman mapping, which is capable of detecting the components being present even in low concentration. The only method available for evaluation of the mapping results was earlier to assign each pixel to a component visually and to count the number of different polymers on the Raman map. An automated method is proposed here for pixel classification, which helps to detect the different polymers present and enables rapid assignment of each pixel to the appropriate polymer. Six chemometric methods were tested to provide a basis for the pixel classification, among which multivariate curve resolution-alternating least squares (MCR-ALS) provided the best results. The MCR-ALS based pixel identification method was then used for the quantitative characterization of each waste density fraction, where it was found that the automated method yields accurate results in a very short time, as opposed to manual pixel counting method which may take hours of human work per dataset.

Keywords: *recycling, micro-Raman, hyperspectral imaging, chemometrics, polymer waste*

1. Introduction

Shredder wastes, even after thorough separation processes, consist of various components, the identification of which needs advanced analytical approach. The main components can be analysed by conventional spectroscopic methods, however, these provide only bulk information [1]. The quantitative determination of the composition and identification of the minor components destroying the processability and/or stability of the material needs additional efforts. It is of great importance to determine the sites where the degree of degradation is high and such components are present that induce mechanical and/or chemical deterioration. For these purposes the so-called hyperspectral chemical imaging techniques are promising extensions of the currently used methods.

Chemical imaging is a rapidly emerging analytical method gaining importance in multiple fields, such as food industry [2], pharmaceuticals [3–6], forensics [7] and polymers [8]. This group of techniques combines vibrational (mostly MIR, NIR or Raman) spectrometry with the spatial resolution of an optical system (usually a microscope). Either images at certain wavelengths are stacked together (*global imaging*), or distinct spectra are collected from a predetermined grid on the sample surface (*point*/*line mapping*), three-dimensional datasets are formed in a way that a vibrational spectrum corresponds to each point of the sample surface. Although the

*Corresponding author, e-mail: gmarosi@mail.bme.hu

terms 'mapping' and 'imaging' originally refer to different instrumental set-ups, their use is often considered interchangeable and 'imaging' is used as a general term to describe both approaches [3–5]. Similarly, in the present study, these terms are used as synonyms.

A large variety of questions can be answered using Raman chemical imaging, by utilizing the spatial information as well as the spectral signals. The miscibility of different binary polypropylene/polyurethane [8], polyethylene/polypropylene [9–11], polyamide/polytetrafluoroethylene [12] and ternary [13] polymer blends and their spatial structure can be studied using chemical imaging methods. Different types of heterogeneities (compositional, structural and morphological) can be defined and separately analysed [14]. Phase separations in polyfluorene have also been studied by Raman mapping [15], while other authors have investigated the effect of fillers on phase separation [16]. Material defects leading to deteriorated fatigue behaviour can be revealed [17], besides, surface characteristics and the effect of coating processes can also be monitored [18, 19]. Due to the sharp and selective Raman peaks, crystallinity and solid state characteristics can be investigated with good efficiency [9, 20]. Raman chemical imaging of polymers is becoming especially popular in the field of pharmaceuticals [21, 22].

It has been proven that the evaluation of vibrational chemical images can be greatly enhanced with multivariate data analysis techniques. Several questions can be answered by such methods: component detection and identification, object classification, and quantitative determination of certain features (e.g. concentration of components).

When unknown samples are investigated, the spectra of the pure components may not always be available. However, the huge amount of data stored in the hyperspectral images make it possible to predict or estimate the pure component spectra and to determine the spatial distribution of components even when no or only limited *a priori* information is present about the samples. Sample-sample two-dimensional correlation spectroscopy has been applied by Šašić *et al*. [23] to analyze multiple polymer blends. The visualization of polymer distributions was enhanced by principal component analysis (PCA) in the study of Stellman *et al*. [24] and by cosine correlation approach in the study of Morris *et al.* [19]. Multiple curve resolution methods have also been compared based on experiments with model samples in the fields of polymers [25] and pharmaceuticals [26, 27].

The analysis of waste materials is also an emerging issue where vibrational spectrometry and chemical imaging are very promising [28–34]. IR spectra, Raman spectra and hyperspectral images in the visible and NIR range enable the identification of post-consumer glasses [28], polymers [29], composts [30] and their contaminants [29, 30] via logical recognition rules [29] and multivariate image analysis [30]. On-line identification of polymer waste components can also be carried out with NIR imaging by using supervised classification methods if an appropriate training set (containing every polymer to be identified) is investigated previously [32, 33]. These two NIR studies showed that a NIR image can be taken from the intact polymer waste and the different plastic objects can be immediately identified via chemometric spectrum classification. It has also been proven that chemical imaging is suitable for quantitative analysis based on the number of classified pixels in each class [34]. However, chemometric processing of vibrational chemical images have not yet been studied for quantitative analysis of polymers (in an earlier study carried out by Vajna *et al.* [34] the classification of Raman spectra was carried out manually, which is an extremely time-consuming procedure).

The aim of this study was to compare different chemometric methods in the quantification of different density fractions of car shredder polymer waste by Raman mapping. As waste materials often contain unknown substances, unsupervised classification and curve resolution techniques were tested that can be applied without using any kind of training sets or reference spectra. Since real-life samples were analyzed, the most prominent challenge in this case was the poor quality of the measured datasets (highly varying and often low signal-to-noise ratio, high fluorescent background and high number of outliers due to various other effects, such as detector saturation and the presence of dyes or other additives).

2. Materials and methods

2.1. Materials

The analyzed car shredder polymer waste (CSPW) originated from a car shredder plant (Alcufer Ltd, Hungary), where cars and large household appliances are processed. At first, dust was removed with dry and wet processes, and then the magnetic metals were removed with a magnet, while the non-magnetic metals were separated with a vortex separator. The remaining material, consisting of mainly polymers, was then separated to pre-defined density fractions by inverse magnetic density separation technique [35]. Four density fractions were separated for analysis, which are shown in Table 1.

Table 1. Acquired density fractions of car shredder polymer waste (CSPW) for Raman mapping analysis

Density	Sample code
$\rho < 0.9$ g/cm^3	CSPW < 0.9
0.9 g/cm^3 $\leq \rho <$ 1 g/cm^3	CSPW 0.9–1
1 g/cm^3 $\leq \rho <$ 1.05 g/cm^3	CSPW 1–1.05
1.05 g/cm^3 $\leq \rho <$ 1.3 g/cm^3	CSPW 1.05–1.3

2.2. Raman mapping experiments

Raman mapping spectra were collected using a LabRAM system (Horiba Jobin-Yvon, Lyon, France) coupled with an external 785 nm diode laser source (Sacher Lasertechnik, Marburg, Germany) and an Olympus BX-40 optical microscope (Olympus, Hamburg, Germany). Objectives of 10× magnification were used for optical imaging and spectrum acquisition. The laser beam is directed through the objective, and backscattered radiation is collected with the same objective. The collected radiation is directed through a notch filter that removes the Rayleigh photons, then through a confocal hole and the entrance slit onto a grating monochromator (950 groove/mm) that disperses the light before it reaches the CCD detector. The spectrograph was set to provide a spectral range of 550–1750 cm^{-1} and 3 cm^{-1} resolution.

The shredded polymer waste sample was ground in a liquid N_2-cooled grinder to reduce the particle size to microscopic scale. The ground particles were pressed with a hydraulic press at 200 bar to provide 60 mm × 60 mm flat surface for the Raman analysis. The measured area was 29 × 29 points in each case. Step size of 500 μm × 500 μm was chosen between the adjacent points in order to minimize dependence between adjacent points. The spectrum acquisition time was 3 s per spectrum. 20 spectra were accumulated and averaged at each measured point (further also referred to as: 'pixel') to achieve acceptable signal-to-noise ratio.

2.3. Data analysis

Before chemometric evaluation, fluorescent background was removed using piece-wise linear baseline correction with manually chosen baseline points. The measured spectra were then normalized to unit area in order to eliminate the intensity deviation between the measured points (pixels). The Raman maps were then unfolded to a two-dimensional matrix form (**X**) of 841 rows (number of measured spectra in a map) and 1000 columns (number of wavenumber channels). A measured spectrum of the Raman map (a row in **X**) can be considered as a vector in the 1000 dimensional (spectral) vector space.

K-means clustering was carried out with Statistica 9.0 software (StatSoft, USA). All other calculations described in Sections 2.3.1.– 2.3.6. were performed in MATLAB 7.6.0 (Mathworks, Natick, USA) with PLS_Toolbox 6.0.1 and MIA_Toolbox 2.0.1 (Eigenvector Research, Seattle, USA). The chemometric methods were tested on the Raman map of the CSPW 1.05–1.3 density fraction and the best one selected was used on all other fractions.

2.3.1. Manual classification via visual inspection of spectra

Reference classification was carried out manually by visual inspection of the spectra in the Raman chemical image. Each measured spectrum (further also referred to as 'object') was visually identified (using spectral library search when needed) and classified accordingly. Spectra containing no useful information were considered as unclassified (bad) spectra.

2.3.2. Principal component analysis (PCA)

PCA [36] is a factor-analysis based method that extracts the most important factors describing the information broadly distributed in a dataset. The data matrix **X** can be resolved into three matrices by performing singular value decomposition (Equation (1)):

$$\mathbf{X} = \mathbf{U}\mathbf{\Lambda}\mathbf{V}^{\mathrm{T}} \quad (1)$$

Theoretically, the first few loading vectors (first few rows in $\mathbf{V}^T$) hold important spectral features, the others mainly consist of deviations and noise. The product of **U** and **Λ** provides the score matrix **T**. These scores can be visualized in the principal component subspace (which is a subspace of the spectral vector space described in Section 2.3.) and allow visual separation of groups of objects. PCA was performed with the pca command of MATLAB PLS_Toolbox. In every case, the first 20 principal components were calculated.

2.3.3. K-means clustering

Clustering [37] is the most common algorithm in the family of unsupervised classification models. It is based on the fact that each object can be represented with a point in the spectral vector space, the position of which is described by the corresponding row vector in **X**. If these points form groups in the vector space, these groups can be found by clustering algorithms.

K-means clustering groups the objects into a given number of clusters (pre-determined by the user). Cluster sizes and positions are iteratively calculated in a way that within-cluster distances are minimized and between-cluster distances are maximized. Some elements may not be successfully included in any of the clusters.

Two types of initializations were tried for the calculations. In the first one (*init1*), the distances among the initial cluster positions were maximized. In the second one (*init2*), initial cluster positions were chosen in a way that they would evenly span the spectral space (object distances were sorted and objects were taken at constant intervals). In each case, number of clusters was set to 20 and Euclidean distance was used for the iterations.

In order to improve the performance of clustering, the effect of an additional data preprocessing step (column standardization [38], i.e. subtracting the mean from each column and dividing each value with the standard deviation) was also tested.

2.3.4. Classical least squares (CLS)

Classical Least Squares method [38] uses the assumption of a bilinear model (Equation (2)):

$$\mathbf{X} = \mathbf{C}\mathbf{S}^T + \mathbf{E} \tag{2}$$

$\mathbf{S}^T$ ($k \cdot \lambda$) is the set of reference (pure component) spectra, each spectrum consisting of λ intensity values and forming a row in the matrix. **X** ($p \cdot \lambda$) is the matrix containing the mapping spectra, and **C** ($p \cdot k$) contains the vectors of spectral concentrations (each row in **C** contains the concentrations of the k ingredients). The matrix **E** represents the residual noise. The alignment of the above mentioned matrices is visually illustrated in reference [4].

The spectral concentrations were estimated by Equation (3):

$$\mathbf{C} = \mathbf{X}\mathbf{S}(\mathbf{S}^T\mathbf{S})^{-1} \tag{3}$$

Using CLS with all reference spectra of the expected polymers present, this method calculates the (spectral) concentration of each component (each possible polymer) in each pixel. As the particle sizes greatly exceeded the sampling volume during spectrum acquisition, in this case one measurement point was expected to correspond to only one polymer. Thus, if the calculated spectral concentration of a certain polymer reached a certain threshold level, the object was classified to the group of that particular polymer. Numerous threshold levels were tested to achieve the best results.

2.3.5. Self-modelling mixture analysis (SMMA)

SMMA [39] aims to find the purest variables (wavelength channels) by the statistical evaluation of the columns of the **X** matrix. The 'length' and 'purity' of these columns (i.e. wavenumbers) are determined based on the mean and standard deviation of the intensity values. After selecting the purest variables, the corresponding columns are used as a guess for the concentration matrix, and the pure component spectra are estimated by Equation (4).

$$\mathbf{S}^T = (\mathbf{C}^T\mathbf{C})^{-1}\mathbf{C}^T\mathbf{X} \tag{4}$$

The calculations were carried out with the '*Purity*' option in PLS_Toolbox at a very high offset level '40'. (This corresponds to $\alpha = 0.4 \cdot$(maximum intensity) offset value in the original SMMA method proposed by Windig and Guilment [39]).

2.3.6. Multivariate curve resolution – alternating least squares (MCR-ALS)

This method, as its name also implies, is an iterative approach with repeated, consecutive estimations of

C from $\mathbf{S}^T$, and vice versa [40]. Physical constraints can be applied between the steps, such as non-negativity of spectral concentrations and intensities, closure of concentration values (their sum is fixed to 1), normality of spectra, unimodality, etc. MCR-ALS needs an initial guess for either the concentrations or the spectra to start the iteration.

The iterations were performed with the *mcr* command of PLS_Toolbox, applying only non-negativity constraints (for both spectra and concentrations) and allowing 300 iteration steps. Two types of initial guesses were used: estimated spectra by SMMA without any offset, and the loadings calculated at offset '40' as described in Section 2.3.5.

2.3.7. Positive matrix factorization (PMF)

The algorithm originally developed by Paatero [41] aims to minimize the error (**E**) matrix of Equation (1) in a gradient-based manner. The errors can be weighted by the uncertainties at the different positions of the **X** matrix, but this feature was not used in this study since it was unnecessary with the experimental setup shown here.

PMF was carried out using the PMF-2 program. The default pseudorandom numbers were used as initial guesses for the pure spectra. The input error level (σ_{ij}) was set to 0.03 according to a thumb rule described in a guide to the PMF method [42].

2.3.8. Simplex identification via split augmented lagrangian (SISAL)

The method can be geometrically interpreted by finding the smallest simplex in the data space that encloses all measured spectra [43]. The apices of this simplex correspond to the pure component spectra, as all measured points are a mixture of these.

SISAL was carried out by the MATLAB implementation downloaded from the source given in the study of Lopes *et al.* [43]. Numerous different λ values (which is signed τ in the MATLAB code) were tried to achieve the best resolution. Best results were achieved with $\lambda = 1$ and 200 iteration steps.

2.4. Data evaluation and visualization

The estimated pure spectra (further also referred to as 'loadings') were visually compared to library reference spectra. The obtained scores or spectral concentrations of the meaningful loadings were refolded into a 2D array according to the spatial information in the original dataset. Object classification was carried out in the same way as described in Section 2.3.4. using the estimated spectral concentrations. This can be also considered as a 'binarization' method, i.e. the concentration of the most prominent component in a pixel is set to 1 and the concentration of the others is set to 0. Visual classification maps were created as a multi-coloured overlaid image of these binarized concentration maps. This way, the different colours correspond to different polymers. Visualization of spectra and classification maps was carried out with LabSpec 5.41 (Horiba Jobin Yvon, Lyon, France).

Polymer composition in the different CSPW fractions was calculated by counting the number of objects in each class and dividing this sum by the total number of objects (841). This ratio was multiplied by 100 to give values in percentage.

Misclassification rate (MR) was determined for each chemometric method by comparing the class assignments between the actual method and the reference class assignments described in Section 2.3.1. *MR* (in percentage) is calculated with Equation (5):

$$MR\,[\,\%\,] = \left(1 - \frac{m}{841}\right)\cdot 100 \tag{5}$$

where m is the number of matching classification assignments with the reference, i.e. the number of correct classifications in the Raman image; 841 is the total number of spectra in each dataset.

3. Results and discussion

The automated estimation of the composition of polymer waste is crucial when the question is whether a sample can be recycled. One aim in the present research was to determine whether the CSPW fractions of different density have a main component and what is the composition of these fractions. In our earlier reported Raman mapping results for quantitative polymer waste analyses the spectra in the Raman map were classified one-by-one visually [34]. This was proven to be, however, an extremely time-consuming process, which is not acceptable for industrial or any other large scale application. The primary aim of the present study was to find the most appropriate chemometric

method to identify the components present and simultaneously determine their concentrations in the sample.

The biggest challenge is the fact that these Raman datasets are of very poor quality due to numerous disturbing factors. As practically any polymers and rubbery materials can be present in the samples, which are also contaminated by other substances (e.g. glass, textile, wood), and each substance has its own response characteristics to the laser excitation, it is very difficult to find proper measurement conditions that work for most of the possible components present. Bad spectra can be obtained (1) if the peaks are blurred by high fluorescent background, (2) if the detector is saturated due to high fluorescence or unexpectedly intensive Raman bands, (3) due to the presence of dyes or other additives, (4) if a component suffers degradation during the spectrum acquisition.

A practiced expert equipped with appropriate spectral library can visually identify even bad quality spectra (if enough signal is present for the identification). The Raman images of each sample were evaluated visually in a way that the pixels containing the different polymers were visually counted. The most diverse density fraction, CSPW 1.05–1.3 was then evaluated in even more details: each pixel was classified visually. The efficiency of the studied, unsupervised chemometric methods was evaluated using the misclassification rate, i.e. what percentage of the pixels were (in)correctly classified.

Then, the performance of the chemometric method with the lowest misclassification rate was further tested based on the quantitative analysis of all other density fractions compared to the reference composition determined visually.

3.1. Visual classification of Raman spectra in the CSPW 1.05–1.3 Raman map

Thorough visual inspection of the spectra of the CSPW 1.05–1.3 sample revealed the presence of nine polymers. Objects were grouped into the following nine classes: polystyrene (PS), polypropylene (PP), polycarbonate (PC), polyamide (PA), polyvinyl chloride (PVC), polyethylene terephtalate (PET), poly(methyl metacrylate) (PMMA), polyethylene (PE) and another unknown substance (unkn.) which could not be identified due to the fact that no matching spectrum was found in the spectral library.

3.2. Exploratory analysis using PCA

Principal component analysis is a very convenient tool to explore a dataset, determine the most prominent factors and to visualize the distribution of the objects in the spectral data space (more accurately, in its principal component subspace).

Figure 1 shows the score plot of the CSPW 1.05–1.3 dataset, proving that the objects indeed form distinct groups in the data space. It should be noted that the first and the fourth principal components (PC1 and PC4) were used for the score plot. PC2 and PC3, in spite of the fact that they explain more variance in the dataset, are not that discriminative of the different polymer classes. This is most likely due to the large number of outliers in the dataset,

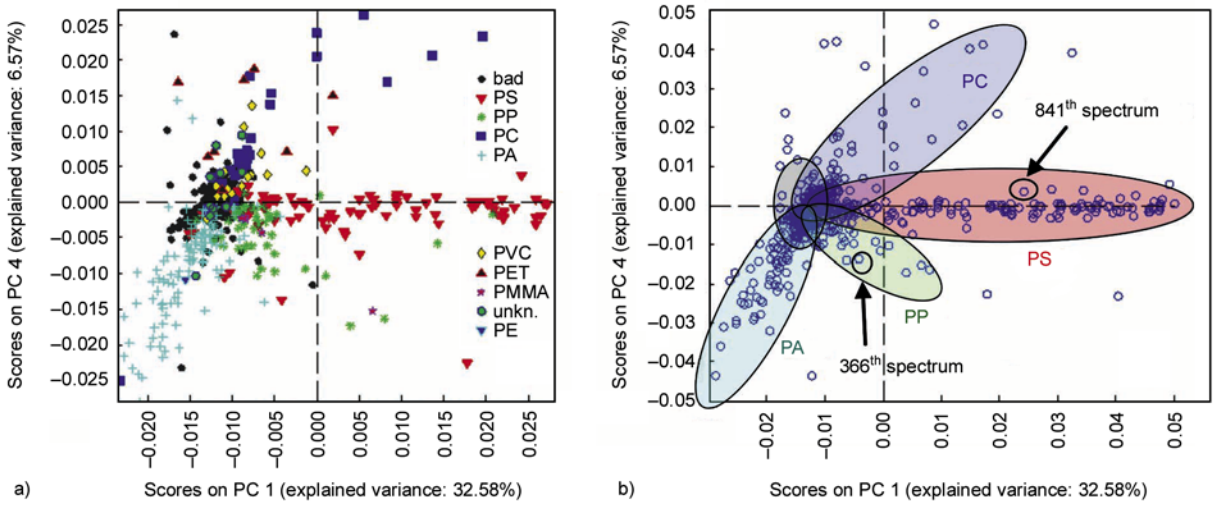

Figure 1. PCA score plot of the CSPW 1.05–1.3 Raman map: a) with reference class assignments shown; b) without reference classes but with the prominent groups marked with an ellipse

however, in chemical imaging it is always advised to visually check the principal components with lower eigenvalues (describing lower variances) as well [44].

It can be observed in Figure 1a that there is some overlap between the classes; however, the more prominent groups with a larger number of objects can be already distinguished (as also shown in Figure 1b). Even if we do not utilize the reference class information obtained visually, four polymers (PS, PP, PC and PA) can be identified by selecting certain objects in the most prominent groups (manually drawn ellipses in Figure 1b) and identifying these spectra. Further groups may be distinguished using other principal components for visualization. PCA is thus a convenient tool to get a general idea about the dataset. However, its main disadvantage is that PCA results can not be processed efficiently for unsupervised classification purposes (like those described in Section 2.4), i.e. the groups cannot be explicitly defined and the number of objects in these roughly identified groups cannot be determined. Therefore PCA cannot be used for quantitative evaluation. (It also has to be noted that not all data points are shown in Figure 1, both axes were truncated to give a clear view on all classes.)

3.3. Estimation of pure component spectra

Estimations for the spectra of the pure components present can be produced in a straightforward way using curve resolution methods (SMMA, MCR-ALS, PMF, SISAL), which provide 'loadings' that can be physically interpreted as spectra themselves. PCA also generates loadings, but these are always linear combinations of the real pure component spectra; thus, PCA gives worse estimations than curve resolution techniques [25–27]. Cluster analysis identifies groups among the objects in the dataset; the mean spectra of these clusters can be also considered as estimations for the pure component spectra (as similar spectra will most likely be placed in the same cluster).

The bad quality of the dataset reflects both in the mean spectra of the clusters and the calculated loadings (estimated pure component spectra) with the curve resolution techniques. Figure 2 shows the meaningful loadings calculated by MCR-ALS compared to the pure reference spectra of the identified polymers. Out of twenty loadings, only six are useful (L4 as PVC, L7 as PP, L12 as PC, L16 as PET, L17 as PS, L20 as PA). Loadings L5 and L9 are spectrally meaningful but practically not useful: L5 can be identified as the spectrum of a particular blue dye that often appears in the car shredder waste and is present in numerous polymers, and L9 holds similar information as L12 and corresponds to PET but with many peaks absent and lower signal-to-noise ratio. All other loadings correspond to artefacts due to baseline deviations and outliers due to detector saturation phenomena.

The findings above apply to all tested chemometric methods, i.e. the majority of the loadings (and the mean spectra of clusters) correspond to outliers and artefacts and a few are good estimations of the real spectra of the polymers present. Best results were achieved with MCR-ALS by resolving 6 polymer spectra out of the nine components present. It has to be noted, though, that L4 is a very poor estimation of the PVC spectrum as only one peak is present at 638 cm^{-1} instead of both peaks at 638 and 690 cm^{-1} (for comparison see Figure 2). The same 6 polymer spectra were resolved with PMF and SISAL. The

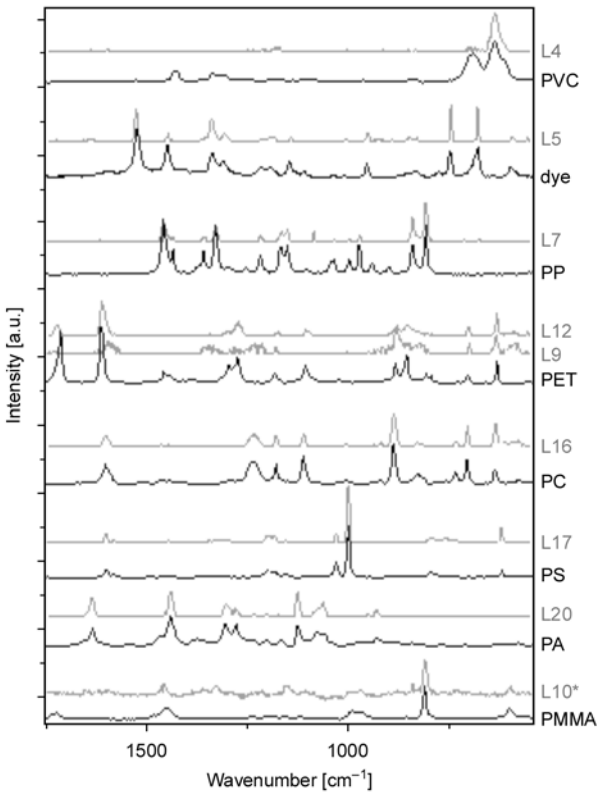

Figure 2. Selected MCR-ALS loadings (grey) of the CSPW 1.05–1.3 Raman map compared to reference spectra (black) of polymers and dyes. Loading 'L10', marked with an asterisk, was resolved with SMMA.

presence of PVC in the dataset was not detected with SMMA, but PMMA spectrum was resolved instead, which was not found using the other curve resolution methods. K-means clustering showed worse performance than other techniques by only detecting five components (PS, PP, PC, PA and PET).

3.4. Classification of measured points

Section 3.3. proved that all studied methods (or their combinations) were feasible for qualitative analysis, since the spectra of the major components could be resolved from the dataset. However, the main question is whether correct quantitative analysis can be carried out as well.

As mentioned in Section 2.3.4., each measured point is expected to contain only one polymer. The basis of quantitative analysis in these cases is to calculate the number of points containing a particular polymer and dividing this number with the total number of measured points. Consequently, it is required that each pixel is classified, i.e. it is determined, which polymer it contains. This automated classification can then be compared to the reference assignments carried out visually, and the rate of misclassification (MR) can be calculated as a quantitative measure of the accuracy of these methods.

Automated classification is straightforward in the case of the K-means clustering method, where each point is included in one certain cluster: the only task is to assign all clusters to the appropriate polymers (or meaningless 'bad' points) based on the mean spectra of the clusters. However, this is not the case when curve resolution methods are applied: these methods provide 'scores' i.e. 'concentrations' for all components in every pixel, despite the assumption that every pixel corresponds to one polymer only. Therefore, another step has to be added which unambiguously assigns pixels to the components in the sample.

Pixel assignment to a particular polymer based on calculated concentrations can be carried out via two approaches. The most straightforward possibility would be to select the loading with the highest concentration and assign it to the pixel under evaluation. This approach, however, leads to high misclassification rate because of disturbances (fluorescence, detector cut-off or dye peaks) causing the highest score to be reached by non-meaningful loadings, even if the peaks of a polymer were also significantly present.

Another possibility to assign pixels is the following: if the Raman score of a certain polymer reaches a pre-defined threshold level, the pixel will be assigned to that particular polymer. This means that only those scores are considered which correspond to a loading already identified as a polymer spectrum. Since the polymer signals are mostly overlapped with disturbing phenomena and not with the signals of other polymers, this method provided unambiguous classification of almost all pixels. Where more than one polymer could be assigned to a pixel this way, the polymer with the higher score is to be considered. The score level 25% was defined as default level for thresholding (as such score is usually only observed when a polymer is significantly present), but numerous other threshold levels were also tested.

The best results obtained with each automated classification method are visually illustrated on Figure 3. As each polymer is shown with different colour, the real spatial distribution of polymers in the sample (determined by manual classification of spectra, Figure 3a) can be compared with the automated classification carried out with the chemometric methods. Black points correspond to pixels where no clear polymer signal was detected. Misclassification rate at various threshold levels are shown in Table 2.

Table 2. Misclassification rate with the different chemometric methods

		MCR-ALS	PMF	SMMA	SISAL			CLS			K-means
threshold (score)	0.30	16.1%	18.4%	24.7%	44.7%	threshold (score)	2	53.6%	conditions	init1[a]	30.4%
	0.25	13.2%	14.8%	22.9%	40.2%		1.5	44.1%		init2[b]	24.3%
	0.20	13.7%	13.6%	21.4%	32.5%		1	44.6%		init2[b], standardization	22.8%
	0.15	25.8%	19.2%	20.3%	22.1%		1.5	51.6%			
	0.10	44.2%	33.7%	24.9%	54.9%		0.25	51.3%			

[a]Initial cluster centres set with maximum possible initial distances within the data space.
[b]Initial cluster centres set at constant intervals in the data space.

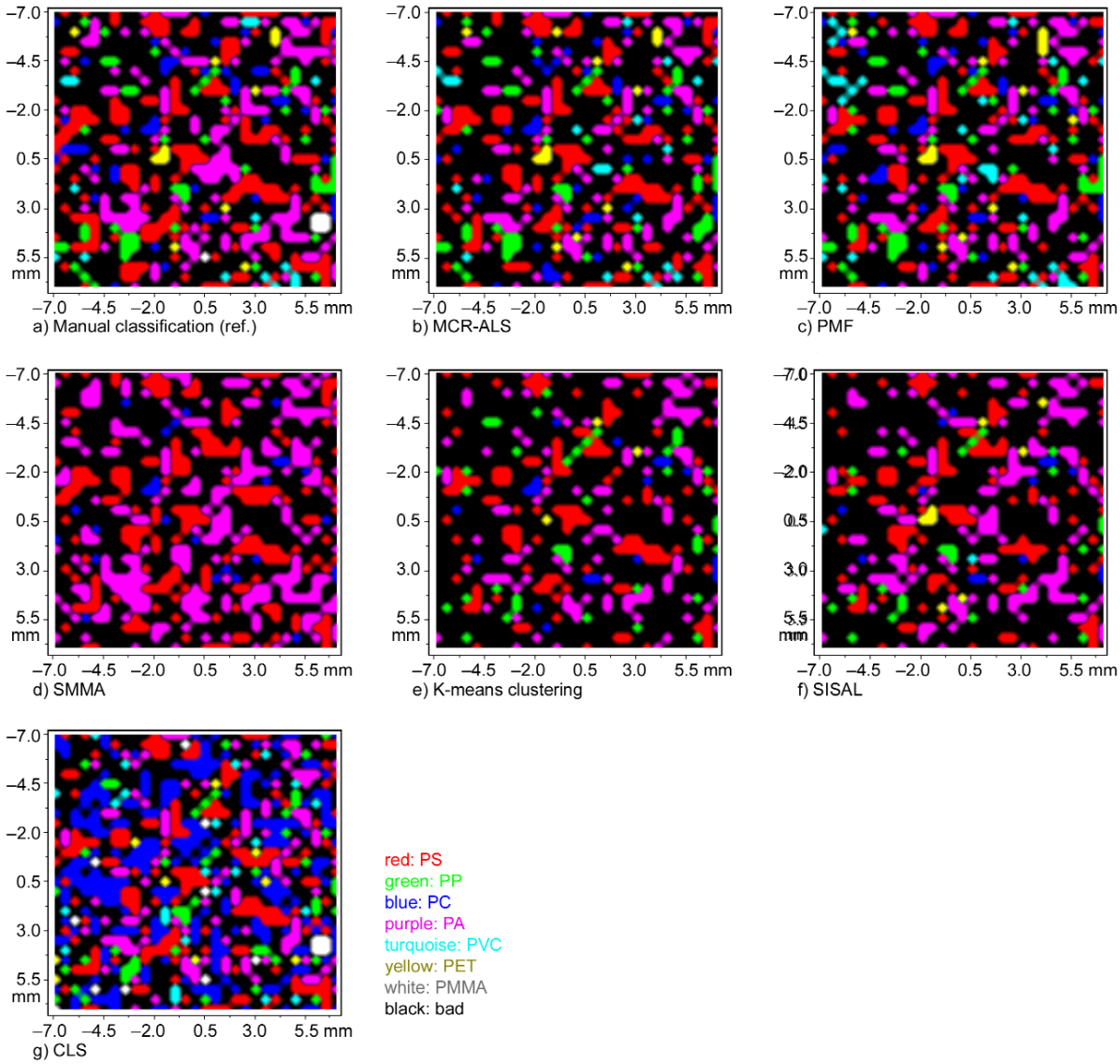

Figure 3. Pixel classification with different chemometric methods in comparison with the real polymer distribution in the CSPW 1.05–1.3 sample. (Threshold level 0.25 for curve resolution methods, K-means results in 'init2' mode and with column standardized dataset. For colour assignments the reader is referred to the web version of this article.)

Based on the scores obtained with MCR-ALS, the majority of pixels were correctly classified, especially those containing PS, PP or PET (red, green and yellow, respectively, in Figure 3b). MCR-ALS proved to be rather robust, as the outcome did not depend significantly on the applied threshold level (Table 2), making it suitable for the analysis of truly unknown substances (where the appropriate threshold level cannot be determined). The reason why the rate of misclassification increased when using very low threshold levels is that artefacts or other polymers with similar peaks can also achieve some score during the MCR-ALS resolution, but this applies to every other curve resolution method as well. Setting the threshold level too high results in the misclassification of pixels with good spectra (with unambiguous polymer signals) as bad pixels.

Similar results were obtained with PMF with slightly worse performance mainly due to more frequent misclassification of bad spectra as PVC (light blue in Figure 3c). PMF also proved to be robust with small dependence of misclassification rate on the applied threshold level (Table 2).

SMMA scores allowed correct evaluation of PS and PA content as almost all of these pixels were correctly classified (Figure 3d). Moderately accurate results were obtained for PC. However, PP (green), PET (yellow) and PMMA (white) were not detected in the Raman map using any reasonable threshold level (10% or higher), even though their spectra

were correctly resolved with the method. Further decrease of the detection threshold score leads to a high degree of misidentification of bad spectra as polymer signals. An advantage of SMMA would be that its overall misclassification rate does not depend much on the applied threshold level (Table 2), rendering this method fairly robust; however, it can only be used for the estimation of the major components.

The main advantage of K-means classification would be that bad spectra do not get misclassified as polymers. However, many pixels containing significant polymer signals were misclassified as bad spectra instead (large number of black points in Figure 3e). Misclassification rate could be significantly decreased by selecting the proper initialization method (designated *init2* in Section 2.3.3.) and by applying column standardization on the dataset. Calculating larger number of clusters and applying other or further preprocessing steps did not increase the efficiency any further.

The performance of SISAL (Figure 3f) was the worst among the curve resolution methods most probably due to the fact that the algorithm cannot cope with such high number of outliers. Although fairly good results were achieved at 0.15% threshold level, even a slight change in the threshold resulted in strong deterioration of its efficiency. Thus, it cannot be expected to work well on a new unknown dataset where the threshold level cannot be optimized.

One can raise the question whether modelling the dataset with the pure component spectra using classical least squares method allows easy and straightforward evaluation of the dataset. The first, theoretical problem with CLS is that the scope of the present study is to successfully analyze and quantify *unknown* polymer waste samples, while CLS requires the knowledge of the components present in the sample. Even if a large number of pure spectra are (even if randomly) added to the calculations, one cannot know if all pure components have been included in the model. The bigger, practical problem with CLS is that even by adding the correct pure component spectra the rate of misclassification is very high. Figure 3g shows that the misclassification of bad spectra is extremely frequent, in this case most of them misidentified as polycarbonate (blue on Figure 3g). Table 2 shows that neither using the default level, nor applying much higher threshold levels make this method feasible for the task, as bad pixels are frequently misclassified as one of the assumed polymers.

The explanation is that while curve resolution methods take the artefacts and noise effects into account by subsequent loadings, these effects cannot be taken into consideration with CLS. This also means that although these uninformative loadings resolved by curve resolution methods cannot be explicitly used and can be discarded in the evaluation, their role is very important in the correct prediction of the real components present in the waste sample.

3.5. Estimation of CSPW composition with MCR-ALS

Based on the findings in Section 3.4., the most efficient method to properly identify a component in a pixel is MCR-ALS. In the present section, this method is used for the estimation of the composition in the case of each CSPW density fraction. For classification purposes, the default threshold level of 25% was used. Real composition was calculated by visually counting the number of spectra in each CSPW Raman map to provide a reference for the MCR-ALS calculations.

Results for all the fractions of CSPW are shown in Table 3. MCR-ALS provided approximately the same results as the manual pixel counting (reference) method, while a tremendous amount of time can be saved. Major deviations from the reference were observed only in a few cases. It can be generally stated that the magnitude of error seen in Table 3 is well within tolerable limits. This makes the combination of Raman microscopic mapping and chemometrics a reliable automatic method for the quantitative characterization of polymer waste samples.

Recyclability of wastes depends both on their major constituents and traces of contaminants. While the major components with high mass fractions may be identified using non-imaging spectroscopic methods as well, the advantage of Raman microscopic mapping over conventional bulk spectroscopic methods is the complementary detection and quantification of minor components and degraded polymers that affect the processability of the waste fraction. For example, the most prominent component in CSPW fraction 1–1.05 is polystyrene, however, it contains a significant amount of PVC and PET

Table 3. Comparison of quantitative results obtained with the MCR-ALS based pixel classification and the reference method

Density g/cm^3	Method	Percentage of pixels containing the polymer [%]										
		PP	degr. PP	PE	degr. PE	PS	PVC	PC	PM-MA	PET	PA	unk.
0–0.9	MCR	54.0	38.6	7.4	–	–	–	–	–	–	–	–
	ref.	57.9	41.4	0.4	–	0.2	–	–	–	–	0.2	–
0.9–1	MCR	20.3	2.3	5.9	16.7	54.8	–	–	–	–	–	–
	ref.	21.4	4.7	4.7	16.7	52.5	–	–	–	–	–	–
1–1.05	MCR	7.8	0.5	–	–	78.7	10.1	–	–	1.8	1.1	–
	ref.	11.7	0.4	–	–	84.4	1.2	0.4	–	0.2	1.4	0.2
1.05–1.3	MCR	13.2	–	–	–	40.8	5.1	11.8	–	3.2	25.9	–
	ref.	10.6	–	0.2	–	39.2	3.3	10.2	1.1	2.4	30.8	2.2

which limit its recyclability. In contrast, density fractions below 0.9 g/cm^3 only contain PE and PP, hence were proven to be well recyclable. Additionally, it can be seen in the low density fractions that a significant amount of the polymer is degraded to some extent (spectra of intact and degraded polymers were compared in details in the study of Vajna *et al*. [34]), which also contains some information about the expectable quality of the recycled product.

4. Conclusions

Car shredder polymer waste was separated to different density fractions and the resulting samples were investigated with Raman mapping. A novel pixel identification method was developed based on an appropriate chemometric algorithm for time-efficient and accurate evaluation of the Raman maps. These datasets posed serious challenges due to tremendous amount of noise, outliers and measurement/preprocessing artefacts present in the data.

Using an appropriately diverse density fraction, the efficiency of six chemometric methods was compared to one another and to the reference visual evaluation. MCR-ALS was found to be the most robust method achieving the smallest misclassification rate, i.e. the highest accuracy. This method was then tested in the quantitative characterization of all density fractions of two polymer waste batch samples. The results proved that appropriate quantification can be carried out with MCR-ALS, also revealing the presence and estimating the amount of trace polymers and degraded parts which may influence the recyclability of the sample or the quality of the future product. While visual evaluation and manual pixel counting of a Raman map requires hours to perform, MCR-ALS calculations and subsequent pixel identification requires much less human work and reduces the time spent to minutes.

Based on the results shown in the present study, the combination of Raman mapping and appropriate chemometrics can greatly enhance the polymer recycling technologies by detailed characterization and quantitative determination of polymer waste samples. As the method developed here is based on an unsupervised curve resolution method, the investigations do not require any prior information about the samples; thus, completely unknown polymer samples can also be characterized.

Acknowledgements

The research was supported by the OTKA Research Fund (code K76346), ERA Chemistry (code NN 82426), W2Plastics EU7 Project (code 212782), and the Hungarian project TECH_08-A4/2-2008-0142. This work is connected to the scientific program of the 'Development of quality-oriented and harmonized R+D+I strategy and functional model at BME' project. This project is supported by the New Széchenyi Plan (Project ID: TÁMOP-4.2.1/B-09/1/KMR-2010-0002).

The authors express their thanks to the University of Miskolc, Hungary for the magnetic density separation of car shredder polymer waste samples. Pentti Paatero is thanked for the useful advice on the PMF program. The first author would also like to express his thanks to Péter Egyedi, László Hortobágyi, Tamás Pálinkás, Dániel Sándor, István Győrfi and Csaba Bokros (IHM) for sharing their views and inner thoughts.

References

[1] Pereira A. G. B., Paulino A. T., Rubira A. F., Muniz E. C.: Polymer-polymer miscibility in PEO/cationic starch and PEO/hydrophobic starch blends. Express Polymer Letters, **4**, 488–499 (2010). DOI: 10.3144/expresspolymlett.2010.62

[2] Gowen A. A., Taghizadeh M., O'Donnell C. P.: Identification of mushrooms subjected to freeze damage using hyperspectral imaging. Journal of Food Engineering, **93**, 7–12 (2009).
DOI: 10.1016/j.jfoodeng.2008.12.021

[3] Gowen A. A., O'Donnell C. P., Cullen P. J., Bell S. E. J.: Recent applications of chemical imaging to pharmaceutical process monitoring and quality control. European Journal of Pharmaceutics and Biopharmaceutics, **69**, 10–22 (2008).
DOI: 10.1016/j.ejpb.2007.10.013

[4] Gendrin C., Roggo Y., Collet C.: Pharmaceutical applications of vibrational chemical imaging and chemometrics: A review. Journal of Pharmaceutical and Biomedical Analysis, **48**, 533–553 (2008).
DOI: 10.1016/j.jpba.2008.08.014

[5] Amigo J. M.: Practical issues of hyperspectral imaging analysis of solid dosage forms. Analytical and Bioanalytical Chemistry, **398**, 93–109 (2010).
DOI: 10.1007/s00216-010-3828-z

[6] Gordon K. C., McGoverin C. M.: Raman mapping of pharmaceuticals. International Journal of Pharmaceutics, **417**, 151–162 (2010).
DOI: 10.1016/j.ijpharm.2010.12.030

[7] Widjaja E., Garland M.: Use of Raman microscopy and band-target entropy minimization analysis to identify dyes in a commercial stamp. Implications for authentication and counterfeit detection. Analytical Chemistry, **80**, 729–733 (2008).
DOI: 10.1021/ac701940k

[8] Schaeberle M. D., Karakatsanis C. G., Lau C. J., Treado P. J.: Raman chemical imaging: Noninvasive visualization of polymer blend architecture. Analytical Chemistry, **67**, 4316–4321 (1995).
DOI: 10.1021/ac00119a018

[9] Furukawa T., Sato H., Kita Y., Matsukawa K., Yamaguchi H., Ochiai S., Siesler H. W., Ozaki Y.: Molecular structure, crystallinity and morphology of polyethylene/polypropylene blends studied by Raman mapping, scanning electron microscopy, wide angle X-ray diffraction, and differential scanning calorimetry. Polymer Journal, **38**, 1127–1136 (2006).
DOI: 10.1295/polymj.PJ2006056

[10] Quintana S. L., Schmidt P., Dybal J., Kratochvíl J., Pastor J. M., Merino J. C.: Microdomain structure and chain orientation in polypropylene/polyethylene blends investigated by micro-Raman confocal imaging spectroscopy. Polymer, **43**, 5187–5195 (2002).
DOI: 10.1016/S0032-3861(02)00384-1

[11] Schmidt P., Dybal J., Šťudla J., Raab M., Kratochvíl J., Eichhorn K-J., Quintana S. L., Pastor J. M.: Structure of polypropylene/polyethylene blends assessed by polarised PA-FTIR spectroscopy, polarised FT Raman spectroscopy and confocal Raman microscopy. Macromolecular Symposia, **184**, 107–122 (2002).
DOI: 10.1002/1521-3900(200208)184:1<107::AID-MASY107>3.0.CO;2-X

[12] Gupper A., Wilhelm P., Schmied M., Ingolic E.: Morphology of a PA/PTFE blend studied by Raman imaging. Macromolecular Symposia, **184**, 275–285 (2002).
DOI: 10.1002/1521-3900(200208)184:1<275::AID-MASY275>3.0.CO;2-9

[13] Markwort L., Kip B.: Micro-Raman imaging of heterogeneous polymer systems: General applications and limitations. Journal of Applied Polymer Science, **61**, 231–254 (1996).
DOI: 10.1002/(SICI)1097-4628(19960711)61:2<231::AID-APP6>3.0.CO;2-Q

[14] Ellis G.: Studies on the heterogeneity of polymeric systems by vibrational microscopy. Macromolecular Symposia, **184**, 37–47 (2002).
DOI: 10.1002/1521-3900(200208)184:1<37::AID-MASY37>3.0.CO;2-4

[15] Stevenson R., Arias A. C., Ramsdale C., MacKenzie J. D., Richards D.: Raman microscopy determination of phase composition in polyfluorene composites. Applied Physics Letters, **79**, 2178–2180 (2001).
DOI: 10.1063/1.1407863

[16] Appel R., Zerda T. W., Waddell W. H.: Raman microimaging of polymer blends. Applied Spectroscopy, **54**, 1559–1566 (2000).
DOI: 10.1366/0003702001948808

[17] Marissen R., Schudy D., Kemp A. V. J. M., Coolen S. M. H., Duijzings W. G., Van Der Pol A., Van Gulick A. J.: The effect of material defects on the fatigue behaviour and the fracture strain of ABS. Journal of Materials Science, **36**, 4167–4180 (2001).
DOI: 10.1023/A:1017960704248

[18] Morris H. R., Munroe B., Ryntz R. A., Treado P. J.: Fluorescence and Raman chemical imaging of thermoplastic olefin (TPO) adhesion promotion. Langmuir, **14**, 2426–2434 (1998).
DOI: 10.1021/la971122g

[19] Morris H. R., Turner J. F. II, Munro B., Ryntz R. A., Treado P. J.: Chemical imaging of thermoplastic olefin (TPO) surface architecture. Langmuir, **15**, 2961–2972 (1999).
DOI: 10.1021/la980653h

[20] Ellis G., Gómez M., Marco C.: Practical considerations in the study of main-chain thermotropic liquid-crystalline polymers by vibrational microscopy. Analusis, **28**, 22–29 (2000).
DOI: 10.1051/analusis:2000280022

[21] Nagy Zs. K., Nyúl K., Wagner I., Molnár K., Marosi Gy.: Electrospun water soluble polymer mat for ultrafast release of donepezil HCl. Express Polymer Letters, **4**, 763–772 (2010).
DOI: 10.3144/expresspolymlett.2010.92

[22] Patyi G., Bódis A., Antal I., Vajna B., Nagy Zs., Marosi Gy.: Thermal and spectroscopic analysis of inclusion complex of spironolactone prepared by evaporation and hot melt methods. Journal of Thermal Analysis and Calorimetry, **102**, 349–355 (2010).
DOI: 10.1007/s10973-010-0936-0

[23] Šašić S., Jiang J-H., Sato H., Ozaki Y.: Analyzing Raman images of polymer blends by sample–sample two-dimensional correlation spectroscopy. Analyst, **128**, 1097–1103 (2003).
DOI: 10.1039/B303245K

[24] Stellman C. M., Booksh K. S., Muroski A. R., Nelson M. P., Myrick M. L.: Principal component mapping applied to Raman microspectroscopy of fiber-reinforced polymer composites. Science and Engineering of Composite Materials, **7**, 51–80 (1998).
DOI: 10.1515/SECM.1998.7.1-2.51

[25] Duponchel L., Elmi-Rayaleh W., Ruckebusch C., Huvenne J. P.: Multivariate curve resolution methods in imaging spectroscopy: Influence of extraction methods and instrumental perturbations. Journal of Chemical Information and Modeling, **43**, 2057–2067 (2003).
DOI: 10.1021/ci034097v

[26] Gendrin C., Roggo Y., Collet C.: Self-modelling curve resolution of near infrared imaging data. Journal of Near Infrared Spectroscopy, **16**, 151–157 (2008).
DOI: 10.1255/jnirs.773

[27] Vajna B., Patyi G., Nagy Zs., Bódis A., Farkas A., Marosi Gy.: Comparison of chemometric methods in the analysis of pharmaceuticals with hyperspectral Raman imaging. Journal of Raman Spectroscopy, **42**, 1977–1986 (2011).
DOI: 10.1002/jrs.2943

[28] Farcomeni A., Serranti S., Bonifazi G.: Non-parametric analysis of infrared spectra for recognition of glass and glass ceramic fragments in recycling plants. Waste Management, **28**, 557–564 (2008).
DOI: 10.1016/j.wasman.2007.01.019

[29] Serranti S., Gargiulo A., Bonifazi G.: The utilization of hyperspectral imaging for impurities detection in secondary plastics. The Open Waste Management Journal, **3**, 56–70 (2010).
DOI: 10.2174/1876400230100301005 6

[30] Bonifazi G., Serranti S., Bonoli A., Dall'Ara A.: Innovative recognition-sorting procedures applied to solid waste: The hyperspectral approach. in: 'Sustainable development and planning IV, Vol. 2' (eds.: Brebbia C. A., Neophytou M., Beriatos E., Ioannou I., Kungolos A. G.), WIT Press, Southampton, 885–894 (2009).
DOI: 10.2495/SDP090832

[31] Serranti S., Bonifazi G.: Hyperspectral imaging based recognition procedures in particulate solid waste recycling. World Review of Science, Technology and Sustainable Development, **7**, 271–281 (2010).
DOI: 10.1504/WRSTSD.2010.032529

[32] Kulcke A., Gurschler C., Spöck G., Leitner R., Kraft M.: On-line classification of synthetic polymers using near infrared spectral imaging. Journal of Near Infrared Spectroscopy, **11**, 71–81 (2003).
DOI: 10.1255/jnirs.355

[33] Leitner R., Mairer H., Kercek A.: Real-time classification of polymers with NIR spectral imaging and blob analysis. Real-Time Imaging, **9**, 245–251 (2003).
DOI: 10.1016/j.rti.2003.09.016

[34] Vajna B., Palásti K., Bodzay B., Toldy A., Patachia S., Buican R., Catalin C., Tierean M.: Complex analysis of car shredder light fraction. The Open Waste Management Journal, **3**, 47–56 (2010).
DOI: 10.2174/1876400230100301004 6

[35] Bakker E. J., Rem P. C., Fraunholcz N.: Upgrading mixed polyolefin waste with magnetic density separation. Waste Management, **29**, 1712–1717 (2009).
DOI: 10.1016/j.wasman.2008.11.006

[36] Malinowski E. R.: Factor analysis in chemistry. Wiley, New York (2004).

[37] Hastie T., Tibshirani R., Friedman J.: The elements of statistical learning: Data mining, inference, and prediction. Springer, New York (2009).

[38] Mark H., Workman J.: Chemometrics in spectroscopy. Academic Press, Amsterdam (2007).

[39] Windig W., Guilment J.: Interactive self-modeling mixture analysis. Analytical Chemistry, **63**, 1425–1432 (1991).
DOI: 10.1021/ac00014a016

[40] Tauler R.: Multivariate curve resolution applied to second order data. Chemometrics and Intelligent Laboratory Systems, **30**, 133–146 (1995).
DOI: 10.1016/0169-7439(95)00047-X

[41] Paatero P.: Least squares formulation of robust non-negative factor analysis. Chemometrics and Intelligent Laboratory Systems, **37**, 23–35 (1997).
DOI: 10.1016/S0169-7439(96)00044-5

[42] Paatero P.: The multilinear engine – A table-driven, least squares program for solving multilinear problems, including the *n*-way parallel factor analysis model. Journal of Computational and Graphical Statistics, **8**, 854–888 (1999).
DOI: 10.2307/1390831

[43] Lopes M. B., Wolff J-C., Bioucas-Dias J. M., Figueiredo M. A. T.: Near-infrared hyperspectral unmixing based on a minimum volume criterion for fast and accurate chemometric characterization of counterfeit tablets. Analytical Chemistry, **82**, 1462–1469 (2010).
DOI: 10.1021/ac902569e

[44] Šašić S.: An in-depth analysis of Raman and near-infrared chemical images of common pharmaceutical tablets. Applied Spectroscopy, **61**, 239–250 (2007).
DOI: 10.1366/000370207780220769

eXPRESS Polymer Letters Vol.6, No.2 (2012) 120–128
Available online at www.expresspolymlett.com
DOI: 10.3144/expresspolymlett.2012.13

A detailed study of α-relaxation in epoxy/carbon nanoparticles composites using computational analysis

A. Z. Stimoniaris[1], *C. A. Stergiou*[2*], *C. G. Delides*[1]

[1]Technological Research Center and Technological Education Institute of Western Macedonia, Laboratories of Physics and Materials Technology, 50100 Kila, Kozani, Greece
[2]Laboratory of Materials for Electrotechnics, Department of Electrical and Computer Engineering, Aristotle University, Thessaloniki 54124 Greece

Received 7 June 2011; accepted in revised form 7 September 2011

Abstract. Nanocomposites were fabricated based on diglycidyl ether of bisphenol A (DGEBA), cured with triethylenetetramine (TETA) and filled with: a) high conductivity carbon black (CB) and b) amino-functionalized multiwalled carbon nanotubes (MWCNTs). The full dynamic mechanical analysis (DMA) spectra, obtained for the thermomechanical characterization of the partially cured DGEBA/TETA/CB and water saturated DGEBA/TETA/MWCNT composites, reveal a complex behaviour as the α-relaxation appears to consist of more than one individual peaks. By employing some basic calculations along with an optimization procedure, which utilizes the pseudo-Voigt profile function, the experimental data have been successfully analyzed. In fact, additional values of sub-glass transition temperature (T_i) corresponding to sub-relaxation mechanisms were introduced besides the dominant process. Thus, the physical sense of multiple networks in the composites is investigated and the glass transition temperature T_g is more precisely determined, as the DMA α-relaxation peaks can be reconstructed by the accumulation of individual peaks. Additionally, a novel term, the index of the network homogeneity (*IH*), is proposed to effectively characterize the degree of statistical perfection of the network.

Keywords: *nanocomposites, carbon black, carbon nanotubes, thermomechanical properties, α-relaxation analysis*

1. Introduction

Carbon nanoparticles (e.g. carbon black and carbon nanotubes) are widely used as a reinforcing agent in epoxy resin products to improve their mechanical, thermal and electrical properties [1, 2]. It is thus known that the addition of carbon nanoparticles into the resin matrix can dramatically change its hardness, tensile strength, elastic modulus and electrical conductivity. Specifically, the effects of the nanofillers in polymer composites on the glass transition (T_g) and on the relaxation behaviour of the polymer matrix have been studied for different filler–resin composites. However, the remarks on T_g variation are controversial as in some cases an increase in T_g with filler content is reported in the literature [3–5], yet the opposite result is possible as well [6, 7]. Additionally, the variation of T_g as a function of filler content in epoxy nanocomposites shows an initial decrease up to a certain content value followed by an increase at higher filler loading [8, 9]. Therefore, the actual effect of the filler on the T_g necessitates further clarification, as it is also reviewed for MWCNT composites in [10]. In general, the amount, the dispersion and the surface conditions of the nanoparticles were found to play an important role in the variation of T_g and the mechanical properties of the nanocomposites [7, 11–13]. In epoxy nanocomposites and generally in thermoset nanocomposites there is an additional difficulty met, compared to the thermoplastic nano-

*Corresponding author, e-mail: stergiou.babis@gmail.com

composites. In particular, the curing conditions of the nanocomposites and their results are different from those of the pure epoxy probably due to the effect of the nanoparticles on the crosslinking mechanism [8]. With regard to the thermoset epoxies a significant amount of data has been accumulated about water absorption and diffusion and their effect on the dynamic mechanical behaviour [11, 14]. However, for the understanding and explanation of all the experimental data there are still some points open to question. Among them two different material systems, namely the sub-cured DGEBA/TETA/CB and the water-saturated DGEBA/TETA/MWCNTs composites, which exhibit complex $\tan\delta$ curves in the dynamic mechanical analysis (DMA) spectra, may function as the case studies for a more detailed analysis.

Therefore, in this work besides the study of the mechanical dynamics of epoxy nanocomposites we focus our attention on the analysis of the α-relaxation peak, where this complex relaxation spectrum appears. To this end, a computational approach is successfully applied based on the analysis of the complex $\tan\delta$ spectrum and the introduction of more than one relaxation mechanisms. In addition to the computational analysis, a new index is proposed to characterize the network homogeneity.

2. Experimental

2.1. Materials

The pre-polymer D.E.R.332 used in this study was diglycidyl ether of bisphenol A (DGEBA) supplied by Fluka SA, USA, with epoxy equivalent 190, molecular weight 380 and viscosity 15 000 cP at 25°C. The hardener used was triethylenetetramine (TETA) supplied by Sigma Aldrich, USA. The extra conductive carbon black (particle size 25–75 nm) was obtained from Degussa, Germany, whereas the multi-wall carbon nanotubes (NC3152), with average diameter of about 9.8 nm and average length of 1 μm, were supplied by Nanocyl, Belgium. All the components of the system are commercial products and they were used without further purification.

2.2. Sample preparation and characterization

In order to prepare the DGEBA/TETA/CB and DGEBA/TETA/MWCNT composites, the pre-polymer was initially heated at 40°C to decrease its viscosity. The necessary amounts of TETA (epoxy/TETA = 100/14) and CB or MWCNT were then added and the mixture was mechanically stirred for 1 hour at 2000 rpm and degassed under vacuum for 15 minutes. Finally, the mixture was sonicated for 30 minutes at 200 W (Hielscher ultrasonic processor), in order to suppress the possible formation of agglomerates and bundles, and degassed again. The produced homogeneous liquid was poured in rectangular shaped molds with dimensions $40 \times 10 \times 1.5$ mm and the samples were cured at 60°C for 20 hours, whereas some of the samples were subjected to an additional post-curing heat treatment at 150°C for 2 hours. For the characterization of the fabricated samples a Polymer Laboratories dynamic mechanical thermal analyzer MK III was used according to ASTM D7028-07e1. Measurements of the tensile storage and loss modulus E' and E'' and loss tangent tanδ were performed from room temperature up to 200°C on a constant rate of 2°C/min, at the frequency of 10 Hz and with a 4% strain. In each of the tests, at least three different samples were tested, and the average results were recorded.

2.3. Computational approach

It is well known from polymer theory that the relaxations in polymers and especially in composites are complex processes which stem from different mechanisms [8, 11, 15–18]. Among various theoretical models, which have been proposed to describe these complex effects, the assumption that the recorded process consists of discrete elementary relaxation processes constitutes a realistic and practical approach. Therefore, we have written a specialized computer program to carry out the computational analysis of the α-relaxation in epoxy nanocomposites, where a complex behaviour appears.

Generally, the measured diagram of $y = \tan\delta$ as a function of temperature $x = T$ can be considered as the result of the contribution and overlapping of individual peaks, which correspond to distinguished relaxations and are indicative of a heterogeneous cross-link topology [19]. These phenomena can be expressed either by Gaussian (G) or Lorentzian (L) distribution, which allows the constituent curve K at the arbitrary temperature x_i to be described by Equations (1) and (2):

$$\Phi_G = \frac{C_0^{1/2}}{H_K \pi^{1/2}} \exp\left(\frac{- C_0 (x_i - x_K)^2}{H_K^2} \right)$$

Gaussian (G) (1)

$$\Phi_L = \frac{C_1^{1/2}}{\pi H_K} \left(1 + C_1 \frac{(x_i - x_K)^2}{H_K^2} \right)^{-1}$$

Lorentzian (L) (2)

where C_0 and C_1 are the normalization fitting constants, x_K is the temperature at the curve's peak, and H_K is the full width at half maximum (FWHM) of the curve K. Nevertheless, better results in the description of real systems can be produced by employing the pseudo-Voigt (pV) function, which is the weighted sum of both functions of Gaussian and Lorentzian formula (Equation (3)):

$$\Phi_{pV} = \eta \cdot \Phi_L + (1 - \eta) \cdot \Phi_G$$

pseudo-Voigt (pV) (3)

where $\eta \leq 1$ is the ratio between the Lorentzian and the Gaussian function. Despite the widespread use of the pV function defined in Equation (3) in materials research, for instance in X-rays diffraction and Raman spectroscopy [20, 21], to the best of our knowledge there is no previously reported application of this function in the investigation of the composites' mechanical properties.

The performed analysis constitutes a typical optimization process in pursuit of the model parameters yielding the minimum value of the selected objective functions. Specifically, as the experimental relaxation spectrum is analyzed to its constituent sub-relaxations, the objective is the minimization of the difference between the measured and calculated master curve by employing the minimum number of component K curves. The obtained characteristic parameters of each K curve are the temperature x_K, the value of the peak y_K and the FWHM HK after the subtraction of the background. The normalization constants C_0 and C_1 for fitting the profile of functions to experimental data are also calculated by the optimization process. During the execution of the program, components can be added and their parameters can be modified. The finally calculated value yci, which corresponds to temperature x_i, is the sum of all contributed components $y_i = s \cdot \Phi_{pV} \cdot |x_i - x_K|$, including the background y_b. Therefore, y_{ci} is given by Equation (4):

$$y_{ci} = s \cdot \sum_K (\Phi_{pV} \cdot |x_i - x_K|) + y_b \quad (4)$$

where the scale factor s is to be optimized as well. By using the least square method, the parameters producing the best approximation of the y_{ci} calculated from the Equation (4) to the experimental values are evaluated after several iterations. By that means, the experimental profile $y = \tan\delta$ is analyzed to its constituent individual curves, serving to elucidate the complex α-relaxation spectrum of epoxy/carbon nanoparticle composites.

At this point, we should additionally define the area S_K that is encompassed by one curve and the line of background, since this expresses the contribution of each mechanism to the relaxation master curve. Since the area S_K of the curve K is extended to the whole temperature range of the experiment, it is given by Equation (5):

$$S_K = \sum_i \left[\frac{1}{2} (y_i + y_{i+1})(x_{i+1} - x_i) \right] \quad (5)$$

3. Results and discussion

3.1. Theoretical background

As it is well known, the glass transition process may be considered as being controlled by the intrinsic flexibility of the backbone or as a function of the free volume available within the polymer. In the latter model, conformational change can only occur when there is sufficient free volume for the chain to move. The free volume is assumed to diffuse throughout the polymer at a rate controlled by the motion of the chains and has a critical value for the onset of large segmental motion. Moreover, according to the intrinsic flexibility approach the variation of chemical structure also involves an intermolecular contribution. Thus, the apparent equivalence of the two approaches for the description of the glass transition lies in the fact that any change will influence both the intra- and intermolecular contributions to the overall potential. Therefore, different factors imposed during curing (e.g. heating procedure, time and frequency of mechanical stirring and sonication) and the incorporation of fillers and/or small molecules, such as water, strongly affect the dynamic mechanical behaviour.

3.2. Sub-cured DGEBA/TETA/CB composites

The typical DMA traces of dynamic storage modulus (E') and loss tangent tanδ for the unfilled resin and the DGEBA/TETA/CB system cured at 60°C for 20 hours (sub-curing) are respectively presented in Figures 1 and 2.

An anisotropic behaviour of modulus E' is clearly detected, as it is strongly affected by the filler content in the glassy state and slightly in the rubbery one. However, apart from the discontinuity observed for the 0.5% CB loaded sample, the modulus at room temperature interestingly reaches its maximum for 0.7% of CB loading, which is in accordance with the dielectric measurements where the percolation threshold for the same system was observed with 1.0% CB loading [8]. Concerning the dependence of T_g on the filler content, when estimated at the tanδ maximum, an increase is observed up to a maximum (156°C) corresponding to CB loading of about 0.7%. Therefore we assume that for this filler concentration the crosslink density reaches its maximum value. Beyond this critical concentration T_g is decreasing as at high CB concentration the nanoparticles aggregate [8, 9], yielding the increase of the free volume.

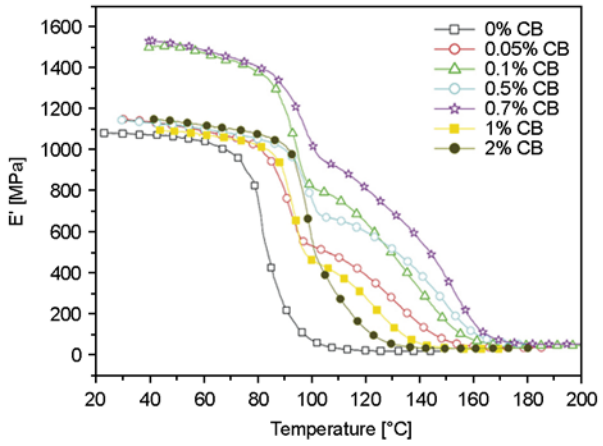

Figure 1. E' spectra of DGEBA/TETA/CB with temperature. Curing conditions: 60°C for 20 hours (sub-cured).

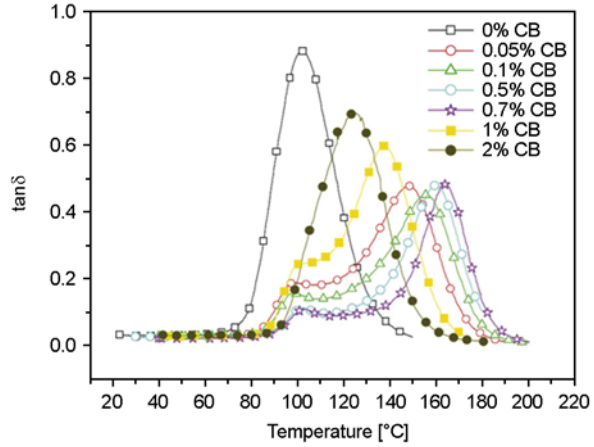

Figure 2. Tanδ spectra of DGEBA/TETA/CB with temperature. Curing conditions: 60°C for 20 hours (sub-cured).

The height and width of the peaks in tanδ spectra provide additional information about the relaxation behaviour of these samples. The height of the peak for the neat resin has a value 0.9, while for the composites it varies between 0.4–0.7 respectively for 0.7–2% CB loading. This implies that the composites exhibit more elastic behaviour than the neat resin. The significant change in the width of the peak suggests a broader distribution of relaxation times, presumably due to more nanoparticle-polymer interactions, and hence restricted mobility.

In addition to this, a new relaxation peak is observed just below the T_g in the partially cured nanocomposites, at the same temperature as for the pure resin. This indicates, at a first glance, the existence of at least two underlying mechanisms of α-relaxation in these curing stages. The first mechanism is caused by the reaction of the crosslink agent with the epoxy groups giving rise to the dominant α-relaxation, while the second one appears as a result of the filler's effect on the curing reaction. The formation of a few nanometres thick intermediate layer on the resin-filler interface, as it has already been reported in [4, 5, 11, 22], probably occurs before the full cure of the composite, thereby inducing the growth of the secondary peak demonstrated in Figure 2. However, as the crosslink density increases in the post-cured composites, the interface region is significantly reduced and the sub-T_g relaxations disappear due to the final incorporation of the loose chains into the main network.

3.3. DGEBA/TETA/MWCNT water saturated composites

The DMA spectra of storage modulus E' and tanδ for the water saturated samples of the DGEBA/TETA/MWCNTs composites are depicted in Figures 3 and 4. It is hence clearly seen that an additional relaxation peak occurs below T_g, at the same temperature as for the transition of the pure resin. These spectra are quite similar to those observed in sub-cured epoxy composites filled with CB (Figures 1 and 2).

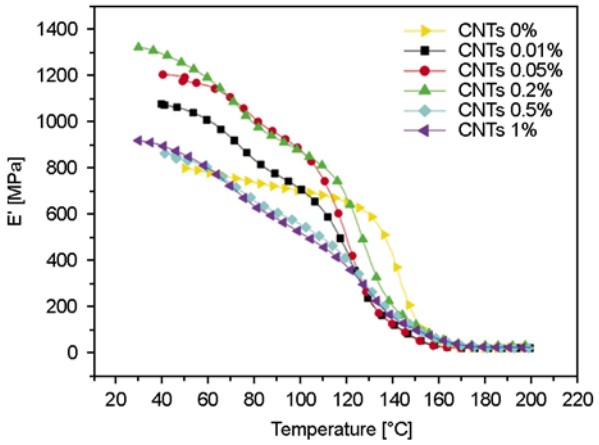

Figure 3. E' spectra of water saturated DGEBA/TETA/MWCNTs composites with temperature. Curing conditions: 60°C for 20 hours (sub-cured) and 150°C for 2 hours (post-cured).

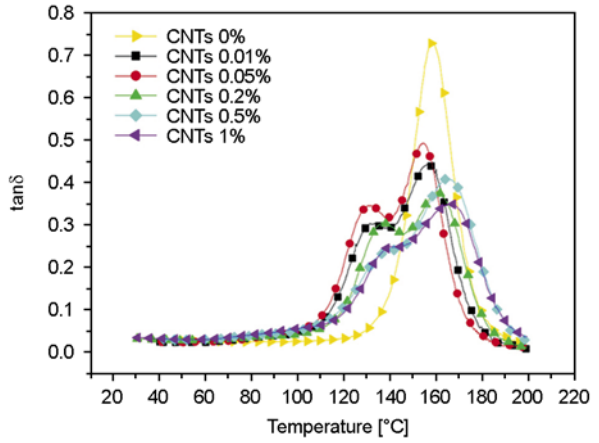

Figure 4. Tan δ spectra of water saturated DGEBA/TETA/MWCNTs composites with temperature. Curing conditions: 60°C for 20 hours (sub-cured) and 150°C for 2 hours (post-cured).

The obtained values of the main and sub-T_g temperature for the case of 0.05% CNT content are displayed in Figure 5. This extra relaxation peak is attributed to the bound water molecules either acting as a plasticizer or participating in the network via hydrogen bonding [14, 23]. Thus, by affecting

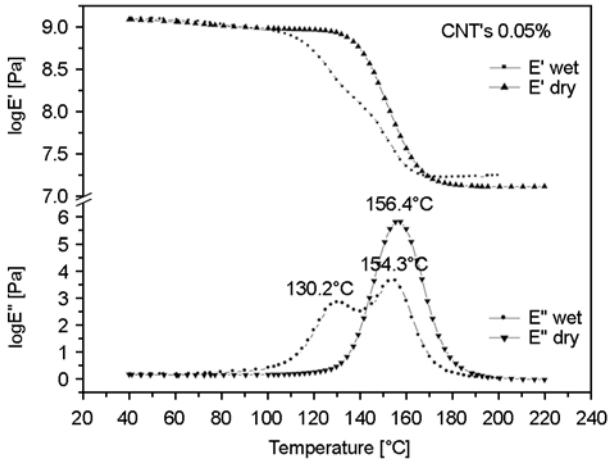

Figure 5. E' and E'' spectra of DGEBA/TETA/MWCNTs with 0.05% filler content, wet and dried at 220°C

the inter- and intra-molecular flexibility of the backbone it introduces a new relaxation mechanism. In fact, the absence of any sub-T_g relaxation in the unfilled resin (Figure 4) along with its disappearance after the water removal, which is noticed in Figure 5, bear additional evidence of this process.

3.4. T_g calculation and network homogeneity

According to the computational process described in Section 2.3, the broad α-relaxation peak is considered as the master curve of the multiple α_i-rexations, each with a different sub-glass transition temperature T_i. Thereby, the analyzed tan δ curves for samples with 0.1 and 0.7% CB content are shown in Figures 6a and 6b. In both spectra the experimental peak is reconstructed by six smaller, namely the dominant one close to the experimental maximum, four peaks at lower temperature and a small one at higher temperature. By using the optimization algorithm the characteristic maximum temperature T_i and the full width at half maximum H_i of the sub-α_i-relaxations were obtained, whereas the bounded area S_i was calculated from Equation (5). The results

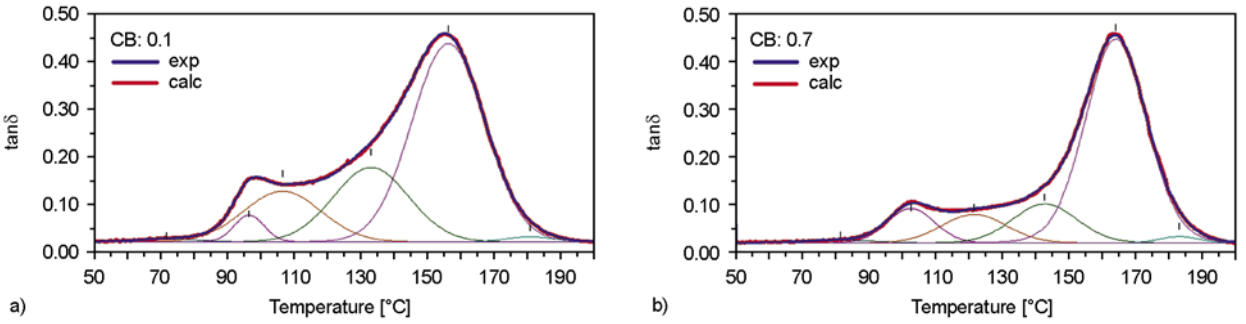

Figure 6. Computational analysis of tanδ curves for DGEBA/TETA/CB with a) 0.1% and b) 0.7% CB

Table 1. Computational analysis results for DGEBA/TETA/CB with 0.1% CB

Curve	T_i [°C]	y_i	H_i [°C]	S_i
1	72	0.006	21.968	0.136
2	97	0.056	10.478	0.627
3	107	0.106	27.335	3.099
4	133	0.156	26.659	4.451
5	156	0.416	25.723	11.437
6	181	0.010	16.786	0.184

for the composite with 0.1% CB content are presented in Table 1.

The contribution weight of each sub-relaxation to the formation of the master curve depends on its characteristics. Taking this into account, the calculated glass transition (T_{gc}) can be introduced by Equation (6):

$$T_{gc} = \frac{\sum T_i \cdot S_i}{\sum S_i} \quad (6)$$

A comparison between the calculated T_{gc} from Equation (6) and the estimated values of $T_{g\,exp}$ from the tan δ maximum is provided in Table 2 for different CB loadings. These new $T_{g\,c}$ values are up to 9% lower than the experimentally estimated values $T_{g\,exp}$. However, they should be more reliable in describing the α-relaxation with a complex profile, since they solely reflect the phenomenon under test, contrary to $T_{g\,exp}$.

Similarly, the analysis of the tan δ curves of the samples with 0.05 and 0.20% CNT content is depicted in Figures 7a and 7b, where both spectra appear to comprise four different peaks. The obtained characteristic parameters for the DGEBA/TETA/MWCNTs composites with 0.05% nanotubes content are listed in Table 3. The corresponding $T_{g\,c}$ values are calculated from Equation (6) and presented in Table 4, in addition to the estimated $T_{g\,exp}$. These new $T_{g\,c}$ values are again up to 7% lower than the initially estimated from the tan δ maximum. Moreover, it is evident that the two main peaks are comparable concerning their height and the included area. This indicates the existence of basically two mechanisms with similar characteristics, responsible for the formation of the peak in tan δ spectra.

The network architecture is a key issue in the analysis of complex α-relaxation in polymer composites. In a 'perfect' network the α-relaxation peak is expected to possess a Gaussian bell-shaped distribution. In any other case the deviation from the Gaussian behaviour can be considered as an evidence of heterogeneity and lack of cohesion of the

Table 3. Computational analysis results for DGEBA/TETA/MWCNTs with 0.05% of CNTs

Curve	T_i [°C]	y_i	H_i [°C]	S_i
1	106	0.018	27.482	0.531
2	131	0.310	24.020	8.035
3	155	0.442	18.799	8.965
4	173	0.033	19.021	0.673

Table 2. Comparison between experimental ($T_{g\,exp}$) and calculated ($T_{g\,c}$) values for DGEBA/TETA/CB with different CB contents

CB %	$T_{g\,exp}$ [°C]	$T_{g\,c}$ [°C]	$T_{g\,exp} - T_{g\,c}$ [°C]
0.05	148	135	13
0.1	155	141	14
0.5	160	148	12
0.7	164	151	12
1.0	137	130	8
2.0	124	121	3

Table 4. Comparison between experimental ($T_{g\,exp}$) and calculated ($T_{g\,c}$) values for DGEBA/TETA/MWCNTs with different CNTs contents

CNTs %	$T_{g\,exp}$ [°C]	$T_{g\,c}$ [°C]	$T_{g\,exp} - T_{g\,c}$ [°C]
0.01	157	152	5
0.05	155	144	11
0.2	161	150	11
0.3	159	150	9
0.5	165	155	10
1	167	155	12

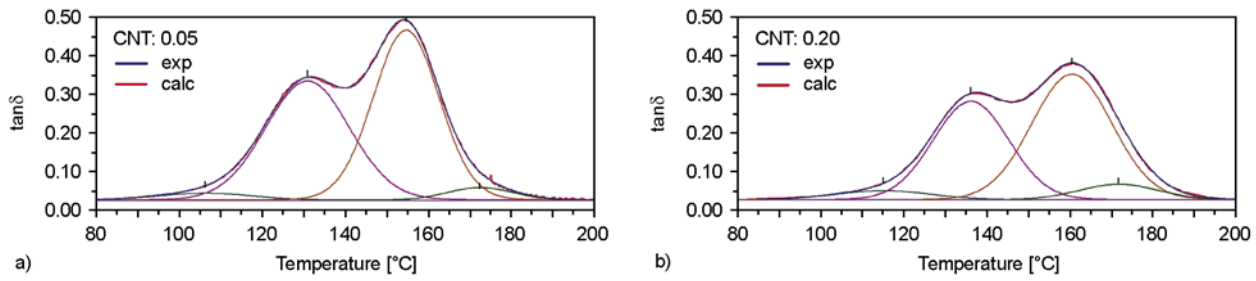

Figure 7. Computational analysis of tan δ curves for DGEBA/TETA/MWCNTs with a) 0.05% and b) 0.2% CNTs.

network due to various phenomena, such as entanglements, free chain ends and complexities produced by the incorporation of the nanoparticles into the backbone of the network. In order to quantify this deviation, based on the above described computational analysis we introduce an index for the network homogeneity (*IH*), calculated from Equation (7):

$$IH = \frac{S_{\mathrm{KDom}}}{S_{\mathrm{KDom}} + \sum_{i=1}^{n} S_{\mathrm{Ki}}} \tag{7}$$

where S_{KDom} is the bounded area of the main peak and S_{Ki} corresponds to the ith secondary peak. For the post-cured pure epoxy matrix the Equation (7) yields the *IH* value 0.92. Although, *IH* and T_g are influenced by the nanoparticles loading on the basis of the same phenomena, they are not by definition proportional to each other. Moreover, on the strength of the Equation (7), we deduce that *IH* may theoretically range up to 1.

Based on these remarks, the calculated values of *IH* for various composites containing CB are shown in Figure 8. It can be derived that the *IH* of the nanocomposites is highly dependent on CB concentration. Specifically, there is an initial increase of *IH* up to a definite maximum of about 0.66 for 0.7% CB content, whereas it decreases for higher filler content. Taking into consideration the occurrence of the percolation threshold at 1.0% CB loading [8], the decrease of the main peak contribution and thus of *IH* for loading above that value may be ascribed to the increase of the network agglomerations and inhomogeneities. Besides, a variety of network

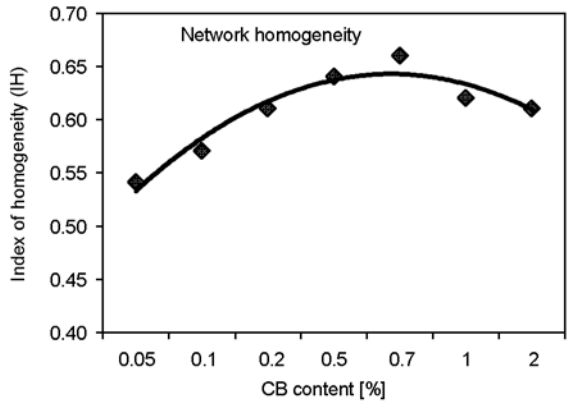

Figure 8. The index of network homogeneity *IH* as a function of CB nanoparticles content in sub-cured epoxy composites

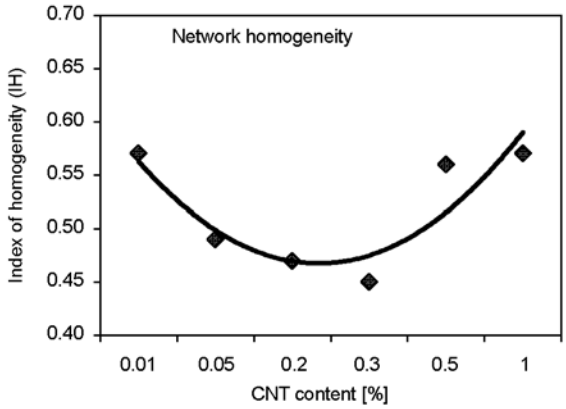

Figure 9. The index of network homogeneity *IH* as a function of MWCNTs content in epoxy composites

defects, such as dangling ends, elastically ineffective loops and entanglements, are known to occur in the epoxy-filler system, liberating an increased number of interaction sites or crosslinking species.

In contrast with the dependence of the index *IH* on the CB content, the reverse variation of *IH* is observed in water saturated composites with MWCNTs. The estimated *IH* values for water saturated composites containing MWCNTs as a function of filler content are shown in Figure 9. The drawn data reveal the decrease in IH from 0.57 to a minimum of 0.45 for 0.3% CNTs content, followed by an increase for higher loading. Since the water uptake is related to the small network homogeneity, this trend may reflect the initial increase of the absorbed water. Furthermore, for 0.5–1% CNT concentration the absorption level diminishes to that of the pure epoxy [24], which may also account for the steady *IH* values of the highly loaded samples. Generally, *IH* of the CNT composites are lower than those of the CB sub-cured composites, which can be attributed to the water uptake that alters the network response to the mechanical perturbations. This assumption is further supported by the diagrams of Figures 7a and 7b, where the appearance of two major peaks with comparable size indicates the evenly strong contribution of the water-related relaxation.

4. Conclusions

In this research the complex relaxation spectra obtained from the thermomechanical characterization of epoxy nanocomposites are analyzed into their constituent curves corresponding to individual relaxation mechanisms. A computational method is

employed for the extraction of useful information about the mechanisms responsible for the α-relaxation in polymer composites. This analysis is based on the analogy between the bounded area by the curves and the respective relaxation strength. In this framework, two systems of epoxy nanocomposites are studied, namely the subcured DGEBA/TETA/CB and the water saturated DGEBA/TETA/MWCNTs, for which the complex α-relaxation spectra possibly occur due to the formation of two separate coexisting networks. This refers to the network of the pure epoxy matrix and the network formed by the nanoparticles either through the filler-epoxy interface (CB) or through the participation of the amino functionalized CNTs to the crosslinking procedure (MWCNTs). The correspondence of the calculated constituent peaks with the respective network is supported by experimental findings. Furthermore, our technique enables the more precise description of the α-relaxation and the evaluation of the actual T_g. Finally, the network complexity due to various defects seems to be related to the α-relaxation profile. Therefore, the analysis of the relaxation spectrum with the assistance of the introduced index *IH* can be used for the qualitative and quantitative assessment of any composite system's homogeneity. The variation in the calculated homogeneity of the two investigated systems is in agreement with the occurrence of network defects above the percolation threshold and the increase of the water content.

Acknowledgements

Acknowledgements are expressed to Professor P. Pissis for the stimulating discussions during this work and to students Eleni Nikolaidou and Christos Liakopoulos for their contribution to sample preparation.

References

[1] Dresselhaus M. S., Dresselhaus G., Avouris P., Smalley R. E.: Carbon nanotubes, synthesis, structure, properties and applications. Springer-Verlag, Berlin (2001).

[2] Mai Y., Yu Z.: Polymer nanocomposites, CRC Press, Boca Raton (2006).

[3] Karippal J. J., Narasimha Murthy H. N., Rai K. S., Krishna M., Sreejith M.: The processing and characterization of MWCNT/epoxy and CB/epoxy nanocomposites using twin screw extrusion. Polymer-Plastics Technology Engineering, **49**, 1207–1213 (2010). DOI: 10.1080/03602559.2010.496413

[4] Hergeth W-D., Steinau U-J., Bittrich H-J., Simon G., Schmutzler K.: Polymerization in the presence of seeds. Part IV: Emulsion polymers containing inorganic filler particles. Polymer, **30**, 254–258 (1989). DOI: 10.1016/0032-3861(89)90114-6

[5] Kotsilkova R., Fragiadakis D., Pissis P.: Reinforcement effect of carbon nanofillers in an epoxy resin system: Rheology, molecular dynamics, and mechanical studies. Journal of Polymer Science Part B: Polymer Physics, **43**, 522–533 (2005). DOI: 10.1002/polb.20352

[6] Ash B. J., Schadler L. S., Siegel R. W.: Glass transition behavior of alumina/polymethylmethacrylate nanocomposites. Materials Letters, **55**, 83–87 (2002). DOI: 10.1016/S0167-577X(01)00626-7

[7] Shen J., Huang W., Wu L., Hu Y., Ye M.: The reinforcement role of different amino-functionalized multiwalled carbon nanotubes in epoxy nanocomposites. Composites Science and Technology, **67**, 3041–3050 (2007). DOI: 10.1016/j.compscitech.2007.04.025

[8] Kosmidou T. V., Vatalis A. S., Delides C. G., Logakis E., Pissis P., Papanicolaou G. C.: Structural, mechanical and electrical characterization of epoxy-amine/carbon black nanocomposites. Express Polymer Letters, **2**, 364–372 (2008). DOI: 10.3144/expresspolymlett.2008.43

[9] Brown J., Rhoney I., Pethrick R. A.: Epoxy resin based nanocomposites: 1. Diglycidylether of bisphenol A (DGEBA) with triethylenetetramine (TETA). Polymer International, **53**, 2130–2137 (2004). DOI: 10.1002/pi.1638

[10] Allaoui A., El Bounia N.: How carbon nanotubes affect the cure kinetics and glass transition temperature of their epoxy composites? – A review. Express Polymer Letters, **3**, 588–594 (2009). DOI: 10.3144/expresspolymlett.2009.73

[11] Sun Y., Zhang Z., Moon K-S., Wong C. P.: Glass transition and relaxation behavior of epoxy nanocomposites. Journal of Polymer Science Part B: Polymer Physics, **42**, 3849–3858 (2004). DOI: 10.1002/polb.20251

[12] Hemmati M., Rahimi G. H., Kaganj A. B., Sepehri S., Rashidi A. M.: Rheological and mechanical characterization of multi-walled carbon nanotubes/polypropylene nanocomposites. Journal of Macromolecular Science Part B, **47**, 1176–1187 (2008). DOI: 10.1080/00222340802403396

[13] Prashantha K., Soulestin J., Lacrampe M. F., Claes M., Dupin G., Krawczak P.: Multi-walled carbon nanotube filled polypropylene nanocomposites based on masterbatch route: Improvement of dispersion and mechanical properties through PP-g-MA addition. Express Polymer Letters, **2**, 735–745 (2008). DOI: 10.3144/expresspolymlett.2008.87

[14] Papanicolaou G. C., Kosmidou T. V., Vatalis A. S., Delides C. G.: Water absorption mechanism and some anomalous effects on the mechanical and viscoelastic behavior of an epoxy system. Journal of Applied Polymer Science, **99**, 1328–1339 (2006).
DOI: 10.1002/app.22095

[15] Pethrick R. A., Amornsaichai T., North A. M.: Introduction to molecular motion in polymers. Whittles Publishing, Dunbeath (2011).

[16] Lakes R. S.: Viscoelastic solids. CRC Press, Boca Raton (1998).

[17] Liu Y., Wang Y-F., Gerasimov T. G., Heffner K. H., Harmon J. P.: Thermal analysis of novel underfill materials with optimum processing characteristics. Journal of Applied Polymer Science, **98**, 1300–1307 (2005).
DOI: 10.1002/app.22272

[18] Psarras G. C., Gatos K. G., Karahaliou P. K., Georga S. N., Krontiras C. A., Karger-Kocsis J.: Relaxation phenomena in rubber/layered silicate nanocomposites. Express Polymer Letters, **1**, 837–845 (2007).
DOI: 10.3144/expresspolymlett.2007.116

[19] Becker O., Simon G. P., Dusek K.: Epoxy layered silicate nanocomposites. Advance Polymer Science, **179**, 329–347 (2005).
DOI: 10.1007/b107204

[20] Komorida Y., Mito M., Deguchi H., Takagi S., Millán A., Silva N. J. O., Palacio F.: Surface and core magnetic anisotropy in maghemite nanoparticles determined by pressure experiments. Applied Physics Letters, **94**, 202503/1–202503/3 (2009).
DOI: 10.1063/1.3131782

[21] Zhang L., Yilmaz E. D., Schjødt-Thomsen J., Rauhe J. C. M., Pyrz R.: MWNT reinforced polyurethane foam: Processing, characterization and modelling of mechanical properties. Composites Science and Technology, **71**, 877–884 (2011).
DOI: 10.1016/j.compscitech.2011.02.002

[22] Li B., Zhong W-H.: Review on polymer/graphite nanoplatelet nanocomposites. Journal of Materials Science, **46**, 5595–5614 (2011).
DOI: 10.1007/s10853-011-5572-y

[23] Zhou J., Lucas J. P.: Hygrothermal effects of epoxy resin. Part I: the nature of water in epoxy. Polymer, **40**, 5505–5512 (1999).
DOI: 10.1016/S0032-3861(98)00790-3

[24] Sanchez-Garcia M. D., Lagaron J. M., Hoa S. V.: Effect of addition of carbon nanofibers and carbon nanotubes on properties of thermoplastic biopolymers. Composites Science and Technology, **70**, 1095–1105 (2010).
DOI: 10.1016/j.compscitech.2010.02.015

eXPRESS Polymer Letters Vol.6, No.2 (2012) 129–141
Available online at www.expresspolymlett.com
DOI: 10.3144/expresspolymlett.2012.14

Investigation on the thermal properties of new thermo-reversible networks based on poly(vinyl furfural) and multifunctional maleimide compounds

C. Gaina[*], *O. Ursache, V. Gaina, E. Buruiana, D. Ionita*

Institute of Macromolecular Chemistry 'Petru Poni' Aleea Gr.Ghica Voda 41 A, RO-700487, Iasi, Romania

Received 24 June 2011; accepted in revised form 7 September 2011

Abstract. New thermo-reversible networks were obtained from poly(vinyl furfural) and multifunctional maleimide monomers by Diels-Alder (DA) and retro-DA reactions. The poly(vinyl furfural) having acetalization degree of 15 and 25% were obtained by the acid-catalyzed homogenous acetalization of poly(vinyl alcohol) with 2-furfural in a nonaqueous media. The thermal and viscoelastic behaviour of the cross-linked materials have been studied via differential scanning calorimetry, dynamic mechanical analysis and thermogravimetric analysis. The networks exhibit considerable swelling in those organic solvents that dissolve both poly(vinyl furfural) and bismaleimides; by heating in aprotic dipolar solvents at 150°C, they become soluble.

Keywords: *polymer synthesis, thermal properties, Diels-Alder polymers, networks*

1. Introduction

Inspired by the phenomenon of self-healing in biological systems, the synthesis of man-made self-healing polymeric materials has become a newly emerging paradigm and a fascinating area of research. The Diels-Alder reaction and its retro-Diels-Alder analogue represent a highly promising route to introducing self-healing properties to polymeric systems [1–5]. The search for various reversible reactions is a paramount importance for unlocking the potential of the conceptual framework of covalent constitutional dynamic chemistry [6]. The reversibility of DA reaction is widely applied to the preparation of remarkable polymers. Thermally-reversible DA reactions have been used in numerous studies including polymer synthesis from multifunctional monomers [4, 7–15] or by cross-linking of functional copolymers containing maleimide or furan pendant groups [16–22], surface modifications [16, 23], organic-inorganic polymer hybrids [24, 25], reversible crosslinking polymer chains/ gels [5, 16, 24, 26] and remendable/self-healing polymers [11, 12, 27]. Due to the fact that these reactions can proceed under mild conditions without a catalyst, this makes them attractive for designing covalently reversible bonds in which furan and maleimide functional groups are responsible for association and dissociation [28–31].

In this study, we report the preparation and characterization of thermo-reversible networks based on poly(vinyl furfural) and multifunctional maleimide compounds, as the basis for obtaining asymmetric membranes by the phase inversion method. Thermo-reversible nature of the Diels-Alder networks was characterized by FTIR, ^{1}H-NMR and by a heating-cooling cycle in differential scanning calorimetry (DSC) using a model compound based on poly(vinyl furfural) and mono-maleimide compound. The ther-

[*]Corresponding author, e-mail: gcost@icmpp.ro

mal and mechanical properties of the polymers were characterized by thermogravimetric analysis and dynamic mechanical analysis.

2. Experimental

2.1. Reagents and materials

Poly(vinyl alcohol) (**PVA**), white crystalline form (Aldrich reagent, viscosity-average molecular weight 77 000–79 000 containing 2% of acetate group), 2-furaldehyde, 99% (Aldrich, USA), dimethylformamide (DMF), dimethylsulfoxide (DMSO), polycaprolactone diol having numeric-average molecular weight of 1250 (Aldrich, USA), *p*-toluene sulfone acid (*p*-**TSA**) were used as received. 4-Maleimidobenzoyl chloride was synthesized as described in the literature [32].

4,4′-bismaleimidodiphenylmethane (**BMI-1**), 4,4′-bismaleimidodiphenyloxide (**BMI-2**) and 1,1′-hexamethylene bismaleimide (**BMI-3**) were synthesized from diamines (1 mol) and maleic anhydride (2 moles) in dry acetone according to a two-step method described in the literature [33].

2.1.1. Synthesis of bismaleimide (BMI-4) and maleimide (MI)

The bismaleimide containing urethane groups (**BMI-4**) was prepared by the addition reaction of 4-maleimidophenyl isocyanate with polycaprolactone diol having numeric-average molecular weight of 1250 (Aldrich, USA) according to a method described in our previous paper [34].

BMI-4, yellow wax from dichloromethane, yield 82%.

FTIR (KBr): 3323, 3085, 2947, 2865, 1735, 1707, 1608, 1534, 1462, 1398, 1314, 1240, 1160, 1105, 1070, 834, 689 cm^{-1}.

^{1}H-NMR ($CDCl_3$): δ = 7.55 (d, 4H, aromatic protons), 7.08 (d, 4H, aromatic protons), 6.80 (s, 4H, maleimide protons), 5.35 (s, 2H, NH proton), 4.05 (t, 20H, COOC$\underline{H}_2$), 3.75 (t, 4H, NHCOOC$\underline{H}_2$), 2.35 (t, 20H, C$\underline{H}_2$COO), 1.45 (m, 160H, C$\underline{H}_2$–CH_2–).

4-nonylphenyl 4-(2,5-dioxo-2,5-dihydro-1*H*-pyrrol-1-yl)benzoate (MI) was prepared by the reaction of 4-maleimidobenzoyl chloride with *p*-nonylphenol, in chloroform, in the presence of triethylamine. A typical procedure is presented below. To a solution of 4-maleimidobenzoyl chloride (0.01 mol, 2.35 g) in chloroform (40 ml) cooled at 0–5°C, triethylamine (1.4 ml) and *p*-nonylphenol (0.01 mol, 2.2 g) were added. The reaction mixture was stirred at 0–5°C for 2 hours, at room temperature for 2 hours and at reflux for 1 hour and then was filtered. The organic layer was washed with water. After removing of chloroform, 4 g of yellow wax product was obtained (yield 90%).

^{1}H-NMR ($CDCl_3$): δ = 8.24 (d, 2H, aromatic protons), 7.63 (d, 2H, aromatic protons), 7.38 (dd, 2H, aromatic protons), 7.23 (d, 2H, aromatic protons), 6.88 (s, 2H, maleimide protons), 1.70 (m, 2H, C$\underline{H}_2$), 1.38 (m, 14H, (C$\underline{H}_2$)$_7$) and 0.80 (t, 3H, C$\underline{H}_3$).

2.1.2. Synthesis of poly(vinyl furfural) (PVF)

PVF was prepared by acetalization of **PVA** in DMSO as solvent, in the presence of *p*-**TSA** according to a method described in literature [35–36]. The degree of acetalization was determined by ^{1}H-NMR spectra using Equation (1) [37]:

$$(FA) = \frac{2}{\frac{A_{CH_2}}{A_{H_5}} - 2} \tag{1}$$

where (*FA*) is the mol% of vinyl acetal, A_{CH_2} represents the total peak area of methylene protons and A_{H_5} represents peak area of the H_5 protons which appears at 7.6 ppm.

A typical procedure is presented below. **PVA** (11 g, 0.25 mol, based on –CH_2–CH–OH as unit) was dissolved in DMSO (200 ml) in a round bottom flask. Then, *p*-**TSA** (2 g, 1% w/v of the reaction medium) and 2-furaldehyde (10 ml, 0.12 mol) was added. The reaction mixture was heated and stirred at 60°C for 24 hours, then cooled at room temperature and poured in water. The solid was filtered, then washed well with water and finally dried in a vacuum oven at 60–65°C for 24 hours, yield 82%.

2.1.3. Synthesis of model compound (PVF-MI)

To a solution of **PVF-2** (0.5 g) in DMF (20 ml), **MI** (1.5 g) was added and stirred at 80°C for 8 hours. The solution was cooled and precipitated in water, then dried. The product was purified by dissolving in acetone and precipitation in water.

2.1.4. Preparation of cross-linked polymers *via* DA reaction of PVF with bismaleimide (BMI)

A mixture of **PVF** and **BMI** (2DS:1 by mols) was dissolved in DMF (10 ml) and stirred at 80–90°C

for 4 hours. The reaction solution was degassed in vacuum and quickly transferred to a glass plate, using a doctor blade (e = 1 mm). The solvent was evaporated in atmosphere at 80–90°C for 24 hours. The film was removed from the glass plate by soaking in cold water.

2.2. Measurements

The Fourier transform infrared (FTIR) spectra were recorded on a Bruker Vertex 70 Instruments (Austria) equipped with a Golden Gate single reflection ATR accessory, spectrum range 600–4000 cm^{-1}.

The proton nuclear magnetic resonance (^{1}H-NMR) spectra were recorded on a Bruker NMR spectrometer, Avance DRX 400 MHz (Rheinstteten, Germany), using DMSO-d_6 and $CDCl_3$ as solvents and tetramethylsilane as an internal standard.

Thermogravimetric analyse (TGA) was carried out in air atmosphere using a DERIVATOGRAF Q-1500 D apparatus (Hungary). The rate of TGA scans was 10°C/min. The initial weight of the samples was about 50 mg and the temperature range 30–700°C.

Differential scanning calorimetry (DSC) measurements were conducted on a DSC 200 F3 Maia (Netzsch, Germany). About 9 mg of sample were heated in pressed and punched aluminium crucibles at a heating rate of 10°C/minute. Nitrogen was used as inert atmosphere at a flow rate of 100 ml/minute. A Perkin Elmer DSC-7 differential scanning calorimeter (Massachusetts, USA) was used for thermal analysis and was operated at a heating rate of 10°C/min. Tests were conducted on samples of about 10 mg, which were gradually heated for observation of the glass-transition temperature.

Dynamic mechanical experiments (DMA) were made using a Diamond PerkinElmer instrument (Singapore) that applies a sinusoidal stress to the sample and measures the resulting strain. The force amplitude used was well within the linear viscoelastic range for all investigated samples. The thermomechanical properties were evaluated, starting from –100°C up to beyond the temperature corresponding to glass transition, at a heating rate of 2°C/min and a frequency of 1 Hz, under nitrogen atmosphere. The size of films was of 10 mm × 10 mm × 0.5 mm for the tension attachment.

Wide-angle X-ray diffractions (WAXD) of the polymers were recorded in a Bruker AD8 Advance diffractometer (Germany) using a Cu-K_α source, at room temperature.

3. Results and discussion

3.1. Characterization of PVF-(1,2)

By acetalization of **PVA** with furfural in DMSO in the presence of *p*-**TSA** was obtained **PVF** with the acetalization degree of 15% (**PVF-1**) and 25% (**PVF-2**). A typical ^{1}H-NMR spectrum for **PVF-2** is shown in Figure 1. The signals observed at 1.30–1.90, 3.83– 3.99, 5.57, 6.43 and 7.61 ppm are attributed to the methylene (–CH_2–), methine (–CH<), dioxymethine (–O–CH–O–) and furan ring protons, respectively.

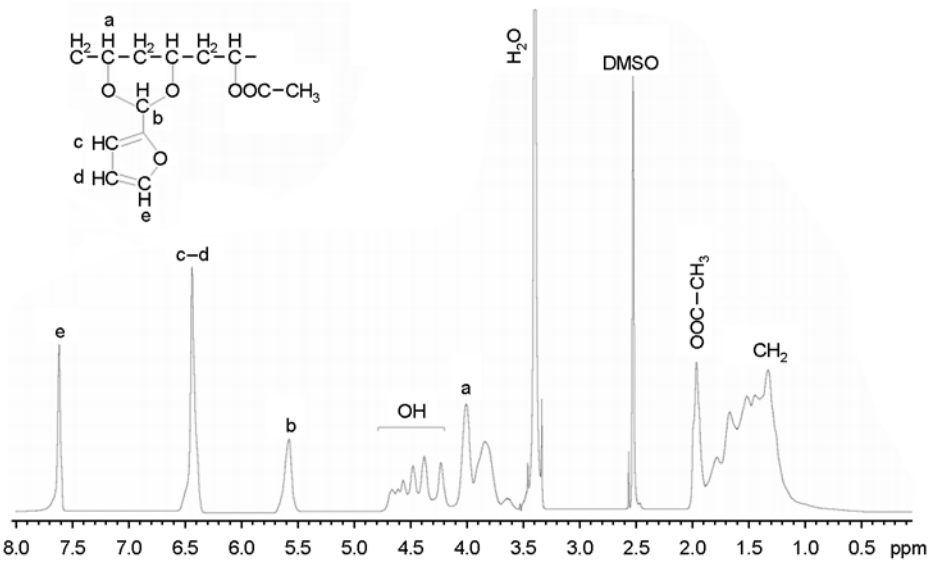

Figure 1. The ^{1}H-NMR spectrum for **PVF-2**

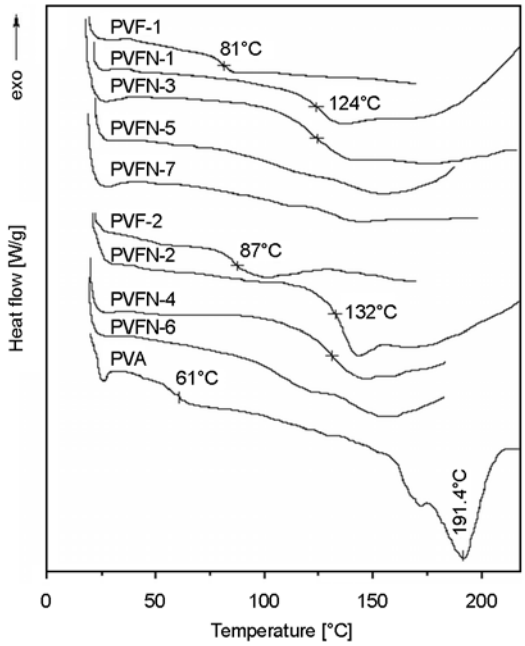

Figure 2. The DSC curves of **PVA**, **PVF** and **PVFN** films at second heating run films

The DSC measurements of **PVA** and **PVF** films are presented in Figure 2. The DSC scan of **PVA** shows a transition corresponding to the glass transition temperature at 61°C and an endothermic peak around 191°C attributed to the melting temperature

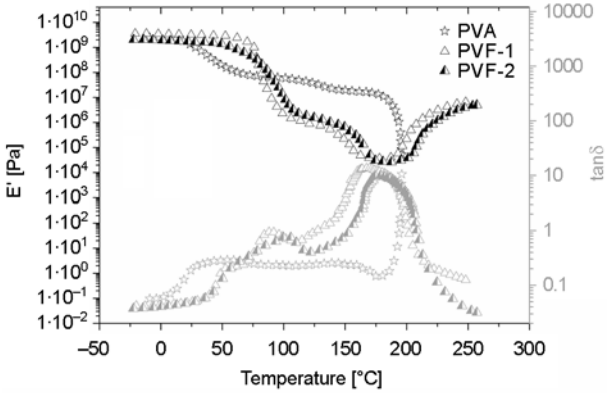

Figure 3. The storage modulus and dissipation factor tan δ profiles of **PVA**, **PVF-1** and **PVF-2** with frequency of 1 Hz

of **PVA**. The DSC scans of **PVF-1** and **PVF-2** show a transition temperature around 81 and 87°C, respectively. Glass transition temperature of **PVF** increases with the increase of acetalization degree [38].

The variations of the dynamic mechanical properties with temperature for **PVA**, **PVF-1** and **PVF-2** are presented in Figure 3. The viscoelastic results obtained for these three samples are summarized in Table 1. All three samples are characterized at low temperatures by a glassy behaviour. This was indicated by the relatively constant value of the storage

Table 1. Dynamic mechanical analysis of **PVF-(1-2)** and **PVFN-(1-8)**

Sample	DMA			Storage modulus at		
	T_g[a] [°C]	tan δ peak		20°C [MPa]	170°C [MPa]	250°C [MPa]
		Temperature [°C]	Height			
PVF-1	71.9	86.9; 163.8	0.93; 13.26	3063	0.039	6
PVFN-1	109.3	136; 180; 232	0.56; 0.25; 0.137	1910	3.250	532
PVFN-3	97.4	123.5; 178.6; 236	0.56; 0.26; 0.151	2019	3.311	1034
PVFN-5	68.2	87.4; 123; 168	0.65; 1.56; 3.50	596	0.096	1.72
PVFN-7	72.7	89.6; 168	0.51; 5.28	290	0.047	–
PVF-2	66.3	100.7; 178.8	0.77; 10.06	1728	0.027	0.263
PVFN-2	118.5	140.6; 156	0.408; 0.471	1781	4.455	108
PVFN-4	113.0	133; 179; 241	0.50; 0.20; 0.12	1412	4.099	161
PVFN-6	96.2	89.6; 124; 195	0.51; 0.78; 0.119	809	4.600	36.10
PVFN-8	40.0	74.2; 180	0.38; 4.65	101	0.017	4.40

[a]Glass transition temperature by DMA measurements, corresponded to onset temperature of the decrease in E'

Table 2. Dynamic mechanical data of **PVA**, **PVF-1** and **PVF-2**

Sample	$E' \cdot 10^9$[a] (≈-6°C) [Pa]	T_g of amorphous phase [°C]				tan δ of crystalline phase	
		E'_{onset}[b]	E''_{max}[c]	tan δ peak		T [°C]	Height
PVA	3.7	34.9	42.4	54.4		Shoulder 113–152	0.15
PVF-1	3.0	39.8; 71.9	46.3; 74.4	Shoulder 51.7	Peak 86.9	167.0	13.53
PVF-2	2.0	41.7	66.3 (broad peak)	58.7; 85.8	100.7	174.5	9.72

[a]Storage modulus corresponding to glass region;
[b]Glass transition temperature of sample by DMA measurement, corresponded to onset temperature of the decrease in E';
[c]Glass transition temperature of sample by DMA measurement, corresponded to maxim peak of E''

modulus whose magnitude is over 10^9 Pa (Table 2). In this region, the macromolecules are in frozen state, the polymers being stiff and glassy. As is depicted in the *E′–T* curve the rigidity of the three polymers in the glassy region decreases in the order: **PVA** > **PVF-1** > **PVF-2**. Consequently, the storage modulus diminishes as furfural content increases suggesting an increasing in mobility of macromolecular chains. The explanation is relative simple: by introduction of furfural units, the cleavage of the intra- and intermolecular hydrogen bonds between hydroxyl groups takes place, the rigidity induced by these bonds decreases, the free volume increases and the sample presents a more flexible structure.

The storage modulus of the **PVA** decreases with increasing temperature and drops at 13°C. The drop of *E′* and two peaks of *E″* and tan δ centred at 42.4 and 54.4°C, respectively can be attributed to the glass transition of the amorphous phase [39–41]. Moreover, the small decrease of *E′* modulus from $3 \cdot 10^9$ to $6 \cdot 10^7$ Pa, less than two orders of magnitude indicates the presence of restraints which impede the coordinated motion of macromolecular chains. These restraints could originate from the higher crystallinity of **PVA** which appeared as a result of planar zig-zag conformation. For **PVF-1** the two drops that appear on the *E′* curve at 39.8 and 71.9°C, the peaks on *E″* (46.3 and 74.4°C) and tan δ curve (51.7 and 86.9°C) indicate the presence of two relaxation phenomena (Table 2). A rapid drop of storage modulus of **PVF-2** from $1.6 \cdot 10^9$ to $1.7 \cdot 10^6$ Pa relates to the glass transition. The fall of the storage modulus is accompanied by a large peak on the *E″* curve with a maximum at 66.3°C. Analyzing the plot tan δ *versus* temperature in the range of 50–120°C a characteristic peak, centred at 100.7°C, was observed accompanied by two shoulders: one centred at 58.7°C and the other at 85.8°C.

The variation of tan δ as a function of temperature at a frequency of 1 Hz is represented in Figure 3. DMA spectra shows a shift of the α peak to higher temperatures with increasing furfural content and a reduction of relaxation strength from 0.93 in the case of **PVF-1** to 0.77 in the case of **PVF-2**. Taking into account that the height of tan δ peak is governed by the molecular mobility there can be concluded that with increasing furfural content a diminution in mobility appears.

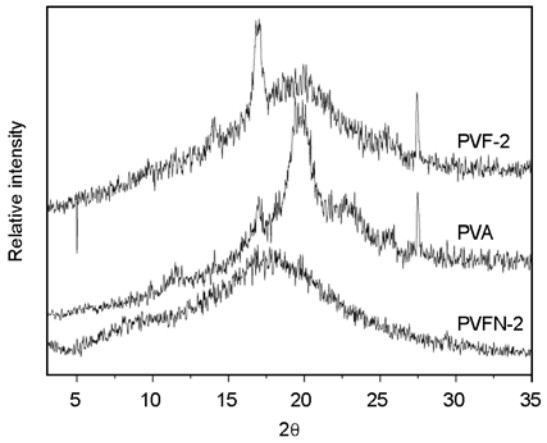

Figure 4. XRD patterns of the **PVA**, **PVF-2** and **PVFN-2**

At a temperature higher than 100°C, literature studies mention two relaxations of the crystalline phase at 135 and 237°C, respectively. The first one is attributed to the local relaxation of the crystalline phase, while the second one is caused by the melting of the crystalline domains [39–41]. In our case the first peak of PVA is shifted to higher temperatures (147.6°C), while the melting of the crystalline domains could not be observed. In **PVF-1** and **PVF-2** there is an increase in the tan δ temperature at which this relaxation appears, as well as a decrease in strength with increasing furfural content. A possible explanation consist of the restrictive molecular motions appeared as a result of the crosslinking reactions confirmed by the abrupt increase of the storage modulus at temperatures higher than 190°C. Since the furfural rings do not fit into the crystal lattice of **PVA**, the degree of crystallinity decreases. The (unreacted) hydroxyl functions, which are distributed randomly as well, can only lead to a very limited degree of crystallinity in **PVF**. This explanation is confirmed by wide-angle X-ray diffraction (WAXD) measurements (see Figure 4). The peak with $\theta = 19.8°$ corresponds to the (110) reflection, i.e., a plane containing the planar zigzag chain direction of the crystallites.

3.2. Characterization of PVFN networks

DA cycloaddition reaction was used in cross-linking poly(vinyl furfural) with multifunctional maleimide (Figure 5). The DA reaction was carried out between **PVF-1** or **PVF-2** and bismaleimide monomers (**BMI**). The furan rings in the **PVF-1** or **PVF-2**, part of the polymer, and the maleimide

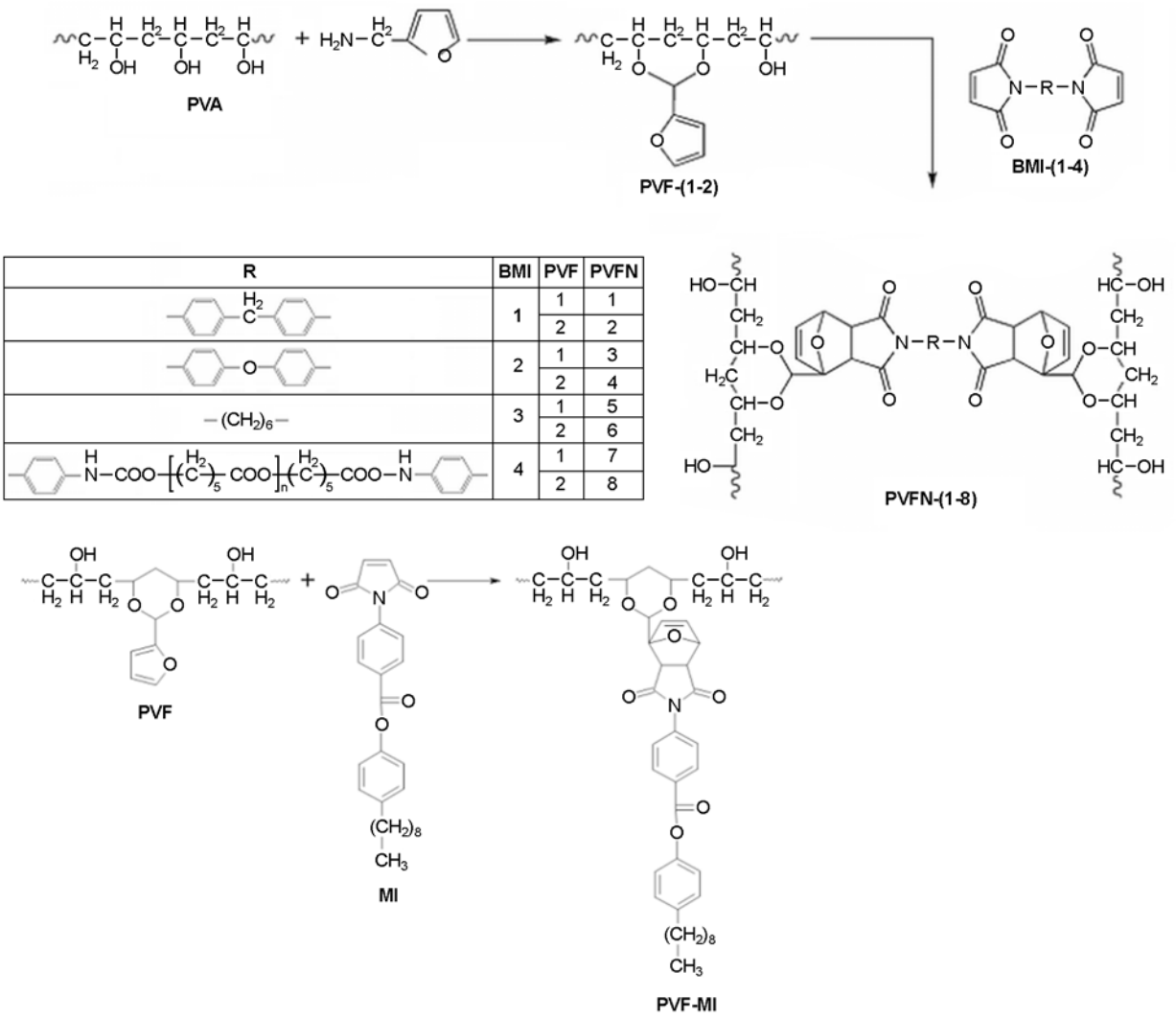

Figure 5. Synthesis of networks **PVFN-(1-8)**

group in the **BMI** acted as the diene and dienophile, respectively. Stoichiometric quantities of **PVF-1** and **BMI** (2:1 mols) were dissolved in DMF and stirred at 80–90°C for 4 hours. The reaction mixture was degassed and transferred to a glass plate and the solvent was evaporated at 80–90°C for 24 hours. The film was removed from the glass plate by soaking in cold water. Figure 6 represents the ATR-FTIR spectra of the **PVF-1** and their network materials. The spectrum of **PVF-1** shows characteristic peaks at 1506 cm^{-1} (C=C in furan ring), 1103 cm^{-1} (C–O in furan ring), 1004 cm^{-1} (furan ring breathing) and 750 cm^{-1} (monosubstituted furan ring) [12]. The ATR-FTIR spectrum of networks shows a new absorption band about 1776 cm^{-1} attributed to the existence of DA adduct from the reaction between furan and maleimide groups [12, 42] and at 1190 cm^{-1} assigned to ν_{C-N-C} from cycoadduct. The strong absorption of the >C=O stretching shifted from 1730 cm^{-1} (in **PVF-1**) to 1705 cm^{-1} (in network) due to the interaction between **PVF** and bismaleimide.

The **PVFN-(1-8)** network materials are not soluble in those organic solvents that dissolve both **PVF** and **BMI**, but they swell in them. By heating of **PVFN-(1-8)** in aprotic dipolar solvents (DMF, NMP or DMSO) at 150°C for 30–60 minutes, they become soluble. For example, a fluid solution of **PVFN-8** in DMF (5 wt%) formed by retro-DA reaction of network in DMF at 150°C for 1 hour (Figure 7a) becomes gel by maintaining it at 80°C for 3 hours (Figure 7b).

3.2.1. Thermal properties

The thermo-reversible properties of network materials are characterized by DSC analysis. Typical

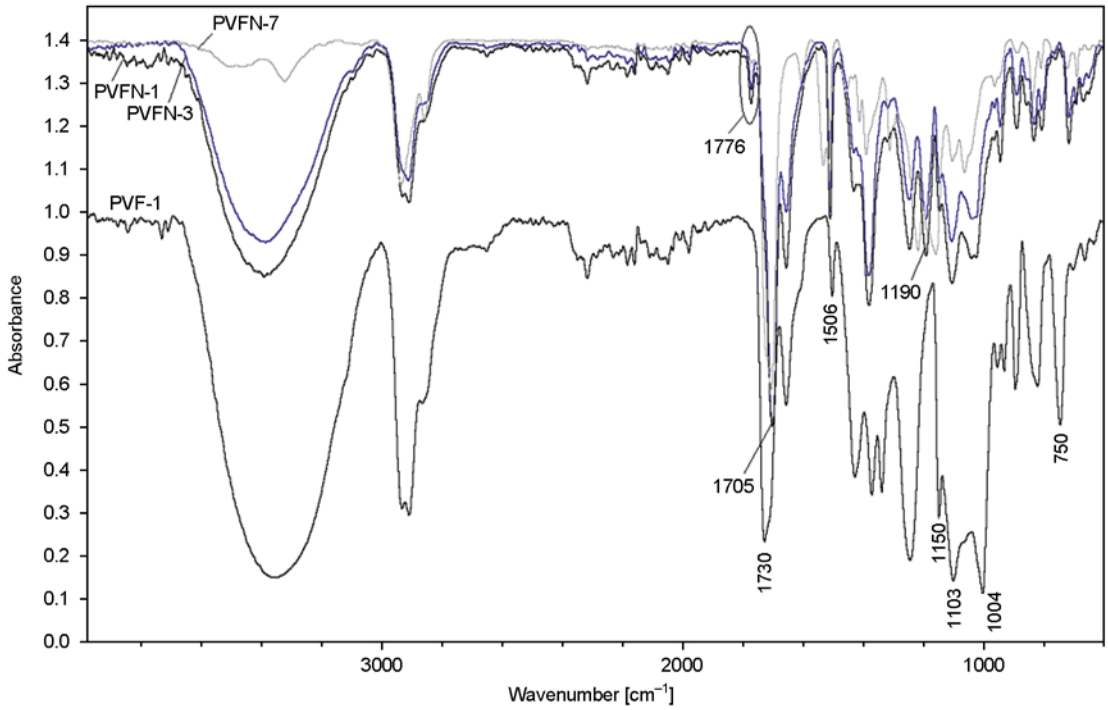

Figure 6. The ATR-FTIR spectra of the **PVF-1** and their network materials

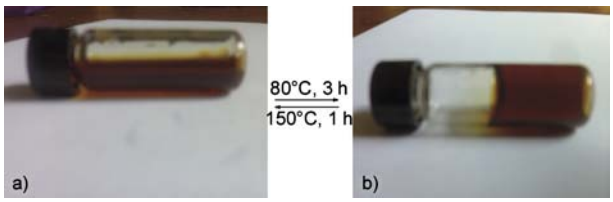

Figure 7. Photograph of observation of the thermally reversible cross-linking behaviour of **PVFN-8**

dynamic DSC curves of **PVF** and **BMI** systems are presented in Figure 2. As can be seen, in the case of polymers based on **BMI-(1,2)** with a higher rigidity, T_g shifts to higher values and the retro-DA process overlaps with the glass transition. The polymers based on **BMI-(3,4)** present lower T_g and the retro-DA process takes place after the glass transition.

To facilitate the investigation by ^{1}H-NMR spectroscopy of the DA and retro-DA reactions of poly (vinyl furfural) with maleimide, a model compound was synthesized by the reaction of **PVF-2** and mono-maleimide compound (**MI**) (Figure 5). The ^{1}H-NMR spectrum of model compound shows in addition to the chemical shifts characteristic to the **PVF** structure, and signals attributed to maleimide organic rest at 0.80–1.70, 6.88, 7.38, 7.63 and 8.24 ppm due to CH_3 and CH_2 protons from nonyl rest and aromatic protons and at 6.60, 5.37, 5.28 and 3.10–3.30 ppm corresponding to the protons of maleimide-furan cycloadduct (Figure 8a). By heating the solution at 150°C for 30 minutes, the ^{1}H-NMR spectrum shows the disappearance of chemical shifts characteristic to the cycloadduct protons and the appearance of new signals at 7.20, 7.55 and 6.41 ppm attributed to the maleimide and furan protons indicating that the retro-DA reaction occurred entirely (Figure 8b). By cooling the sample at room temperature there can be observed the partial recovery of cycloadduct (Figure 8c). Maintaining the sample at 80°C for 3 hours leads to total recovery of cycloadduct.

Retro-DA and DA reactions were also studied by DSC measurements, applying heating-cooling cycles for **PVF-MI** (Figure 9a). The h1 curve shows the first heating cycle of the cross-linked **PVF-MI** heated at 50–180°C with a heating rate of 10°C/min. It has an inflexion around 98°C attributed to the glass transition temperature of sample and a large endothermic peak at 143°C which indicated the cleavage of the DA cycloadduct. In the second (h2) and the third (h3) heating run the compound has the same behaviour as in the first one, this fact being a proof of it's thermo-reversible nature. The increase of the glass transition temperature from 98°C for the first heating run to 99°C for the third heating cycle is probably due to the dehydration reactions of PVF polymer.

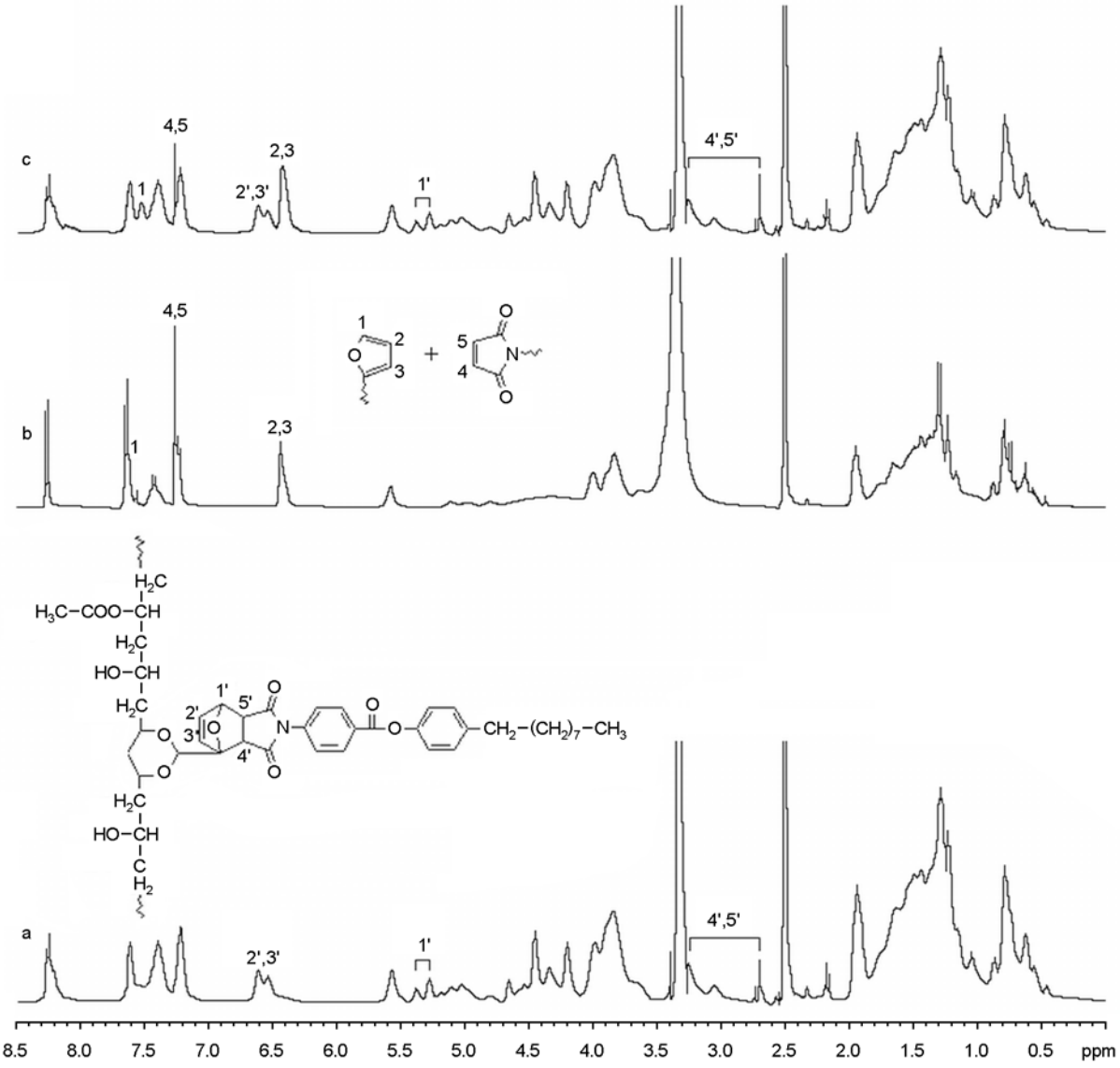

Figure 8. The ^{1}H-NMR spectrum for model compound: a) adduct of **PVF-2** and **MI**; b) retro-DA product obtaining by heating the adduct at 150°C for 30 minutes; c) after cooling at room temperature

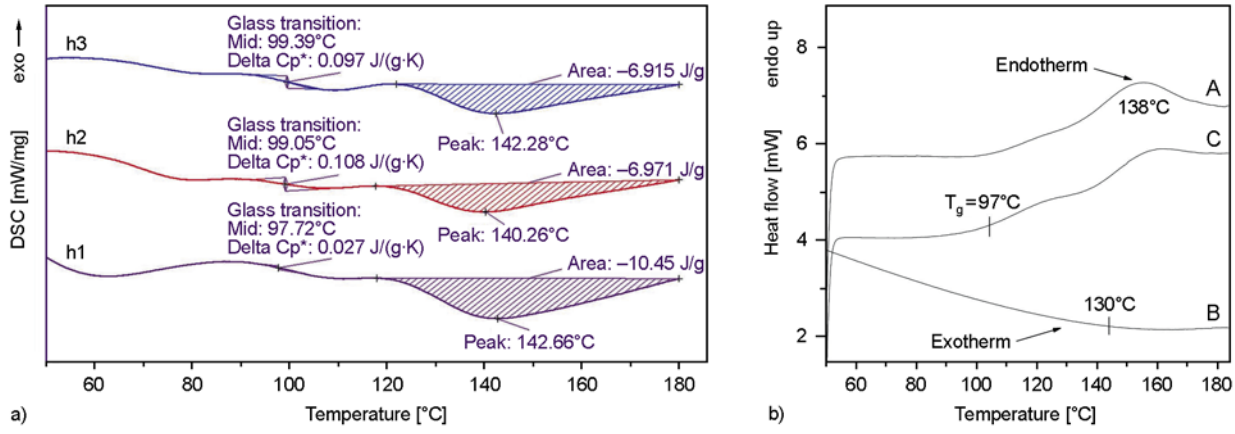

Figure 9. The DSC curves of model compound (a) (h1 – the first heating run; h2 – the second heating run and h3 –the third heating run) and **PVFN-8** (b) (A – first heating; B – cooling; C – second heating)

Figure 9b shows the heating and cooling curves of DSC analysis of the **PVFN-8** polymer. The curve 'A' shows the first heating cycle of the cross-linked polymer heated at 50 to 165°C. It has an endothermic peak at 138°C, which indicated the cleavage of the DA cross-links. The curve 'B' shows the cooling curve of the polymer. It shows a broad exothermic peak at 103–161°C (centering at about 130°C) due to the covalent bond formation between furan and maleimide moieties, as the samples come closer on cooling and then finally reconnect very efficiently. The curve 'C' shows the second heating cycle of the DA cross-linked polymer. It also shows the same observation in the first heating cycle. It clearly indicates that the Diels-Alder crosslinked polymer (**PVFN-8**) is thermoreversible. The T_g of the **PVFN-8** polymer at 97°C was determined from the second heating cycle of the polymers and are shown in Figure 9. The shifting of T_g from 87°C (**PVF-2**) to 97°C is due to the DA cross-linked between **PVF-2** and **BMI-4**.

The occurrence of the retro-DA reaction was also observed with ATR-FTIR. Figure 10a–c shows the ATR-FTIR spectra of **PVFN-8** network film before heating at 150°C (Figure 10a), after heating at 150°C (Figure 10b) and after maintaining at 80°C for 3 h (Figure 10c). The **PVFN-8** film spectrum (Figure 10a) evidences the intense absorption bands at 1709 and 1730 cm^{-1} attributed to C=O stretching from urethane, ester or imide groups, 1536 cm^{-1} (amide II), 1395 cm^{-1} (C–N–C), 1220 cm^{-1} (amide III) and 1159 cm^{-1} (C–O–C). The peak at 1776 cm^{-1} is attributed to the maleimide-furan cycloadduct [38]. The spectrum ATR-FTIR of **PVFN-8** after heating at 150°C (Figure 10b) presents a shift of absorption band characteristic to C=O stretching from 1709 to 1711 cm^{-1} and the disappearance of the absorption bands at 1776 cm^{-1} attributed to the cycloadduct and at 1190 cm^{-1} corresponding to C–N–C (succinimide structure). The absorption band of amide II shifted to 1520 cm^{-1}. The ATR-FTIR spectrum of network film after cooling at room temperature (Figure 10c) is identical to the initial spectrum.

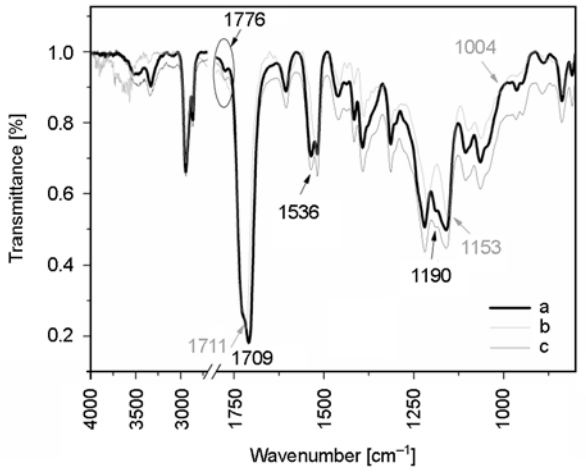

Figure 10. The ATR-FTIR spectra of **PVFN-8**: a) initial; b) heated at 150°C; c) and after maintaining at 80°C for 3 h

In addition to the ATR-FTIR and DSC study, DMA was also employed to examine thermal behavior of the network materials. In Figures 11 and 12, the storage modulus (E') and dissipation factor ($\tan\delta$) curves of networks based on **PVF** and **BMI**, are plotted against temperature, and their data are presented in Table 1. As in DSC, DMA curves of the networks based on **BMI-(1,2)** show a single drop

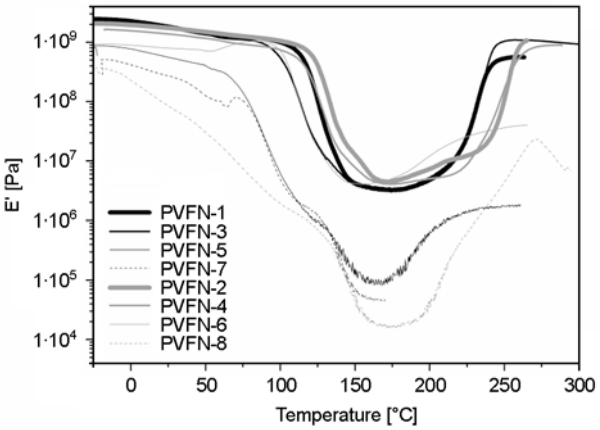

Figure 11. Storage modulus curves of **PVFN** networks based on **PVF-1** (black line) and **PVF-2** (grey line) with frequency of 1 Hz (with a heating rate of 2°C/min)

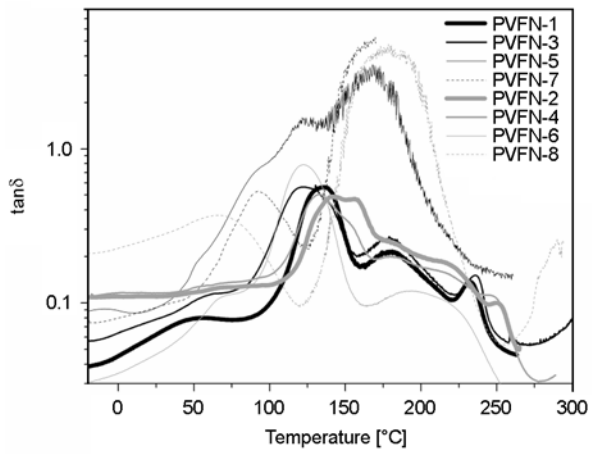

Figure 12. Dissipation factor $\tan\delta$ curves of **PVFN** networks with frequency of 1 Hz

Table 3. The thermogravimetric data of **PVA**, **PVF** and **PVFN**

Sample	Decomposition temperature range (weight loss) [°C] ([%])			
	Stage I	Stage II	Stage III	Stage IV
PVA	20–232 (3)	260–385 (42)	385–470 (26.8)	470–630 (16.8)
PVF-1	20–240 (3)	240–300 (28.5)	300–370 (22)	370–500 (20); 510–670 (20)
PVFN-1	20–235 (3)	235–380 (25)	389–500 (28)	500–680 (42)
PVFN-3	20–235 (2)	245–405 (32)	405–520 (22)	520–720 (36)
PVFN-5	20–240 (2)	245–395 (33)	410–505 (29)	510–700 (36)
PVFN-7	20–200 (2)	210–406 (37)	400–530 (23)	530–700 (30)
PVF-2	20–235 (2)	240–370 (43)	370–500 (21)	500–630 (29)
PVFN-2	20–265 (5)	270–400 (20)	400–515 (26)	515–700 (40)
PVFN-4	20–270 (1.5)	270–403 (20)	405–510 (25)	515–720 (38)
PVFN-6	20–245 (1.5)	250–400 (30)	405–510 (27)	515–710 (40)
PVFN-8	20–220 (1.5)	230–395 (36)	400–530 (21)	530–700 (31)

attributed to the glass transition which overlaps with the retro-DA reaction and varied between 97.4 and 118.5°C (Table 1). The DMA curves of networks based on **BMI-(3,4)** show a decrease in two stages, first step is due to the glass transition and the second stage is assigned to the retro-DA reaction. This behaviour is concordance with the DSC diagrams (Figure 2) where the networks based on **BMI-(1-2)** presented a single inflexion while the networks based on **BMI-(3,4)** showed two inflexion points. The storage modulus of networks recovers above 200°C due to the thermal crosslinking reactions of the resulted bismaleimide from retro-DA reactions and partial dehydration of **PVA** accompanied by polyene formation [43]. Figure 12 illustrated the temperature dependence of tan δ for **PVFN-(1-8)** networks. Indeed, the relaxation process of networks appears structured into two components that can be tentatively attributed to the glass transition temperature of networks and retro-DA reactions. The second transition become prevailing for networks based on **BMI-(3,4)** due to length of aliphatic chains of bismaleimide groups.

By processing TGA curves, thermal data presented in Table 3 resulted. The synthesized networks exhibited a four-step thermo-degradation curve. The weight loss at 20–265°C (in the first stage of decomposition) could be due to the residual solvents in the polymers (DMF and water). The second stage of decomposition ranged between 210–406°C with a weight loss of 20– 36% corresponding to the elimination of water molecules from **PVF** chains [44] and acetic acid from acetate groups. In the third stages of decomposition, the breakdown of the polymer backbone takes place in the range of 389–530°C with a weight loss of 21– 29%. Specifically, it can be assigned to the degradation of nonconjugated polyene. The main decomposition of this process takes place in the range of 500–720°C corresponding to the weight loss of 31–42%.

3.2.2. Water absorption of networks

The water absorption property of the samples was tested by their immersion in distilled water for 100 hours. Specimens were drawn, and the surface water was removed using a tissue paper and weighted to an accuracy of 0.001 g. The water absorption versus time is plotted in Figure 13. As can be seen from figure, the moisture absorption of **PVF-2**-based networks (having acetalization degree of 25%) is considerably smaller than that of the series based on **PVF-1**.

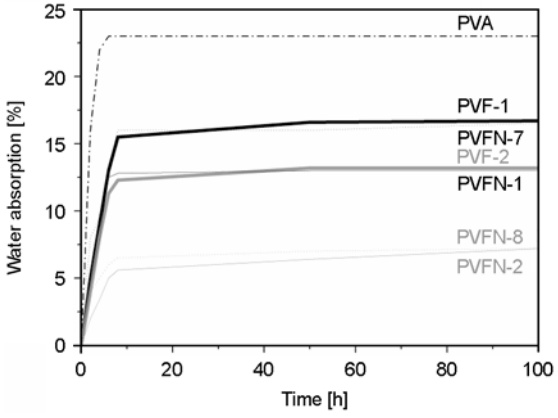

Figure 13. The water absorption versus time of the **PVA**, **PVF** and **PVFN**

4. Conclusions

Two series of polymers based on PVA modified with 2-furaldehyde have been synthetized and characterized using ATR-FTIR, ^{1}H-NMR, DSC, DMA, TGA analysis. The acetalization of **PVA** increases

T_g, value that increases more by cross-linking with **BMI**. The reversible nature of the cross-linked polymer was confirmed by ATR-FTIR spectroscopy and DSC analysis. In the DSC experiments the **PVF-BMI** system shows a clear endotherm during heating, indicating the cleavage of the inter-monomer linkages; they also show an exotherm during cooling, indicating reconnection of the dienes and dienophiles. This hypothesis was corroborated by ATR-FTIR analysis during the heating/cooling cycle and DMA measurements. The E' curves for networks based on **BMI-(1,2)** show a single drop attributed to the glass transition which overlaps with the retro-DA reaction, while DMA curves of networks based on **BMI-(3,4)** exhibit a two-stage decrease, first stage is attributed to the glass transition of polymers and the second stage is attributed to the retro Diels-Alder reaction.

High acetalization degree of **PVF** played an important role in reducing moisture absorption of the networks.

References

[1] Bergman S. D., Wudl F.: Re-mendable polymers. in 'Self healing materials: An alternative approach to 20 centuries of materials science' (ed.: van der Zwaag S.) Springer, Dordrecht, 45–68 (2007).

[2] Bergman, S. D., Wudl F.: Mendable polymers. Journal of Materials Chemistry, **18**, 41–62 (2008). DOI: 10.1039/B713953P

[3] Goiti E., Huglin M. B., Rego J. M.: Some properties of networks produced by the Diels–Alder reaction between poly(styrene-co-furfuryl methacrylate) and bismaleimide. European Polymer Journal, **40**, 219–226 (2004). DOI: 10.1016/j.eurpolymj.2003.09.017

[4] Wu D. Y., Meure S., Solomon D.: Self-healing polymeric materials: A review of recent developments. Progress in Polymer Science, **33**, 479–522 (2008). DOI: 10.1016/j.progpolymsci.2008.02.001

[5] Chen X., Dam M. A., Ono K., Mal A., Shen H., Nutt S. R., Sheran K., Wudl F.: A thermally re-mendable cross-linked polymeric material. Science, **295**, 1698–1702 (2002). DOI: 10.1126/science.1065879

[6] Boul P. J., Reutenauer P., Lehn J-M.: Reversible Diels–Alder reactions for the generation of dynamic combinatorial libraries. Organic Letters, **7**, 15–18 (2005). DOI: 10.1021/ol048065k

[7] Mcelhanon J. R., Russick E. M., Wheeler D. R., Loy D. A., Aubert J. H.: Removable foams based on an epoxy resin incorporating reversible Diels–Alder adducts. Journal of Applied Polymer Science, **85**, 1496–1502 (2002). DOI: 10.1002/app.10753

[8] Chen X., Wudl F., Mal A. K., Shen H., Nutt S. R.: New thermally remendable highly cross-linked polymeric materials. Macromolecules, **36**, 1802–1807 (2003). DOI: 10.1021/ma0210675

[9] Goiti E., Heatley F., Huglin M. B., Rego J. M.: Kinetic aspects of the Diels–Alder reaction between poly (styrene-co-furfuryl methacrylate) and bismaleimide. European Polymer Journal, **40**, 1451–1460 (2004). DOI: 10.1016/j.eurpolymj.2004.01.036

[10] Watanabe M., Yoshie N.: Synthesis and properties of readily recyclable polymers from bisfuranic terminated poly(ethylene adipate) and multi-maleimide linkers. Polymer, **47**, 4946–4952 (2006). DOI: 10.1016/j.polymer.2006.05.036

[11] Liu Y-L., Hsieh C-Y.: Crosslinked epoxy materials exhibiting thermal remendablility and removability from multifunctional maleimide and furan compounds. Journal of Polymer Science Part A: Polymer Chemistry, **44**, 905–913 (2006). DOI: 10.1002/pola.21184

[12] Tian Q., Rong M. Z., Zhang M. Q., Yuan Y. C.: Synthesis and characterization of epoxy with improved thermal remendability based on Diels–Alder reaction. Polymer International, **59**, 1339–1345 (2010). DOI: 10.1002/pi.2872

[13] Tian Q., Yuan Y. C., Rong M. Z., Zhang M. Q.: A thermally remendable epoxy resin. Journal of Materials Chemistry, **19**, 1289–1296 (2009) DOI: 10.1039/B811938D

[14] Ishida K., Yoshie N.: Two-way conversion between hard and soft properties of semicrystalline cross-linked polymer. Macromolecules, **41**, 4753–4757 (2008). DOI: 10.1021/ma8008383

[15] Aumsuwan N., Urban M. W.: Reversible releasing of arms from star morphology polymers. Polymer, **50**, 33–36 (2009). DOI: 10.1016/j.polymer.2008.10.048

[16] Gousé C., Gandini A., Hodge P.: Application of the Diels–Alder reaction to polymers bearing furan moieties. 2. Diels–Alder and retro-Diels–Alder reactions involving furan rings in some styrene copolymers. Macromolecules, **31**, 314–321 (1998). DOI: 10.1021/ma9710141

[17] Goiti E., Huglin M. B., Rego J. M.: Some observations on the copolymerization of styrene with furfuryl methacrylate. Polymer, **42**, 10187–10193 (2001). DOI: 10.1016/S0032-3861(01)00577-8

[18] Goiti E., Huglin M. B., Rego J. M.: Thermal breakdown by the retro Diels–Alder reaction of crosslinking in poly[styrene-*co*-(furfuryl methacrylate)]. Macromolecular Rapid Communications, **24**, 692–696 (2003). DOI: 10.1002/marc.200350013

[19] Gheneim R., Perez-Berumen C., Gandini A.: Diels–Alder reactions with novel polymeric dienes and dienophiles: Synthesis of reversibly cross-linked elastomers. Macromolecules, **35**, 7246–7253 (2002). DOI: 10.1021/ma020343c

[20] Kavitha A. A., Singha N. K.: A tailor-made polymethacrylate bearing a reactive diene in reversible Diels–Alder reaction. Journal of Polymer Science Part A: Polymer Chemistry, **45**, 4441–4449 (2007). DOI: 10.1002/pola.22195

[21] Liu Y-L., Chen Y-W.: Thermally reversible cross-linked polyamides with high toughness and self-repairing ability from maleimide- and furan-functionalized aromatic polyamides). Macromolecular Chemistry and Physics, **208**, 224–232 (2007). DOI: 10.1002/macp.200600445

[22] Kavitha A. A., Singha N. K.: Atom-transfer radical copolymerization of furfuryl methacrylate (FMA) and methyl methacrylate (MMA): A thermally-amendable copolymer. Macromolecular Chemistry and Physics, **208**, 2569–2577 (2007). DOI: 10.1002/macp.200700239

[23] Zhu J., Kell A. J., Workentin M. S.: A retro-Diels–Alder reaction to uncover maleimide-modified surfaces on monolayer-protected nanoparticles for reversible covalent assembly. Organic Letters, **8**, 4993–4996 (2006). DOI: 10.1021/ol0615937

[24] Imai Y., Itoh H., Naka K., Chujo Y.: Thermally reversible IPN organic–inorganic polymer hybrids utilizing the Diels–Alder reaction. Macromolecules, **33**, 4343–4346 (2000). DOI: 10.1021/ma991899b

[25] Adachi K., Achimuthu A. K., Chujo Y.: Synthesis of organic–inorganic polymer hybrids controlled by Diels–Alder reaction. Macromolecules, **37**, 9793–9797 (2004). DOI: 10.1021/ma0400618

[26] Liu Y-L., Hsieh C-Y., Chen Y-W.: Thermally reversible cross-linked polyamides and thermo-responsive gels by means of Diels–Alder reaction. Polymer, **47**, 2581–2586 (2006). DOI: 10.1016/j.polymer.2006.02.057

[27] Zhang Y., Broekhuis A. A., Picchioni F.: Thermally self-healing polymeric materials: The next step to recycling thermoset polymers? Macromolecules, **42**, 1906–1912 (2009). DOI: 10.1021/ma8027672

[28] Teramoto N., Arai Y., Shibata M.: Thermo-reversible Diels–Alder polymerization of difurfurylidene trehalose and bismaleimides. Carbohydrate Polymers, **64**, 78–84 (2006). DOI: 10.1016/j.carbpol.2005.10.029

[29] Gandini A., Coelho D., Silvestre A. J. D.: Reversible click chemistry at the service of macromolecular materials. Part 1: Kinetics of the Diels–Alder reaction applied to furan–maleimide model compounds and linear polymerizations. European Polymer Journal, **44**, 4029–4036 (2008). DOI: 10.1016/j.eurpolymj.2008.09.026

[30] Jegat C., Mignard N.: Effect of the polymer matrix on the thermal behaviour of a furan-maleimide type adduct in the molten state. Polymer Bulletin, **60**, 799–808 (2008). DOI: 10.1007/s00289-008-0913-y

[31] Canadell J., Fischer H., De With G., Van Benthem R. A. T. M.: Stereoisomeric effects in thermo-remendable polymer networks based on Diels–Alder crosslink reactions. Journal of Polymer Science Part A: Polymer Chemistry, **48**, 3456–3467 (2010). DOI: 10.1002/pola.24134

[32] Mikroyannidis J. A.: Thermostable laminating resins based on aromatic diketone bis- and tetramaleimides. Journal of Polymer Science Part A: Polymer Chemistry, **28**, 679–691 (1990). DOI: 10.1002/pola.1990.080280317

[33] Cristea M., Gaina C., Gheorghiu Ionita D., Gaina V.: Dynamic mechanical analysis on modified bismaleimide resins. Journal of Thermal Analysis and Calorimetry, **93**, 69–76 (2008). DOI: 10.1007/s10973-007-8802-4

[34] Gaina V., Gaina C., Sava M., Stoleriu A., Rusu M.: Bismaleimide resins containing urethanic moieties. Journal of Macromolecular Science Part A: Pure and Applied Chemistry, **34**, 2435–2449 (1997). DOI: 10.1080/10601329708010058

[35] Gousse C., Gandini A.: Acetalization of polyvinyl alcohol with furfural. European Polymer Journal, **33**, 667–671 (1997). DOI: 10.1016/S0014-3057(96)00234-0

[36] Chetri P., Dass N. N.: Synthesis of poly(vinyl benzal) from poly(vinyl alcohol) in nonaqueous medium. Journal of Applied Polymer Science, **62**, 2139–2145 (1996). DOI: 10.1002/(SICI)1097-4628(19961219)62:12<2139::AID-APP16>3.0.CO;2-0

[37] Fernández M. D., Fernández M. J., Hoces P.: Poly(vinyl acetal)s containing electron-donor groups: Synthesis in homogeneous phase and their thermal properties. Reactive and Functional Polymers, **68**, 39–56 (2008). DOI: 10.1016/j.reactfunctpolym.2007.10.012

[38] Adriaensens P., Pollers I., Carleer R., Vanderzande D., Gelan J.: Solid-state NMR study of different types of poly(vinyl formal). Macromolecules, **32**, 440–447 (1999). DOI: 10.1021/ma981216c

[39] Cerrada M. L., Benavente R., Pérez E., Pereña J. M.: The effect of orientation on the morphology and viscoelastic response of vinyl alcohol-ethylene copolymers. Macromolecular Chemistry and Physics, **201**, 1858–1868 (2000).
DOI: 10.1002/1521-3935(20000901)201:14<1858::AID-MACP1858>3.0.CO;2-A

[40] Park J-S., Park J-W., Ruckenstein E.: On the viscoelastic properties of poly(vinyl alcohol) and chemically crosslinked poly(vinyl alcohol). Journal of Applied Polymer Science, **82**, 1816–1823 (2001).
DOI: 10.1002/app.2023

[41] Park J-S., Park J-W., Ruckenstein E.: A dynamic mechanical and thermal analysis of unplasticized and plasticized poly(vinyl alcohol)/methylcellulose blends. Journal of Applied Polymer Science, **80**, 1825–1834 (2001).
DOI: 10.1002/app.1278

[42] Tian Q., Rong M. Z., Zhang M. Q., Yuan Y. C.: Optimization of thermal remendability of epoxy via blending. Polymer, **51**, 1779–1785 (2010).
DOI: 10.1016/j.polymer.2010.02.004

[43] Shaulov A. Yu., Lomakin S. M., Zarkhina T. S., Rakhimkulov A. D., Shilkina N. G., Muravlev Yu. B., Berlin Al. Al.: Carbonization of poly(vinyl alcohol) in blends with boron polyoxide. Doklady Physical Chemistry, **403**, 154–158 (2005).
DOI: 10.1007/s10634-005-0048-x

[44] Alexy P., Káchová D., Kršiak M., Bakoš D., Šimková B.: Poly(vinyl alcohol) stabilisation in thermoplastic processing. Polymer Degradation and Stability, **78**, 413–421 (2002).
DOI: 10.1016/S0141-3910(02)00177-5

eXPRESS Polymer Letters Vol.6, No.2 (2012) 142–147
Available online at www.expresspolymlett.com
DOI: 10.3144/expresspolymlett.2012.15

A simple way of improving graphite nanoplatelets (GNP) for their incorporation into a polymer matrix

H. Persson[*], *Y. Yao, U. Klement, R. W. Rychwalski*

Chalmers University of Technology, Department of Materials and Manufacturing Technology, Göteborg, Sweden

Received 30 May 2011; accepted in revised form 13 September 2011

Abstract. A simple method of solvent exfoliation/refining of direct-graphite nanoplatelets for their better incorporation into a polymer matrix is presented. We demonstrate the method for polystyrene. The method relies on sonication in N-methyl-2-pyrrolidone solvent, with surfactant assistance. A small amount of polystyrene is added to the solvent in order to increase the viscosity, this enhancing the exfoliation process and resulting in formation of a polymeric layer on graphene for its better incorporation in the polymer matrix. Polystyrene-coated thin graphene stacks form a stable dispersion, while thicker graphite nanoplatelets settle out. Thus bulk separation of thin and thick graphene stacks takes place.
The polystyrene-coated thin graphene stacks are studied using Transmission Electron Microscopy in two ways: (i) we calculate the number of graphene layers forming thin graphene stacks, and (ii) we employ Selected Area Diffraction to confirm our image analysis results by checking the intensity ratio (1100) and (2100) deflections in the diffraction patterns. Five layers is found to be the cut-off number, that is there are no stacks >5 layers, and 3 layer stacks are dominantly present. The average largest in-plane dimension is found to be approximately 2.5 μm (reduction by 50%).

Keywords: *nanocomposites, solvent dispersion, graphene*

1. Introduction

Graphene has triggered off further expectations in nanocarbon polymer composites, and enthusiasm in the research community. However, at present, only minute amounts of single monolayer graphene from 'bottom-up' production is available. For nanocomposites, massive amounts of graphene is needed. In our work we use direct-graphite nanoplatelets (GNP), now becoming increasingly available. Attractiveness of the material stems among others from the low cost of graphite, the precursor for GNP. Indeed, price of GNP is low compared to e.g., multiwall carbon nanotubes (MWNT). It is well known that the quality of polymer nanocomposites hinges on the quality of the filler. In the case of graphene based filler, this first of all refers to well-defined and small thickness.

The need for well-defined exfoliated GNP has been emphasized in the literature, and efficient ways to address the problem have been presented. Green and Hersam [1, 2] used density gradient ultracentrifugation, and achieved separation in graphene stacks by the number of layers. Sun *et al.* [3] used density gradient ultracentrifugal rate separation, and achieved sorting by sheet size and surface chemistry. In above works, a density gradient is essential, although in report [3] results for a uniform medium column are also included. The authors prepared a separate external measuring uniform density column, and found that separation was achievable over a smaller size range. Methods to exfoliate powdered graphite have been developed by Coleman and collaborators, among others in [4, 5], and by Bourlinos *et al*. [6], as well as Blake *et al*. [7].

[*]Corresponding author, e-mail: henrik.persson@chalmers.se

Simultaneously, research into various types of graphite nanoplatelets, such as graphene oxide (GO) [8, 9], chemically modified graphene [10], and thermally expanded graphite [11], as a precursor to graphene-based materials is carried out, and important results are published. The present state of knowledge of graphene-based materials/graphite nanoparticles, including preparation of polymer composites has been overviewed, *e.g*., by Kim *et al*. [12], and Potts *et al*. [13].

In the present work, we proceed from the above experiences for graphite powder exfoliation, and adapt and modify them towards GNP exfoliation. We refine GNP material using solvent dispersion, where a small amount of polymer is added to the solvating medium. Direct-GNP microagglomerates are refined, nanoplatelets are exfoliated and polymer is deposited on graphene. The refined filler can easily be turned into a composite either by evaporating the solvent and using it as a masterbach, or polymer could be added to the solution before solvent evaporation in order to tailor the filler content. To the best of our knowledge, there is no report on the use of polymer coated direct-graphite refining.

2. Experimental

2.1. Solvent dispersion

Our early unsuccessful trials included the use of toluene (after bath sonicating for 4 h, the entire mass of GNP material rapidly settled out). Then N-methyl-2-pyrrolidone (NMP) was used, and the following preparation was carried out.

GNP, xGnP from XG Sciences, USA, was mixed together with polyethylene glycol p-(1,1,3,3-tetramethylbutyl)-phenyl ether surfactant, Triton X-100 from Alfa Aesar, Germany, and NMP, in proportion 10:1:200 by weight (nanoplatelets:surfactant: solvent). The mixture was stirred for 15 minutes, and then sonicated in a cuvette in a bath for 2 hours (Branson 1510E-MTH, Branson Ultrasonic Corp., USA). The temperature in the bath did not exceed 55°C during the sonication.

We decided to increase the solvent viscosity by adding polystyrene (PS) (Polystyrol 143 E, BASF, Germany), which was first dissolved in NMP, in proportion 1:15 by weight. The PS-solution was then added to the GNP mixture, stirred for 30 minutes followed by additional sonication for 2 hours. The final concentration of GNP in the solution was

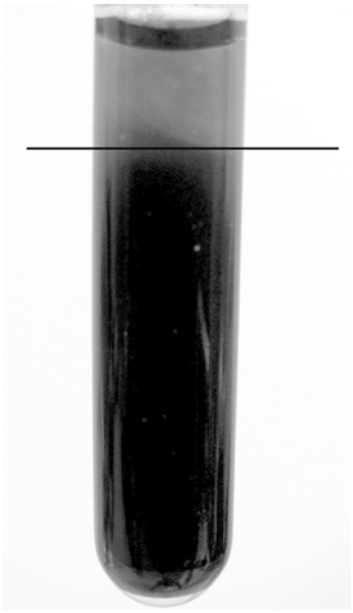

Figure 1. Stable dispersion of thin graphene stacks in NMP/PS (after sonication time of 4 h, and sedimentation time of 170 h)

5 wt% with respect to PS. Cavitations caused by sonication lead to initial intercalation and in turn facilitate solvent penetration into nanoplatelet. Increased solvent viscosity (by the presence of polymer) creates larger forces hindering reverse of intercalation. After 4 h of sonication, the dispersion in the cuvette appeared dark/black. After sedimentation time of close to 170 h, sediment settled out, and a dispersion appearing gray/tinted formed in the upper part of the cuvette (Figure 1), with a thin black layer floating on the surface. Using a microsyringe, a subset of the dispersion was carefully removed, avoiding the floating layer and the sediment.

2.2. Thermal gravimetric analysis

The subset was next analysed using Thermal Gravimetric Analysis (TGA) (TGA/DSC 1 Star system, Mettler Toldedo, Switzerland). The folowing program was used during the analysis, heating from 50–600ºC at a rate of 20ºC/min under nitrogen atmospere, followed by a 40 min isothermal step at 600ºC under air atmospere, and then heating to 900ºC at 20ºC/min under air atomospere. Star software v9.20 was used.

2.3. Transmission Electron Microscopy

The dispersion was further diluted 10 times in (NMP), and a small amount was deposited onto holey carbon grids (400 mesh), and then studied by

Transmission Electron Microscopy (TEM). Images and electron diffraction were taken with an electron transmission microscope (Zeiss EM912 Omega, Germany) equipped with an Ω energy filter and operated at 120 keV.

3. Results and discussion

3.1. TGA

In Figure 2, a representative measured TGA plot is shown. A pronounced weight loss starting at about 400ºC originating from the degradation of the PS is clearly present. By applying oxygen containing atmosphere the reaming GNP was burnt off, and the GNP content was measured to be 0.13 wt% of that of the PS. This corresponds to a GNP concentration in the solution of 0.08 mg/ml, which is comparable to the results obtained by Khan *et al*. [4] at similar sonication time.

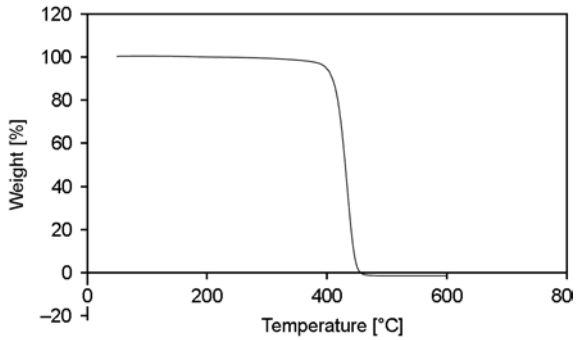

Figure 2. TGA plot of GNP/PS composite

3.2. TEM image analysis

Image analysis was carried out on 23 images. An example is shown in Figure 3.

As can be seen in Figure 3, distinguishable layers (shown with thin arrows) form a stack. Layers grayscale and boundary/edges made it possible to count the layers per stack, as proposed in [4]. Herein, PS molecules deposited on graphene facilitates image analysis, for example edges become more marked and contrasting. On the other hand, the deposited polymer disturbs imaging because of the extra background. Presence of polymer can be noticed on the holey carbon substrate; particularly the smallest hole is filled. Clearly, the layers do not overlap ideally, and the number of layers varies depending on location. In Figure 3, the maximum number of layers is 3. In Figure 4 (histogram), statistics summarizing the 23 images is given. We report

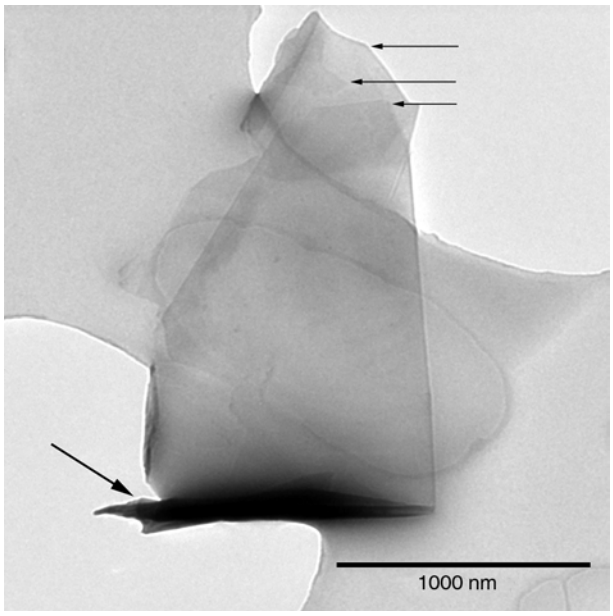

Figure 3. TEM image of a multilayer graphene stack. Thin arrows indicate the edges of the individual layers, and the bold arrow indicates a folded off-plane fragment of layer.

the maximum number of layers per stack. 5 layers is found to be the cut-off number. No stacks >5 layers were found, and 3 layer stacks are dominantly present. This is close to the statistics given in [4], using the edge-counting method proposed by the authors, for the case of exfoliating powdered graphite.

When computing the layers, occasionally, we needed to account for folded graphene. A folded off-plane fragment of layer is seen in Figure 3 (bold arrow). In such a case, two layers were counted. Also in Figure 3, a black grayscale domain can be seen. We believe this can be ascribed to carbon wrap containing polymer and surfactant molecules. In-plane dimensions of layers/stacks are reduced compared to that of pristine GNP, as specified by the supplier. The average largest in-plane dimension is found to

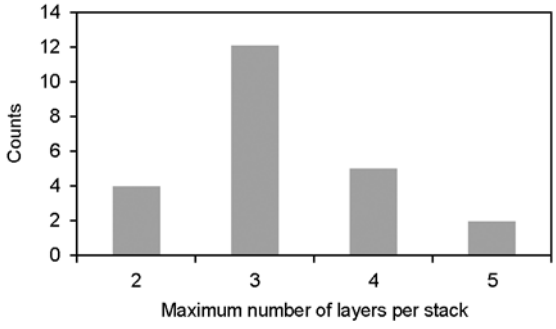

Figure 4. Histogram showing the maximum number of layers whithin a stack

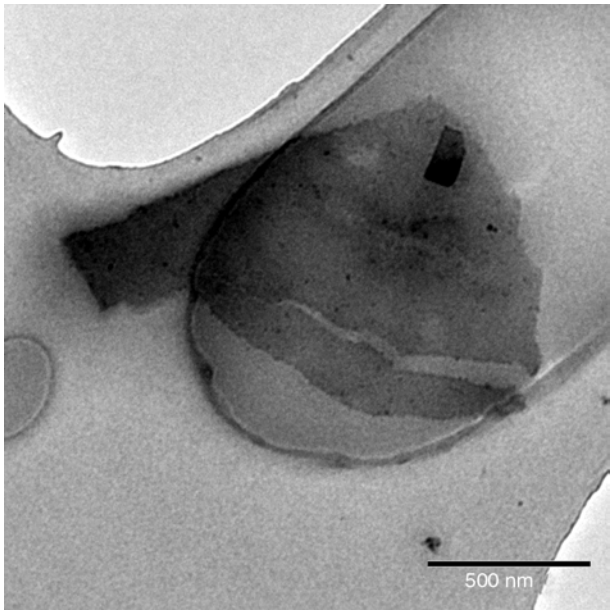

Figure 5. TEM image showing a layer containing a crack

be approximately 2.5 μm. We ascribe this to the sonication process. A layer containing a crack, most likely developed during sonication, is seen in Figure 5. We note that on one occasion, one very large microagglomerate was observed.

3.3. Diffraction analysis

Electron diffraction was carried out as a complementary method, in addition to the image analysis described above. SAD and nano diffraction under Köhler illumination were performed using a small selected area aperture and condenser aperture with diameter of 5 μm.

The PS deposition requires caution when studying the graphene architecture; on the one hand the extra background, and on the other hand the additional irregular edges from PS presence, make subtle differences in identifying graphene edges. According to the numerical simulation with Fourier transformation of projected atomic potentials and scattering factors [14], the intensity ratio $I_{(1100)}/I_{(2100)}$ in the electron diffraction pattern of graphite/graphene with ABAB stacking can be used for distinguishing monolayer from multilayer graphene stacks, as follows.

In Figure 6, TEM bright field image (a), and typical diffraction patterns taken from the monolayer region (b) (marked with a white dot), and multilayer region (c) (marked with a black dot) of a graphene stack, are shown. The image was sufficiently defocused in order to enhance the phase contrast of the

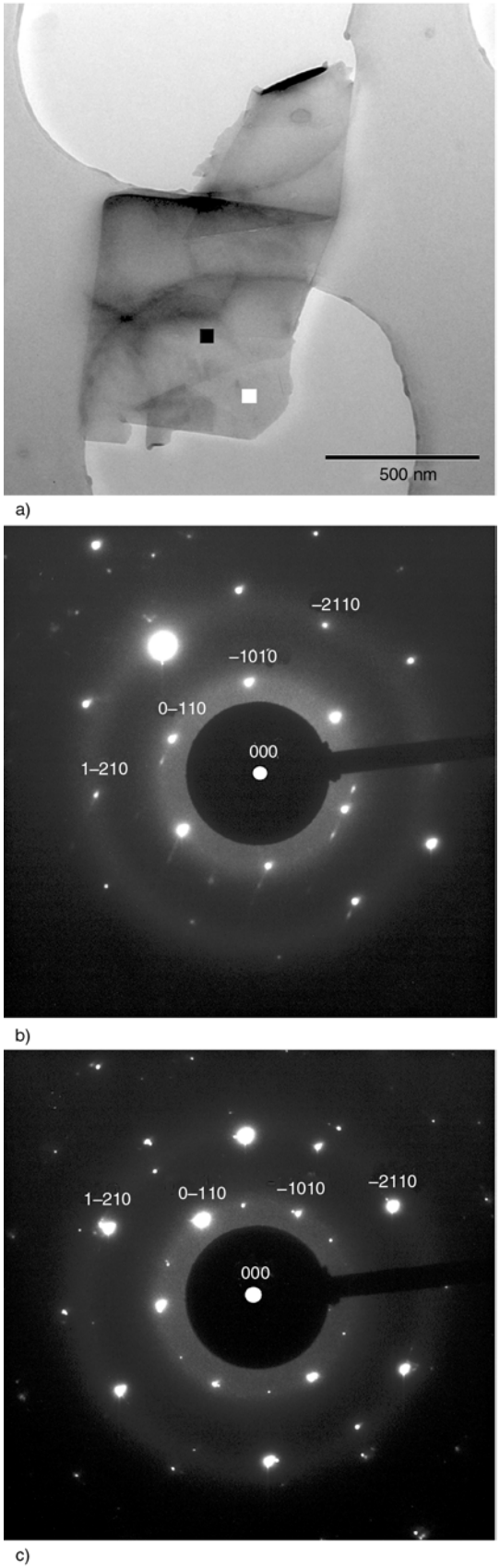

Figure 6. a) TEM bright field image of graphene stack. b) SAD pattern taken from region marked in figure a) with the white dot (monolayer). c) SAD pattern taken from region marked in figure a) with the black dot (multilayer).

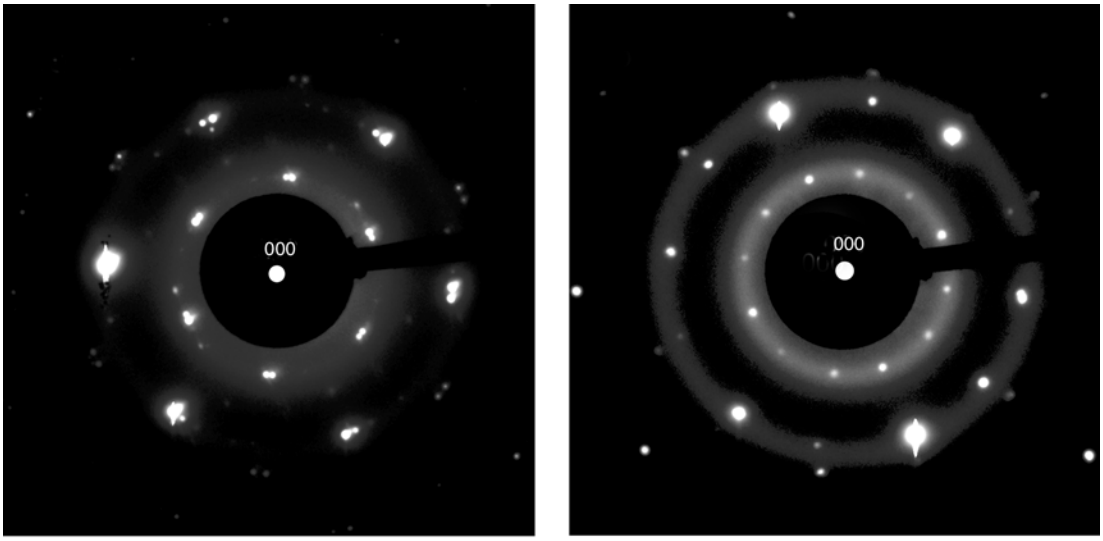

Figure 7. a) SAD pattern of two graphene sheets stacking with a rotation angle of 2.5°. b) SAD pattern of two multilayer graphene superimposed with a rotation angle of 30°.

image. The diffraction patterns exhibit the typical six-fold symmetry, which can be indexed as the [0001] zone pattern of graphite/graphene. As can be seen clearly, the spots intensity ratio $I_{(1100)}/I_{(2100)}$ is >1 in the monolayer pattern (Figure 6b), whereas $I_{(1100)}/I_{(2100)}$ is <1 in the multilayer pattern (Figure 6c). The observation is consistent with the result for pure graphene suspension [15]. The diffraction pattern in Figure 6c can be observed in nearly all the examined multilayer objects. Caution is needed when identifying a monolayer from TEM images. Some monolayer-looking objects may not be monolayer graphene, and have a diffraction pattern of multilayer. Thin graphite sheets or stacked graphene fragments may be mistaken for monolayer graphene particularly when covered with polymer molecules merging the individual edges into one single edge. The presence of monolayer regions and multilayer regions shown with SAD supports the statistical results in Figure 3, and thus we believe that the pristine GNPs have been successfully refined.

Another observation relates to the graphene stack schedule (or build-up), particularly random or non-random assembly. We find that they do not overlap or fold together randomly in the graphene/PS composite. Graphene sheets usually form stacks with either a very small rotation angle (<5°) or close to 30°. Figure 7a presents a SAD pattern of graphene sheets stacking with a rotation angle of 2.5°. Figure 7b shows two sets of [0001] zone patters superimposed of two multilayer graphene with a rotation angle of 30°. The latter rotation relationship can be often observed directly from folded edge of graphene sheets in images (Figure 6a and 6c). The stacking arrangements of the graphene sheets observed in this work are comparable to the zigzag and arm-chair chiralities in carbon nanotubes [16]. While the graphene stacks long range assembly is driven by the surface energy, we believe that when they meet, likely, the thin PS film remaining between the graphene sheets enables more mobility. As a result, the graphene sheets can rotate or orientate themselves towards favourable configurations, at lower energy states.

4. Conclusions

A simple method to exfoliate/refine direct-graphite nanoplatelets towards their better incorporation into a polymeric matrix is presented, and demonstrated for the case of polystyrene. By adding a small amount of polystyrene to N-methyl-2-pyrrolidone solvent containing surfactant, the solvent viscosity increased, and thus created larger forces during sonication and hindered the reverse of intercalation. The refined nanoplatelets were characterized by using Transmission Electron Microscopy based imaging and diffraction analysis. Using the edge-counting method, no platelets thicker than 5 layers, and dominantly 3-layer thick stacks were observed. The average layer's in-plane dimension was 2.5 μm.

The presence of monolayer and multilayer regions, analysed with the selected area diffraction method supports the results.

Acknowledgements

Erik Nilsson at Swerea IVF is acknowledged for TGA measurements. The financial support from the Swedish Foundation for Strategic Research (SSF) is acknowledged.

References

[1] Green A. A., Hersam M. C.: Solution phase production of graphene with controlled thickness via density differentiation. Nano Letters, **9**, 4031–4036 (2009). DOI: 10.1021/nl902200b

[2] Green A. A., Hersam M. C.: Emerging methods for producing monodisperse graphene dispersions. Journal of Physical Chemistry Letters, **1**, 544–549 (2010). DOI: 10.1021/jz900235f

[3] Sun X., Luo D., Liu J., Evans D. G.: Monodisperse chemically modified graphene obtained by density gradient ultracentrifugal rate separation. ACS Nano, **4**, 3381–3389 (2010). DOI: 10.1021/nn1000386

[4] Khan U., O'Neill A., Lotya M., De S., Coleman J. N.: High-concentration solvent exfoliation of graphene. Small, **6**, 864–871 (2010). DOI: 10.1002/smll.200902066

[5] Hernandez Y., Nicolosi V., Lotya M., Blighe F. M., Sun Z., De S., McGovern I. T., Holland B., Byrne M., Gun'Ko Y. K., Boland J. J., Niraj P., Duesberg G., Krishnamurthy S., Goodhue R., Hutchison J., Scardaci V., Ferrari A. C., Coleman J. N.: High-yield production of graphene by liquid-phase exfoliation of graphite. Nature Nanotechnology, **3**, 563–568 (2008). DOI: 10.1038/nnano.2008.215

[6] Bourlinos A. B., Georgakilas V., Zboril R., Steriotis T. A., Stubos A. K.: Liquid-phase exfoliation of graphite towards solubilized graphenes. Small, **5**, 1841–1845 (2009). DOI: 10.1002/smll.200900242

[7] Blake P., Brimicombe P. D., Nair R. R., Booth T. J., Jiang D., Schedin F., Ponomarenko L. A., Morozov S. V., Gleeson H. F., Hill E. W., Geim A. K., Novoselov K. S.: Graphene-based liquid crystal device. Nano Letters, **8**, 1704–1708 (2008). DOI: 10.1021/nl080649i

[8] Lee S. H., Dreyer D. R., An J., Velamakanni A., Piner R. D., Park S., Zhu Y., Kim S. O., Bielawski C. W., Ruoff R. S.: Polymer brushes via controlled, surface-initiated atom transfer radical polymerization (ATRP) from graphene oxide. Macromolecular Rapid Communications, **31**, 281–288 (2010). DOI: 10.1002/marc.200900641

[9] Dreyer D. R., Park S., Bielawski C. W., Ruoff R. S.: The chemistry of graphene oxide. Chemical Society Reviews, **39**, 228–240 (2010). DOI: 10.1039/B917103G

[10] Stankovich S., Dikin D. A., Dommett G. H. B., Kohlhaas K. M., Zimney E. J., Stach E. A., Piner R. D., Nguyen S. T., Ruoff R. S.: Graphene-based composite materials. Nature, **442**, 282–286 (2006). DOI: 10.1038/nature04969

[11] Ansari S., Giannelis E. P.: Functionalized graphene sheet–Poly(vinylidene fluoride) conductive nanocomposites. Journal of Polymer Science Part B: Polymer Physics, **47**, 888–897 (2009). DOI: 10.1002/polb.21695

[12] Kim H., Abdala A. A., Macosko C. W.: Graphene/polymer nanocomposites. Macromolecules, **43**, 6515–6530 (2010). DOI: 10.1021/ma100572e

[13] Potts J. R., Dreyer D. R., Bielawski C. W., Ruoff R. S.: Graphene-based polymer nanocomposites. Polymer, **52**, 5–25 (2011). DOI: 10.1016/j.polymer.2010.11.042

[14] Meyer J. C., Geim A. K., Katsnelson M. I., Novoselov K. S., Booth T. J., Roth S.: The structure of suspended graphene sheets. Nature, **446**, 60–63 (2007). DOI: 10.1038/nature05545

[15] Meyer J. C., Geim A. K., Katsnelson M. I., Novoselov K. S., Obergfell D., Roth S., Girit C., Zettl A.: On the roughness of single- and bi-layer graphene membranes. Solid State Communications, **143**, 101–109 (2007). DOI: 10.1016/j.ssc.2007.02.047

[16] Gao G., Çağin T., Goddard W. A. III.: Energetics, structure, mechanical and vibrational properties of single-walled carbon nanotubes. Nanotechnology, **9**, 184–191 (1998). DOI: 10.1088/0957-4484/9/3/007

eXPRESS Polymer Letters Vol.6, No.2 (2012) 148–158
Available online at www.expresspolymlett.com
DOI: 10.3144/expresspolymlett.2012.16

Crystallization and melting behavior of nanoclay-containing polypropylene/poly(trimethylene terephthalate) blends

S. H. Jafari[1], A. Kalati-vahid[1], H. A. Khonakdar[2], A. Asadinezhad[3], U. Wagenknecht[4], D. Jehnichen[4]*

[1]Department of Polymer, School of Chemical Engineering, College of Engineering, University of Tehran, P.O.Box: 11365-4563, Tehran, Iran
[2]Iran Polymer and Petrochemical Institute, P.O.Box:14965-115, Tehran, Iran
[3]Department of Chemical Engineering, Isfahan University of Technology, P.O.Box: 84156-83111, Isfahan, Iran
[4]Leibniz Institute of Polymer Research Dresden, Hohe Str. 6, D-01069, Dresden, Germany

Received 4 May 2011; accepted in revised form 14 September 2011

Abstract. This contribution concerns preparation and characterization of polypropylene (PP)/poly(trimethylene terephthalate) (PTT) melt-mixed blends in the presence of organically-modified montmorillonite nanoclays and functional compatibilizers. Immiscibility and nanocomposite formation were confirmed via transmission electron microscopy. An intercalated structure was observed by wide angle X-ray diffraction technique. Crystallization, and melting characteristics were studied by differential scanning calorimetry in both isothermal and non-isothermal modes, supplemented by temperature modulated DSC (TMDSC). A concurrent crystallization was found for both polymeric components in the blends. Whereas blending favored PP crystallizability, it interrupted that of PTT. The addition compatibilizers interfered with rate, temperature, and degree of crystallization of PP and PTT. On the contrary, nanoclays incorporation increased crystallizability of each individual component. However, as for blend nanocomposite samples, the way the crystallization behavior changed was established to depend on the type of nanoclay. Based on kinetic analysis, isothermal crystallization nucleation followed athermal mechanism, while that of non-isothermal obeyed thermal mode. Addition of nanoclays shifted nucleation mechanism from athermal to thermal mode.

Keywords: *nanocomposites, polymer blends, crystallization, polypropylene, poly(trimethylene terephthalate)*

1. Introduction

The extensive use of polypropylene (PP) in a broad spectrum of applications has fueled a huge interest in conducting research meant for improvement of this common polymer. Aromatic polyesters, thanks to overall superior properties, have found a niche as candidates to foster PP performance via blending and nanocomposite technologies [1, 2]. A major challenge on the way forward is inherent incompatibility of polyester and polyolefin [3, 4]. This has been dealt with to much extent by incorporating compatibilizers such as, maleic anhydride-grafted PP (PP-g-MAH) [5, 6], ethylene-butyl acrylate-glycidyl methacrylate terpolymer (Elvaloy PTW) [7, 8], and ethylene-glycidyl methacrylate (E-GMA) copolymers [9, 10]. An alternative, up-to-date approach is to harness clay-based nanofillers [11–17] as well as inorganic nanoscale particles [18] frequently used in polymeric systems originally intended for improving compatibility as well as mechanical properties.
An intricate subject in the realm of polymer blends and nanocomposites is crystallization and melting behaviors on which the final properties strongly rely [19, 20]. The complications indeed, come from

*Corresponding author, e-mail: shjafari@ut.ac.ir

the critical interactions among the blend components and how the crystallization characteristics are accordingly altered [21]. Poly(trimethylene terephthalate) (PTT), a relatively new member of aromatic polyesters, has been established to possess a combination of properties of two analogous predecessors, poly(ethylene terephthalate) (PET) and poly(butylene terephthalate) (PBT) [22]. Few publications in the literature focus on the thermal properties of PP/PTT blends and nanocomposites which communicate rather contradictory findings in some aspects [23–26]. Xue *et al*. [23] in a detailed study reported that PTT and PP crystallization rates are expedited by the presence of each other and the acceleration is dependent on the blend ratio. Also PTT showed a fractionated crystallization. PP-g-MAH as a reactive compatibilizer decreased the crystallization temperature of PTT and PP which was more significant for PTT due to the reactivity of maleic anhydride and PTT. It took a longer time to reach a given crystallinity for compatibilized blends compared to the corresponding uncompatibilized ones. Elsewhere, Lin and Cheng [24] in an article on PTT/PP blends reported a complex melting behavior accounted for by recrystallization process. They stated that PP in PTT/PP blends can increase the crystallization rate of PTT and reduce the amount of imperfect PTT crystals. Furthermore, the crystalline structure of PTT in blends remained intact. Wang and Run [25] reported that PTT/PP blends exhibit different crystallization and melting behavior depending on PP-g-MAH content. The results showed that the crystallization rate of PTT component is raised on introduction of PP-g-MAH, even though that of PP component is slowed down. As to PTT/PP nanocomposites with and without PP-g-MAH, Upadhyay *et al*. [26] recently carried out various measurements and observed an intercalated morphology as well as an increase in crystallization temperature of the blend components in presence of nanoclays, however, crystallinity and melting temperature of the components were not affected significantly.

With particular attention to the existing complexities of and rising demands for nano-based multiphase polymer systems, the idea behind the current effort is to shed light on crystallization and melting characteristics of PP/PTT blends in presence of organically modified montmorillonite (Cloisite nanoclays 20A and 30B), Elvaloy PTW, and PP-g-MAH via differential scanning calorimetry (DSC), temperature-modulated DSC (TMDSC), wide-angle X-ray diffraction (WAXS), and transmission electron microscopy (TEM). Cloisite 20A and 30B have been selected on account of their characteristic difference as the former was reported to be considerably more hydrophobic than the latter [27].

2. Experimental

2.1. Materials

All of the materials used in this work were of commercial grade consumed as received without further treatment. Isotactic PP (Moplen HP501H) with melt flow rate of 2.1 g/10 min was purchased from Basell Company (Germany). PTT (RTP 4700), with an intrinsic viscosity of 0.901 ml/g, measured at 25°C in a 60/40 mixture of phenol and tetrachloroethane, was obtained from RTP Company (USA). Elvaloy PTW, containing 2.4 wt% GMA, was obtained from DuPont (USA). PP-g-MA (Polybond 3200) was supplied by Chemtura (USA). Cloisite 20A and Cloisite 30B were provided from Southern Clay Products (USA).

2.2. Samples preparation

The processing conditions were set based on this fact that it strongly affects nanoclay dispersion [28]. The samples were prepared in an intermeshing twin screw extruder (Berstorff) using a temperature profile of 200–235°C at screw speed of 200 rpm in co-rotating mode. The extrudate was collected in the form of rods in absence of drawing in order not to

Table 1. Compositions and codes of the samples

Sample code	PP/PTT ratio	Compatibilizer [wt%]	Nanoclay [wt%]
PP100	100/0	0	0
PP97CA3	100/0	0	3 Cloisite 20A
PP95CA5	100/0	0	5 Cloisite 20A
PTT100	0/100	0	0
PTT95CB5	0/100	0	5 Cloisite 30B
B100	75/25	0	0
B95E5	75/25	5 Elvaloy PTW	0
B95gM5	75/25	5 PP-g-MAH	0
B90E10	75/25	10 Elvaloy PTW	0
N95CB5	75/25	0	5 Cloisite 30B
N95CB2.5CA2.5	75/25	0	2.5 Cloisite 20A + 2.5 Cloisite 30B
N90E5CB5	75/25	5 Elvaloy PTW	5 Cloisite 30B
N85E10CB5	75/25	10 Elvaloy PTW	5 Cloisite 30B

assume orientation. A constant PP/PTT weight ratio, 75/25, was used with various contents of the compatibilizers and nanoclays. All of the components were introduced to the extruder in a single step. The formulation of the samples is presented in Table 1.

2.3. Characterization

2.3.1. WAXS

Wide angle X-ray diffraction (WAXS) analysis was performed on X-ray diffractometer P4 with area detection system GADDS (Bruker, Germany), operating at 40 kV and 30 mA using Cu K_α radiation (λ = 0.154 nm). The samples were investigated in transmission with primary beam normal to extrusion direction. The scanning was carried out in 2θ range between 1.8 and 40.5°.

2.3.2. DSC

Thermal behavior was examined on Q2000 DSC (TA Instruments USA), with samples of about 5 mg sealed in aluminum pans under nitrogen atmosphere. The samples were first heated from 25 to 250°C at 10°C/min, kept at 250°C for 2 min to erase the thermal history. To study non-isothermal behavior, cooling was executed down to 25°C at the rate of 10°C/min. The samples were finally heated back to 250°C at the same rate to study the subsequent melting behavior. Isothermal crystallization was performed stepwise at different sets of temperatures to determine the optimal one where the highest crystallization rate for each component was reached. The samples were accordingly cooled from 250 to 170°C (optimal isothermal crystallization temperature for PTT), held for 10 min to examine PTT component crystallization, and then prompt cooling continued to 120°C (optimal isothermal crystallization temperature for PP), kept for 30 min to examine PP crystallization. Cooling was then performed back to 25°C at the rate of 10°C/min and subsequent melting was done at equal rate to 250°C. Furthermore, crystallization degree was estimated based on the Equation (1):

$$X_c = \frac{\Delta H_m}{\omega_f \cdot \Delta H_m^0} \cdot 100 \quad (1)$$

where ΔH_m is the measured melting enthalpy and ΔH_m^0 is melting enthalpy of 100% crystalline sample. ω_f denotes weight percentage. For neat PTT, ΔH_m^0 = 145.5 J/g [22] and for neat PP, ΔH_m^0 =207.0 J/g [29].

2.3.3. TMDSC

TMDSC (Mettler Toledo DSC, Switzerland) was managed to investigate the complex melting phenomena on 6 mg samples sealed in aluminum pans. The specimen was heated from 25 to 250°C at 10°C/min and kept 2 min at 250°C, subsequently cooled down to 25°C at the rate of 10°C/min and heated to 100 C. The final heating was carried out from 100 to 240°C to observe cold crystallization at amplitude of 1° and period of 60 sec.

2.3.4. TEM

The extruded samples were ultramicrotomed down to 80 nm thickness under cryogenic conditions at –120°C via EM UC/FC6 ultramicrotome (Leica, Germany) equipped with a diamond knife. TEM images were then recorded using LEO 910 TEM (Carl Zeiss, Germany) at an acceleration voltage of 120 kV.

3. Results and discussion

3.1. Morphology

TEM morphological images of three representative samples are given in Figure 1. As it is evident from Figure 1a, which corresponds to sample N95CB5, PTT droplets are dispersed within PP matrix. Exfoliated Cloisite 30B nanoparticles are distributed in PTT phase as well as blend interphase confirming nanocomposite formation. The higher tendency of Cloisite 30B to PTT has also been reported elsewhere [26] which is principally due to their hydrophilic affinity. On introduction of 2.5 wt% Cloisite 20A and 2.5 wt% Cloisite 30B to PP/PTT blend (Figure 1b), nanoclay content at the interphase rises significantly to the detriment of that inside PTT droplets which reveals the tendency of Cloisite 20A to reside at the interfacial phase because of its hydrophobic nature. Depending on the material, Cloisite 20A locates selectively in the phase with which it has more affinity [30]. The selective localization of nanoclay is also predictable from surface free energy values (pertinent data not shown). Furthermore, the presence of Cloisite 20A led to an increase in PTT droplets size and aspect ratio seemingly on account of coalescence. According to Figure 1c, addition of the compatibilizer, Elvaloy PTW, as much as 5 wt% to N95CB5 gives rise to significant alterations in morphology, *viz*., an increased PTT dispersion due to reduced interfacial tension

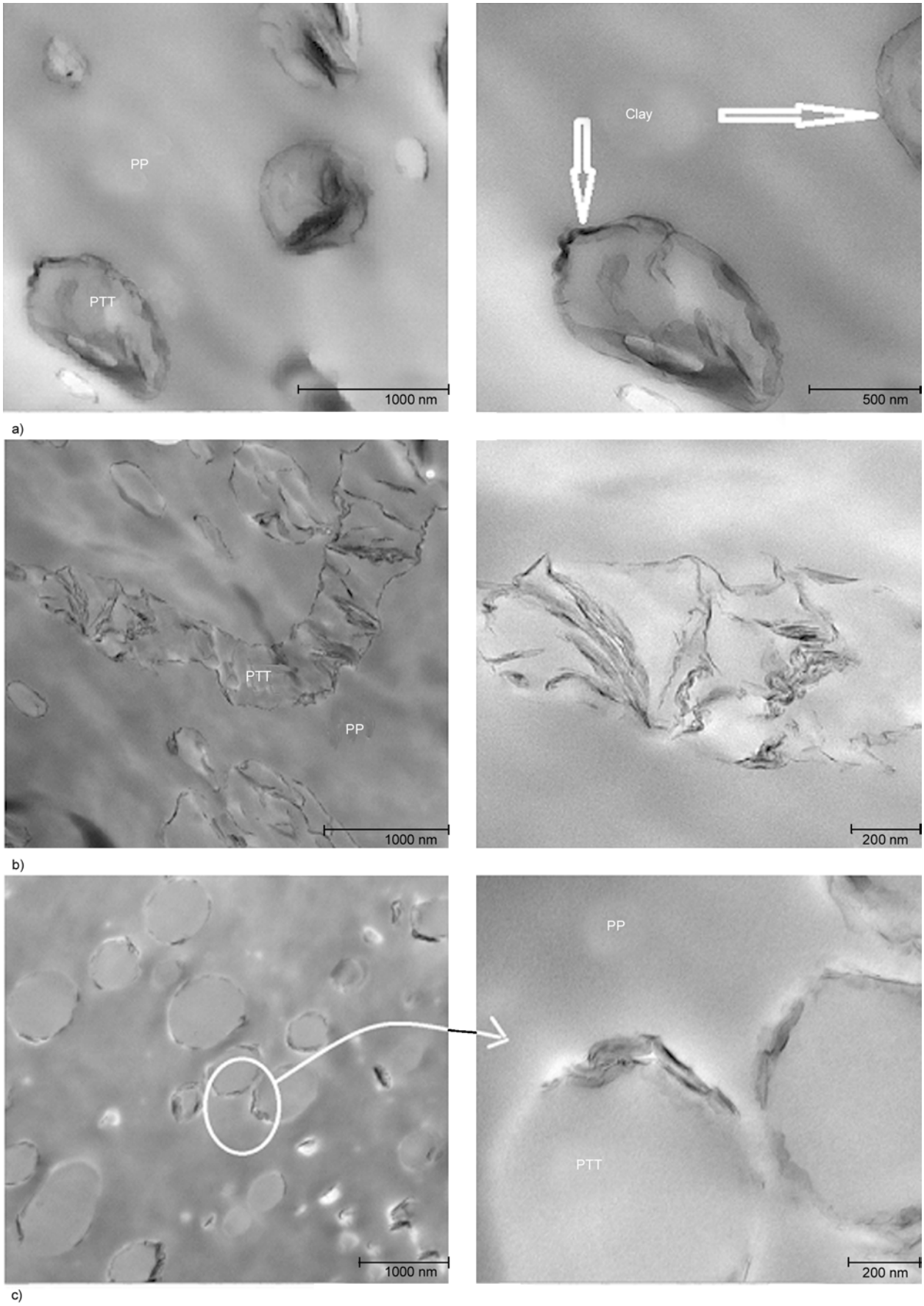

Figure 1. TEM morphological images of different samples: (a) N95CB5, (b) N95CB2.5CA2.5, (c) N90E5CB5

and coalescence, an enlarged gallery space of clay layers, and a higher amount of nanoclays lying at the interphase rather than within PTT phase domain. The significant difference compared to N95CB5 sample refers to the formation of a compatibilizer-rich phase which encompasses a considerable amount of nanoclay due to their affinity. This leads to a reduction of nanoclay presence at the interphase as well as inside PP droplets.

3.2. X-ray crystallography

The WAXS patterns from different samples along with pure nanoclays are presented in Figure 2. Over low-scattering-angle range (Figure 2a), the observed peaks in the given patterns correspond to (001) crystalline plane of nanoclays preserved when compounded with polymeric constituents. This is indicative of an intercalated morphology formation being in agreement with Upadhyay *et al*. [26]. Nanoclays interlayer distance values estimated based on Bragg's law [21] are also embedded in the graph. Data suggests weak interactions between PP chains and Cloisite 20A galleries since the interlayer distance remains nearly unchanged upon blending with PP, while an opposite trend is seen between PTT and Cloisite 30B moieties corroborating the TEM findings. Furthermore, the presence of Cloisite 30B contributes to intercalation by raising the gallery spacing in blend nanocomposite samples implying the facilitated insertion of polymer chains within the interlayer space in virtue of polymer-nanoclay affinity [31].

Based on the patterns shown in Figure 2b, PP α-crystalline form is discernible by the signals assigned to (110), (040), (130), (111), (131), and (041) planes. Neat PTT samples gives no characteristic peaks remaining amorphous under imposed processing conditions. Introduction of the compatibilizer and nanoclays into PP/PTT blends has no sensible effect on PP crystalline size similar to what is reported by Lin and Cheng [24]. This is learned from the data calculated for (040) crystal plane in accordance with the Scherrer equation [32] and demonstrated graphically in Figure 3a.

According to the Scherrer equation, the crystal size (L) is given by Equation (2):

$$L = \frac{0.9 \cdot \lambda}{\beta \cdot \cos\theta} \tag{2}$$

where λ denotes wavelength, θ is scattring angle, and β is full width at half maximum. Also, the repsective crystalline percentage (X) is calculated from Equation (3):

$$X_{040} = \frac{S_{040}}{S_{040} + S_{110} + S_{130} + S_{111} + S_{041}} \tag{3}$$

In which S refers to area under each scattering peak. Nonetheless, an overall advantageous impact of blending as well as nanoclays incorporation on crystallinity values is found (Figure 3a) obtained based on Zipper equation [33] which may be attributed to the nucleating effects and dispersed phase domain size. Zipper equation gives orientation parameters of (040) crystal plane, A_{110} (Equation (4)), and (110) crystal plane, C (Equation (5)), in terms of signals intensity values (I):

$$A_{110} = \frac{I_{110}}{I_{110} + I_{111} + I_{\underline{\quad}_{131+041}}} \tag{4}$$

$$C = \frac{I_{040}}{I_{110} + I_{040} + I_{130}} \tag{5}$$

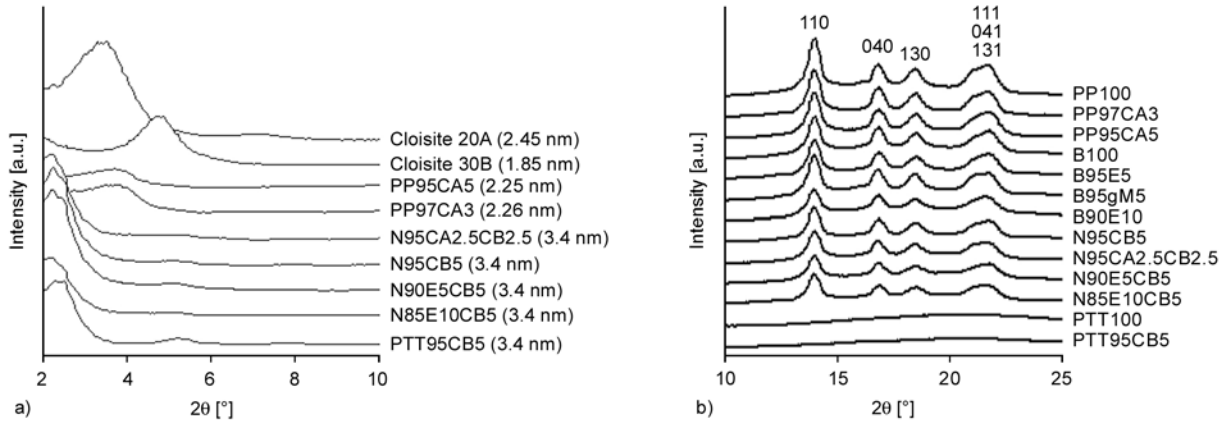

Figure 2. WAXS patterns of different samples: (a) low scattering angle range (b) medium scattering angle range

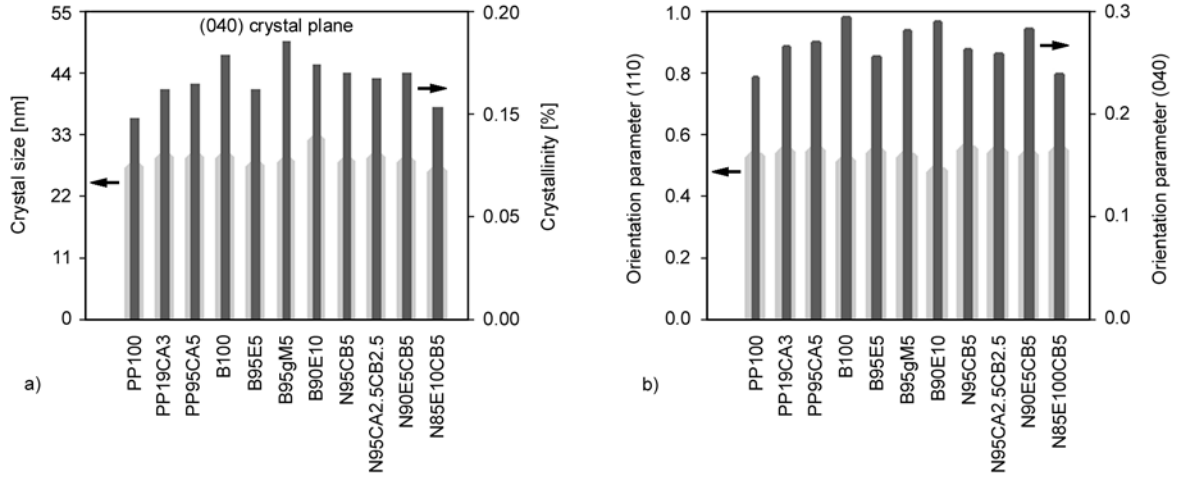

Figure 3. Crystallographic parameters estimated for different samples: (a) crystalline size and percentage, (b) orientation indices of crystal planes

A_{110} and C indices are presented in Figure 3b. It is deduced such that under processing conditions maintained for samples preparation, orientation index of (110) direction is not influenced while that of (040) is favored by blending and nanocomposite formation.

3.3. Crystallization and melting

DSC thermograms of the samples undergone the isothermal crystallization process together with the corresponding heating scan are given in Figure 4 and 5, respectively. A complex melting behavior is observed for neat PP (PP100) arising from melting of crystals with different thermal stability [34]. Moreover, a cold crystallization phenomenon for pure PTT (PTT100) is noticed stemmed from chains reorganization [35]. Both phenomena vanish in heating scan of PP/PTT blend sample (B100), which shows a single crystallization peak in very close proximity to PP exothermic signal. A cursory examination of Figure 4 curves may suggest that PTT remains amorphous, although based on Figure 5, two distinct melting peaks emerge for B100 implying the crystallization of both components. The melting endotherm due to PTT is raised either as a result of melt or cold crystallization. The occurrence of the latter is excluded after a survey into the obtained TMDSC thermograms (Figure 6). Since both reversing and non-reversing heat flow curves possess resembling endotherms, it is understood that no thermally-induced crystallization associated with PTT chains reorganization happens. Therefore, PTT and PP crystallize under cooling simultaneously giving rise to a concurrent crystallization which normally occurs when the crystallization temperature ranges coincide provided the crystallizability of the blend components is similar [3]. To get further insight into the isothermal crystallization and melting behav-

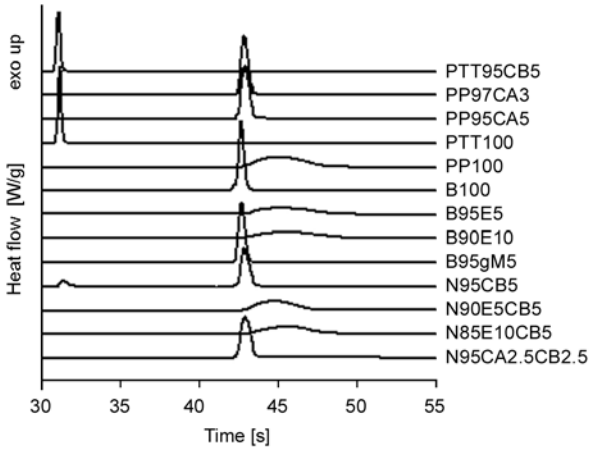

Figure 4. DSC cooling thermograms of the samples crystallized isothermally at certain temperatures

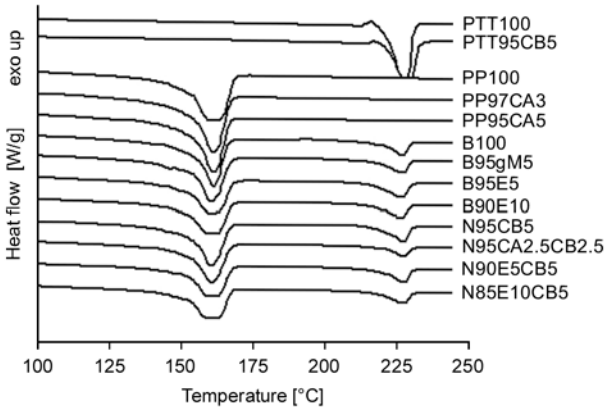

Figure 5. DSC melting thermograms of the isothermally-crystallized samples

Table 2. Isothermal crystallization and the respective melting data of the samples

Sample	PP component				PTT component			
	ΔH_c[(1)] [J/g]	T_m[(2)] [°C]	ΔH_m[(3)] [J/g]	X[(4)] [%]	ΔH_c [J/g]	T_m [°C]	ΔH_m [J/g]	X [%]
PP100	84.0	161.0	84.0	40.5	…	…	…	…
PP97CA3	85.8	161.3	85.8	42.7	…	…	…	…
PP95CA5	85.0	160.8	85.0	43.2	…	…	…	…
PTT100	…	…	…	…	50.7	227.5	50.7	35.1
PTT95CB5	…	…	…	…	49.5	228.6	49.5	34.7
B100	77.0	161.0	65.0	41.9	…	227.3	12.0	33.0
B95gM5	76.2	160.8	66.0	44.7	…	227.0	10.5	30.4
B95E5	58.0	160.5	47.5	32.2	…	226.9	10.1	28.9
B90E10	56.0	160.3	46.0	32.9	…	227.5	10.0	30.5
N95CB5	65.1	161.0	62.0	42.0	8.9	227.7	12.0	34.7
N95CB2.5CA2.5	64.5	161.8	58.5	39.6	…	227.9	6.0	17.3
N90E5CB5	54.8	159.8	45.5	32.2	…	228.0	9.5	29.6
N85E10CB5	53.9	160.1	44.0	33.5	…	228.4	10.0	30.7

(1)Crystallization enthalpy
(2)Melting temperature
(3)Melting enthalpy
(4)Crystallinity

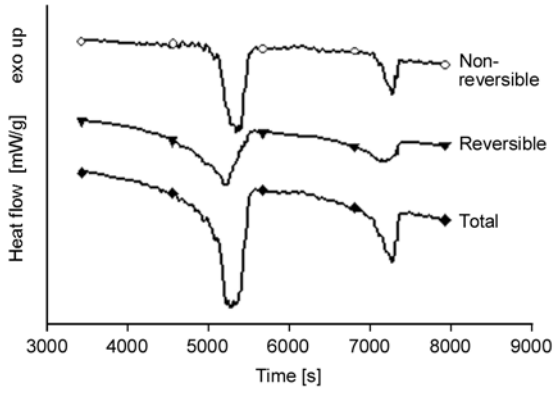

Figure 6. TMDSC curves of B100 sample obtained during heating scan

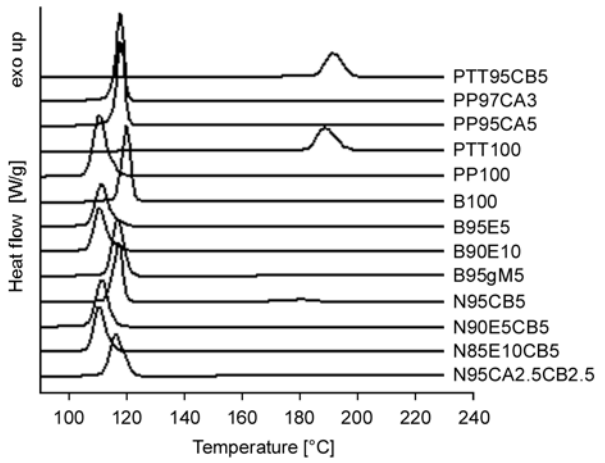

Figure 7. DSC cooling thermograms of the samples crystallized non-isothermally

ior, Table 2 is given embracing numerical data. It is inferred that blending leads to a decrease in crystallization rate and degree of PTT component while the opposite is found for PP. This can be explained based on the favorable role of PTT crystallites for PP nucleation stage, while PTT crystallization is hindered by PP phase being in molten state when PTT is about to crystallize. Similar conclusion has also been reported on PET nucleating role on PP crystallization in PP/PET blend [36].

Non-isothermal crystallization and melting behavior of the samples are respectively demonstrated in Figures 7 and 8. The cold crystallization of PTT100 again appears, while the complex melting of PP100 disappears. Blending PTT with PP correspondingly results in a decrease in PTT crystallization temperature and an increase in that of PP, as numerically displayed in Table 3. Heating scan of the non-

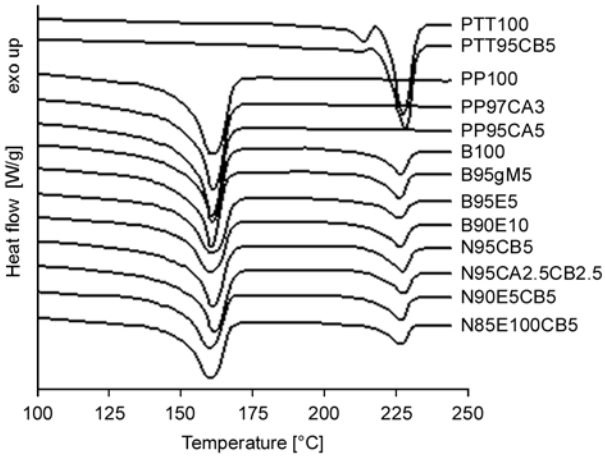

Figure 8. DSC melting thermograms of the non-isothermally-crystallized samples

isothermally crystallized blend (B100) reveals neither complex melting behavior nor recrystallization

Table 3. Non-isothermal crystallization and the respective melting data of the samples

Sample	PP component				PTT component			
	ΔH_c [J/g]	T_m [°C]	ΔH_m [J/g]	X [%]	ΔH_c [J/g]	T_m [°C]	ΔH_m [J/g]	X [%]
PP100	86.7	160.7	86.7	41.9	…	…	…	…
PP97CA3	90.3	161.0	90.3	45.0	…	…	…	…
PP95CA5	90.5	160.7	90.5	46.0	…	…	…	…
PTT100	…	…	…	…	48.6	227.0	48.1	33.1
PTT95CB5	…	…	…	…	44.3	227.1	44.3	32.0
B100	78.7	160.7	65.9	42.5	…	226.1	12.6	34.6
B95gM5	79.5	160.5	67.0	45.4	…	225.9	12.0	34.7
B95E5	62.0	160.4	49.5	33.5	…	226.0	13.0	37.6
B90E10	61.2	160.2	48.0	34.3	…	225.9	12.8	39.1
N95CB5	68.0	161.0	62.0	42.0	6.6	226.7	12.0	34.7
N95CB2.5CA2.5	66.8	161.6	60.0	40.7	…	226.8	6.2	18.1
N90E5CB5	60.0	159.6	49.0	35.0	…	226.5	10.9	33.3
N85E10CB5	58.0	159.5	46.0	34.8	…	226.7	11.0	35.6

phenomenon. Furthermore, no significant shift in melting peaks are observed on blending.

The addition of the compatibilizers, i.e. Elvaloy PTW and PP-g-MAH, to PP/PTT blend (B95E5, B90E10, B95gM5) entails considerable changes in the respective thermal characteristics, of which a reduction in crystallizability of the blend constituents is brought about, as evident from Table 2 data. This agrees with a similar published attempt [24]. The presence of the compatibilizer entities located at the interface results in a decrease of PTT dispersed phase domains which restricts the crystallization potential of both components. Further increase of Elvaloy PTW quantity (B90E10) has no detectable change on blend crystallization rate and degree possibly due to the interfacial saturation which is elaborated on for different blends in the literature [37]. It is interesting to note that PP-g-MAH influences PP thermal characteristics stronger than Elvaloy PTW, while an inverse trend is evident for PTT surmised to be on account of the structural similarity of the former pair and the higher reactivity of the latter one. Additionally, it is noteworthy that PTT cold crystallization disappears, however, the complex melting behavior of PP is preserved in presence of both compatibilizers revealing the influence of the compatibilizer entities on PP crystal morphology.

As for non-isothermal crystallization and melting, the compatibilizers decrease crystallization temperature of both components in blend. Neither complex melting nor cold crystallization is observed in melting scans after introducing compatibilizers. Also, no significant shifts in melting peaks are observed on compatibilizer addition.

Nanoclay particles affect crystallization characteristics of the polymeric components (PP95CA5, PTT95CB5), where Cloisite 20A acts as nucleating agent and increases crystallization rate and degree of PP. Further addition of clay content has no favorable influence but a slightly negative impact is also observed which is ascribed to an increase in viscosity as well as chain folding energy [38, 39]. Moreover, the complex melting behavior of PP is absent in the presence of nanoclay. As for PTT, Cloisite 30B particles contribute to the crystallization rate, however, crystallization degree slightly decreases. This may be related to the nucleating effect of nanoclays particles within PTT region leading to an increase in overall rate of crystal formation. Cold crystallization of PTT is also retained as evident from the respective melting scan.

Analogous to the above-stated findings, as regards the non-isothermal crystallization and melting thermograms, the introduction of nanoclays to the homopolymers increase crystallization temperature of PP and PTT. The favorable effect of nanoclays on PP crystallization has been addressed by Preschilla *et al*. [40]. Complex melting of PP is absent while cold crystallization is yet detectable for PTT in heating scans. Also, no significant shifts in melting peaks are observed on nanoclays addition.

Concerning the blend nanocomposite samples (N95CB5, N95CB2.5CA2.5, N90E5CB5, N85E10CB5), Cloisite 30B is effective as it increases PP crystallizability, whereas decreases that of PTT.

On addition of Cloisite 20A to the nanocomposite sample, crystallization rate and degree of both PTT and PP are adversely altered. This may be associated with the tendency of Cloisite 20A to reside at the interfacial phase, rather than inside PTT domain which led to an increase in PTT droplets size and undermine the nucleating effect of PTT particles on PP crystallization. It should be noticed that the compatibilizer restricts crystallizability of the nanocomposite sample due to the same reasons stated earlier. This component diminishes the content of nanoclay particles in PTT phase and impairs both crystallization rate and degree. Further addition of the compatibilizer slightly affects crystallization and melting parameters which is believed to be due to the interfacial saturation and micelle formation. In respect of the heating scans, the complex melting behavior of PP is observed in the blend nanocomposite samples, while the cold crystallization of PTT is not.

Concerning non-isothermal mode, PTT crystallization temperature decreases while that of PP increases on introduction of Cloisite 30B to the blend, whereas the addition of cloisite 20A has reducing effect on crystallization temperature of both components. The heating scan of the non-isothermally crystallized blend nanocomposites reveals neither complex melting behavior nor recrystallization phenomenon. Furthermore, no significant shift in melting peaks are discernible being consistent with the literature [26]. An overall comparison among the data on the samples crystallization behavior shows that the compatibilizer is remarkably more influential than nanoclay.

From kinetic standpoint, Avrami equation [41] has been employed whose characteristic parameters, that is to say, *n* and *K* are given in Table 4. *K* denotes the rate constant and *n* is the Avrami exponent which depends on the nucleation and growth mechanisms and is said to have contributions from growth dimensionality and nucleation mode [40]. According to the table, the n values mostly range between 2.2 and 3.6 which indicates athermal nucleation process followed by a two-dimensional (mostly in blend nanocomposites) or three-dimensional crystal growth, respectively. However, nanoclay particles alter the nucleation mode from athermal to thermal signified by a noticeable increase in the Avrami index. To describe the non-isothermal kinetics, Avrami equation was modified by Wang and Run [25] by defining a reduced rate constant on the basis of the cooling rate. Non-isothermal kinetics with respect to n values shows that crystallization occurs via thermal mode through a three-dimensional growth.

Table 4. Kinetic analysis data of the samples based on the Avrami equation

Sample	Isothermal		Non-isothermal	
	n	ln K	n	ln K
PP100	2.3	–5.16	4.5	–19.98
PP97CA3	4.0	–6.91	4.5	–17.52
PP95CA5	5.3	–10.17	4.9	–18.77
B100	9.3	–19.31	10.2	–47.06
B95gM5	3.7	–6.06	4.1	–18.63
B95E5	2.3	–5.17	4.8	–20.06
B90E10	2.3	–5.34	5.8	–27.29
N95CB5	3.4	–5.90	5.1	–20.75
N95CA2.5CB2.5	3.5	–6.14	4.0	–16.53
N90E5CB5	2.2	–4.90	4.7	–20.83
N85E10CB5	2.5	–5.78	4.4	–18.83

4. Conclusions

The results from TEM on characterization of PP/PTT blend nanocomposites show an inherent incompatibility which is resolved to some extent through compatibilizer incorporation. Cloisite 30B exhibits higher inclination to PTT phase rather PP. WAXS reveals an intercalated morphology where the gallery spacing is considerably contributed by Cloisite 30B. Also, introduction of nanoclays and compatibilizers has no detectable impact on PP α-crystalline size. DSC studies indicate a simultaneous crystallization of both polymeric components in blends. Blending favors PP crystallizability, even though it curbs that of PTT. Addition of compatibilizers interferes with crystallizability of PP and PTT. However, nanoclays incorporation increases crystallizability of polymer in samples of polymer/nanoclay. As to blend nanocomposites, the way the crystallization behavior varies relies on type of nanoclay. Based on Avrami kinetic analysis, nucleation stage of isothermal crystallization follows athermal mechanism, while that of non-isothermal obeys thermal mode. Furthermore, addition of nanoclays shifts nucleation mechanism from athermal to thermal mode. A comparison among the data on crystallization and melting characteristics shows that the compatibilizer is remarkably more influential than nanoclay.

Acknowledgements

H.A. Khonakdar thanks Alexander von Humboldt foundation for financial support.

References

[1] Karian H.: Handbook of polypropylene and polypropylene composites. Marcel Dekker, New York (2003). DOI: 10.1201/9780203911808

[2] Karger-Kocis J., Fakirov S.: Nano- and micromechanics of polymer blends and composites. Hanser, Munich (2009).

[3] Utracki L. A.: Polymer blends handbook. Kluwer, Dordrecht (2002).

[4] Karger-Kocsis J.: Polypropylene: Structure, blends and composites: Structure and morphology copolymers and blends composites. Chapman and Hall, London (1995).

[5] Dorscht B. M., Tzoganakis C.: Reactive extrusion of polypropylene with supercritical carbon dioxide: Free radical grafting of maleic anhydride. Journal of Applied Polymer Science, **87**, 1116–1122 (2003). DOI: 10.1002/app.11561

[6] Kaci M., Benhamida A., Cimmino S., Silvestre C., Carfagna C.: Waste and virgin LDPE/PET blends compatibilized with an ethylene-butyl acrylate-glycidyl methacrylate (EBAGMA) terpolymer, 1. Macromolecular Materials and Engineering, **290**, 987–995 (2005). DOI: 10.1002/mame.200500217

[7] Benhamida A., Kaci M., Cimmino S., Silvestre C., Duraccio D.: Melt mixing of ethylene/butyl acrylate/glycidyl methacrylate terpolymers with LDPE and PET. Macromolecular Materials and Engineering, **294**, 122–129 (2009). DOI: 10.1002/mame.200800214

[8] Asadinezhad A., Yavari A., Jafari S. H., Khonakdar H. A., Böhme F.: Description of the dynamic moduli of poly(trimethylene terephthalate)/polyamide-12 blends in molten state. Polymer Engineering and Science, **45**, 1401–1407 (2005). DOI: 10.1002/pen.20413

[9] Loyens W., Groeninckx G.: Rubber toughened semicrystalline PET: Influence of the matrix properties and test temperature. Polymer, **44**, 123–136 (2003). DOI: 10.1016/S0032-3861(02)00743-7

[10] Pawlak A., Morawiec J., Pazzagli F., Pracella M., Galeski A.: Recycling of postconsumer poly(ethylene terephthalate) and high-density polyethylene by compatibilized blending. Journal of Applied Polymer Science, **86**, 1473–1485 (2002). DOI: 10.1002/app.11307

[11] Ray S. S., Bousmina M.: Compatibilization efficiency of organoclay in an immiscible polycarbonate/poly (methyl methacrylate) blend. Macromolecular Rapid Communications, **26**, 450–455 (2005). DOI: 10.1002/marc.200400586

[12] Li Y., Shimizu H.: Novel morphologies of poly(phenylene oxide) (PPO)/polyamide 6 (PA6) blend nanocomposites. Polymer, **45**, 7381–7388 (2004). DOI: 10.1016/j.polymer.2004.09.018

[13] Khatua B. B., Lee D. J., Kim H. Y., Kim J. K.: Effect of organoclay platelets on morphology of nylon-6 and poly(ethylene-*ran*-propylene) rubber blends. Macromolecules, **37**, 2454–2459 (2004). DOI: 10.1021/ma0352072

[14] Si M., Araki T., Ade H., Kilcoyne A. L. D., Fisher R., Sokolov J. C., Rafailovich M. H.: Compatibilizing bulk polymer blends by using organoclays. Macromolecules, **39**, 4793–4801 (2006). DOI: 10.1021/ma060125+

[15] Vo L. T., Giannelis E. P.: Compatibilizing poly(vinylidene fluoride)/nylon-6 blends with nanoclay. Macromolecules, **40**, 8271–8276 (2007). DOI: 10.1021/ma071508q

[16] Goodarzi V., Jafari S. H., Khonakdar H. A., Monemian S. A., Hässler R., Jehnichen D.: Nonisothermal crystallization kinetics and determination of surface-folding free energy of PP/EVA/OMMT nanocomposites. Journal of Polymer Science Part B: Polymer Physics, **47**, 674–684 (2009). DOI: 10.1002/polb.21672

[17] Huang J. J., Keskkula H., Paul D. R.: Rubber toughening of an amorphous polyamide by functionalized SEBS copolymers: Morphology and Izod impact behavior. Polymer, **45**, 4203–4215 (2004). DOI: 10.1016/j.polymer.2004.04.002

[18] Li W., Karger-Kocsis J., Thomann R.: Compatibilization effect of TiO_2 nanoparticles on the phase structure of PET/PP/TiO_2 nanocomposites. Journal of Polymer Science Part B: Polymer Physics, **47**, 1616–1624 (2009). DOI: 10.1002/polb.21752

[19] Robeson L. M.: Polymer blends: A comprehensive review. Hanser, Munich (2007).

[20] Mittal V.: Optimization of polymer nanocomposite properties. Wiley-VCH, Weinheim (2010).

[21] Schultiz J. M.: Polymer crystallization: The development of crystalline order in thermoplastic polymers. American Chemical Society, Washington (2001).

[22] Jafari S. H., Khonakdar H. A., Asadinezhad A.: A review on homopolymer, blends, and nanocomposites of poly (trimethylene terephthalate) as a new addition to the aromatic polyesters class. Iranian Polymer Journal, **17**, 19–38 (2008).

[23] Xue M-L., Yu Y-L., Chuah H. H.: Reactive compatibilization of poly(trimethylene terephthalate)/polypropylene blends by polypropylene-graft-maleic anhydride. Part 2. Crystallization behavior. Journal of Macromolecular Science Part B: Physics, **46**, 603–615 (2007). DOI: 10.1080/00222340701258008

[24] Lin S-W., Cheng Y-Y.: Miscibility, mechanical and thermal properties of melt-mixed poly(trimethylene terephthalate)/polypropylene blends. Polymer-Plastics Technology and Engineering, **48**, 827–833 (2009). DOI: 10.1080/03602550902994888

[25] Wang Y., Run M.: Non-isothermal crystallization kinetic and compatibility of PTT/PP blends by using maleic anhydride grafted polypropylene as compatibilizer. Journal of Polymer Research, **16**, 725–737 (2009). DOI: 10.1007/s10965-009-9279-6

[26] Upadhyay D., Mohanty S., Nayak S. K., Parvaiz M. R., Panda B. P.: Impact modification of poly(trimethylene terephthalate)/polypropylene blend nanocomposites: Fabrication and characterization. Journal of Applied Polymer Science, **120**, 932–943 (2011). DOI: 10.1002/app.33106

[27] Pegoretti A., Dorigato A., Brugnara M., Penati A.: Contact angle measurements as a tool to investigate the filler–matrix interactions in polyurethane–clay nanocomposites from blocked prepolymer. European Polymer Journal, **44**, 1662–1672 (2009). DOI: 10.1016/j.eurpolymj.2008.04.011

[28] Hári J., Dominkovics Z., Fekete E., Pukánszky B.: Kinetics of structure formation in PP/layered silicate nanocomposite. Express Polymer Letters, **3**, 684–691 (2009). DOI: 10.3144/expresspolymlett.2009.87

[29] Varga J.: Polypropylene structure, blends and composites. Chapman and Hall, London (1995).

[30] Favaro M. M., Branciforti M. C., Bretas R. E. S.: Influence of a terpolymer compatibilizer on the nanostructure of poly(trimethylene terephthalate)/montmorillonite nanocomposites. Polymers for Advanced Technologies, **20**, 940–949 (2009). DOI: 10.1002/pat.1343

[31] Martín Z., Jiménez I., Gómez-Fantous M. A., West M., Hitchcock A. P.: Interfacial interactions in polypropylene–organoclay–elastomer nanocomposites: Influence of polar modifications on the location of the clay. Macromolecules, **44**, 2179–2189 (2011). DOI: 10.1021/ma102707f

[32] Bordes P., Pollet E., Bourbigot S., Avérous L.: Structure and properties of PHA/clay nano-biocomposites prepared by melt intercalation. Macromolecular Chemistry and Physics, **209**, 1473–1484 (2008). DOI: 10.1002/macp.200800022

[33] Alexander, L. E.: X-ray diffraction methods in polymer science. Wiley, New York (1969).

[34] Zipper P., Jánosi A., Wrentschur E.: Scanning X-ray scattering of mouldings from semicrystalline polymers. Journal de Physique IV, **3**, 33–36 (1993). DOI: 10.1051/jp4:1993807

[35] Medellín-Rodríguez F. J., Mata-Padilla M., Sánchez-Valdes S., Vega-Díaz S., Dávalos-Montoya O.: Step-like melting mechanisms of isothermally crystallized isotactic polypropylene. Journal of Polymer Science Part B: Polymer Physics, **46**, 2188–2200 (2008). DOI: 10.1002/polb.21551

[36] Asadinezhad A., Jafari S. H., Khonakdar H. A., Böhme F., Hässler R., Häussler L.: Kinetics of isothermal crystallization and subsequent melting behavior of PTT/PA12 blend. Journal of Applied Polymer Science, **106**, 1964–1971 (2007). DOI: 10.1002/app.26808

[37] Tao Y., Mai K.: Non-isothermal crystallization and melting behavior of compatibilized polypropylene/recycled poly(ethylene terephthalate) blends. European Polymer Journal, **43**, 3538–3549 (2007). DOI: 10.1016/j.eurpolymj.2007.05.007

[38] Aravind I., Albert P., Ranganathaiah C., Kurian J. V., Thomas S.: Compatibilizing effect of EPM-g-MA in EPDM/poly(trimethylene terephthalate) incompatible blends. Polymer, **45**, 4925–4937 (2004). DOI: 10.1016/j.polymer.2004.04.063

[39] Li Y., Wang S., Zhang Y., Zhang Y.: Crystallization behavior of carbon black-filled polypropylene and polypropylene/epoxy composites. Journal of Applied Polymer Science, **102**, 104–118 (2006). DOI: 10.1002/app.23254

[40] Preschilla N., Abdul Rasheed A. S., Sahadevan S., Biswas A., Bellare J. R., Shyamroy S.: Study of layered silicate clays as synergistic nucleating agent for polypropylene. Journal of Polymer Science Part B: Polymer Physics, **48**, 1786–1794 (2010). DOI: 10.1002/polb.22044

[41] Jena A. K., Chaturvedi M. C.: Phase transformations in materials. Prentice Hall, New Jersey (1992).

eXPRESS Polymer Letters Vol.6, No.2 (2012) 159–168
Available online at www.expresspolymlett.com
DOI: 10.3144/expresspolymlett.2012.17

Synergistic effect in conductive networks constructed with carbon nanofillers in different dimensions

S. M. Zhang[1], *L. Lin*[1], *H. Deng*[1*], *X. Gao*[1], *E. Bilotti*[2], *T. Peijs*[2,3], *Q. Zhang*[1], *Q. Fu*[1]

[1]College of Polymer Science and Engineering, State Key Laboratory of Polymer Materials Engineering, Sichuan University, 610065 Chengdu, People's Republic of China
[2]Queen Mary University of London, School of Engineering and Materials Science, and Centre of Materials Research, Mile End Road, E1 4NS London, UK
[3]Eindhoven University of Technology, Eindhoven Polymer Laboratories, 5600 MB Eindhoven, The Netherlands

Received 27 July 2011; accepted in revised form 15 September 2011

Abstract. Herein, investigation on synergistic effect during network formation for conductive network constructed with carbon nanofillers in different dimensions is conducted. Multi-walled carbon nanotubes (MWNTs) and carbon black (CB) are employed as conductive fillers in this system. Morphological control of the conductive network is realized by adjusting the ratio between different fillers. Classical percolation threshold theory and adjusted excluded volume theory are used to analyze the electrical percolating behavior of these systems. It is observed that the percolation threshold of hybrid fillers filled conductive polymer composites (CPCs) is much lower than that of MWNTs or CB filled CPCs, and it can be reduced from 2.4 to 0.21 wt% by replacing half of the MWNTs with CB. Possible mechanism of this phenomenon is discussed together with morphological observation. A model is proposed to understand the mechanism of the percolation behavior in the composites containing various proportions of nanofillers. Our work is important for the design and preparation of low cost conductive polymer composites with novel electrical property.

Keywords: *nanocomposites, carbon nanotubes, carbon black, synergistic effect, electrical percolation*

1. Introduction

Conductive polymer composites (CPCs) have attracted a lot of attention in the past few decades, and have many potential applications including antistatic [1], electromagnetic interference shielding [2], sensing [3–8], flexible solar cell electrodes [9], field emission [10, 11], etc. CPCs can be fabricated by adding conductive filler into an insulating polymer matrix, where a sudden jump in conductivity can be observed while a critical content of filler is incorporated. Classic percolation theory is often used to describe such a phenomenon [12], and carbon nanotubes (CNTs), carbon black (CB), graphite, graphene nanoplates etc. are often used as electrically conductive fillers. CNTs are believed to be one of the most interesting conductive fillers due to their ultra-high aspect ratio and intrinsic conductivity [13–17]. For example, the percolation threshold of CPCs containing CNTs can be as low as 0.0025 wt% [18–21]. In these systems, percolation thresholds are significantly lower than 0.1 wt%. It is attributed to the kinetic percolation which allows for particle movement and re-aggregation [22], and these results are often achieved in emulsion or solution-based systems under controlling the viscosity of the aqueous composite mixture and the shear intensity of the stirring process. However, percolation threshold is often much higher for composites prepared by melt compounding. McNally *et al.* [23] observed a percolation threshold of 7.5 wt% for

*Corresponding author, e-mail: huadeng@scu.edu.cn

PE/MWNTs composites prepared by melt blending. The value is often between 1 to 5 wt% for melt compounded systems and considered as statistical percolation threshold [22]. The mechanism behind this significant difference between kinetic and statistical percolation is the prohibition of re-aggregation between CNTs during melt compounding process [22, 24]. It was reported that the re-aggregation process of CNTs within polymer melt can take hours to complete [25].

To achieve better conductivity or lower cost, more than one kind of filler, particularly fillers in different aspect ratios, are used to prepare CPCs. Regarding the formation of conductive network with fillers in different aspect ratios, theoretical study has shown that it is not necessary to build conductive network with high aspect ratio filler alone [26], and the percolation threshold is sensitive to the portion of high aspect ratio filler in a system containing fillers in different aspect ratios [27]. There are a number of investigations reported in the literature on mixed carbon fillers filled CPCs [26, 28–31]. However, the percolation thresholds of these systems filled with mixed fillers are only simple average of that for systems filled with a particular kind of carbon filler. Therefore, more study is needed to study the true synergistic effect between conductive fillers of different dimensionality in building conductive network.

In current study, CPCs based on mixed filler between carbon nanofillers in different dimensions and polypropylene will be fabricated. It is well known that polyolefin is a widely used material and its processability is prominent. Moreover, due to the difference in filler dimension and intrinsic structure, the networks formed with mixed fillers might illustrate interesting percolating behavior in CPCs. Furthermore, this study could be used as an example to demonstrate the real synergistic effect between different dimensional fillers and replace high price and aspect ratio filler with lower ones. Multiwall carbon nanotubes (MWNTs) and CB will be used as conductive fillers. Classical percolation threshold theory and adjusted excluded volume theory [26] will be used to analyze the electrical percolating behavior of current systems.

2. Experimental

2.1. Materials

MWNTs (NC 7000, Nanocyl S.A., Belgium) were used for the preparation of CPCs. These MWNTs have an outer diameter of 10 nm, a length of 1.5 μm, and a surface area of 250–300 $m^2 \cdot g^{-1}$ according to the producer. CB (VXC-605, Cabot Co. Ltd, U.S.) is acetylene carbon black with DBP absorption of 148 cm^3/100 g, and a primary particle diameter of 34 nm. A maleic anhydride grafted polypropylene (PP-*g*-MA) (E43, Westlake Chemical, U.S.) was used as compatibilizer. Polypropylene (PP, Basell Adsyl 5C39F, Basell, U.S.) is a copolymer (M_w = 320 $kg \cdot mol^{-1}$, MFI = 5.5 $g \cdot min^{-1}$) containing 98% of PP and 2% of ethylene.

2.2. Composites preparation

Fillers were melt-blended with PP copolymer (co-PP) in an internal mixer (XSS-300, Qingfeng Mould Factory, Shanghai, China) at 200°C, 100 rpm for 15 min in order to prepare the masterbatch with high filler content. The mixture of MWNT and CB are mentioned as 'Hybrid fillers' in the following. Then, the masterbatch, co-PP and E43 were added into a double-screw micro-extruder (HAAKE Mini-Lab, Thermo Electron, Germany) at 200°C, 100 rpm for 15 min to prepare composites containing different filler content. The content of E43 is kept at 10 wt% for all composites in this study. The extruded strand was then cut and hot-pressed (KT-0701, Kangte Technology Co. Ltd, Beijing, China) into a film with a thickness about 200 μm at 200°C, 20 MPa for 5 min.

2.3. Composites characterization

2.3.1. Electrical measurements

Direct current (DC) electrical resistivity is measured for the composites at different processing stages. Two points method was used. To avoid contact resistance, silver paint was applied on both ends of the tape. As a result, contact resistance is negligible compared to sample resistance. The resistance is measured by a Keithley 6487 picoammeter (Keithley Instruments Inc. Ohio, USA) at a constant voltage of 1 V. The results were recorded after the voltage had been exerted for 5 seconds. Resistivity can be calculated using the resistance by Equation (1):

$$\rho = \frac{R \cdot w \cdot t}{l} \quad (1)$$

where R is the resistance of the sample, w, t, and l represent width, thickness and length of the sample, respectively. Resistivity exceeding 10^4 Ω·m is not measurable with the current set-up and these films are therefore classified as non-conductive.

2.3.2. Scanning electron microscope (SEM)

Morphology studies were carried out on a scanning electron microscope (SEM, Inspect F, FEI company, USA) under an acceleration voltage of 20 kV. For the investigation of conductive networks, uncoated specimens were used. To study the morphology of network constructed with lower filler content, standard gold-coated specimens were used.

3. Results and discussion

3.1. Percolation threshold in isotropic systems

The electrical conductivity of isotropic nanocomposites is plotted as a function of filler content in Figure 1. Composites containing only MWNTs, only CB, both MWNTs and CB in the ratio of 1:1, 1:4 and 4:1 are labeled as: CPC-MWNT, CPC-CB, CPC-$MWNT_1$-CB_1, CPC-$MWNT_1$-CB_4 and CPC-$MWNT_4$-CB_1, respectively. The result that the CPC-CB system exhibits a higher percolation threshold than the CPC-MWNT system is anticipated due to the higher aspect ratio of MWNTs comparing with CB. Further experiments were carried out to investigate the influence of hybrid nanofillers and the ratio between them on the electrical percolating behavior. Interestingly, a measurable resistivity is obtained for the composites containing a hybrid filler consisting of 0.25 wt% MWNTs and 0.25 wt% CB, while the resistivity of the composites filled with MWNTs alone could only become conductive for the filler contents above 2 wt%. Therefore, the percolation threshold is reduced significantly by using a hybrid nanofiller system. As shown in Figure 1, CPC-$MWNT_1$-CB_1 are more conductive than CPC-$MWNT_1$-CB_4 at the same total filler content. Furthermore, the resistivity of the composites containing hybrid nanofillers is higher than CPC-MWNT at the same filler content. However, the resistivity of CPC-$MWNT_4$-CB_1 and CPC-$MWNT_1$-CB_1 is very close to that of CPC-MWNT. Therefore, the synergistic effect between CB and MWNTs allows the partial replacement of high aspect ratio and high priced nanofillers (MWNTs) with low aspect ratio, low priced fillers (CB) in CPCs. This agrees well with the theoretical results reported in literature [27]. More importantly, the synergistic effect between CB and MWNTs results in a reduced percolation threshold for CPC-$MWNT_1$-CB_1 compared with CPC-MWNT.

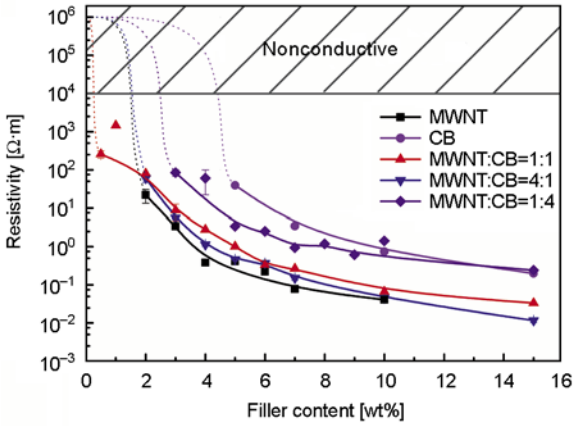

Figure 1. DC electrical resistivity of nanocomposites: CPC-MWNT, CPC-CB, CPC-$MWNT_1$-CB_1, CPC-$MWNT_4$-CB_1 and CPC-$MWNT_1$-CB_4. Please note that the dot lines are drawn to guide the eye.

In order to perform a more in-depth analysis, the data of the above five systems were fitted according to the classical percolation scaling law, see Equation (2):

$$\sigma = \sigma_0 (P - P_c)^t \quad (2)$$

for $P > P_c$

where σ_0 is a scaling factor, P_c is the percolation threshold, σ is the conductivity of the CPC and P is the filler content in the CPC [12]. The exponent t is a parameter which depends on the dimensionality of the conductive network. It is expected to vary for different materials with calculated values of $t \approx 1.3$ and $t \approx 2.0$ for two and three dimension networks, respectively. As widely reported in the literature [4, 32], the percolation threshold of CPCs can be determined accurately, and information on the dimensionality of the conducting network can be obtained through the fitting of classical percolation scaling law to experimentally obtained conductivity data. Hence, the percolation threshold P_c and exponent t are obtained, the results are shown in Figure 2.

Furthermore, excluded volume theory has been widely used in conductive polymer composites filled with one type of conductive filler to analyze their conductive percolation behavior [19, 24].

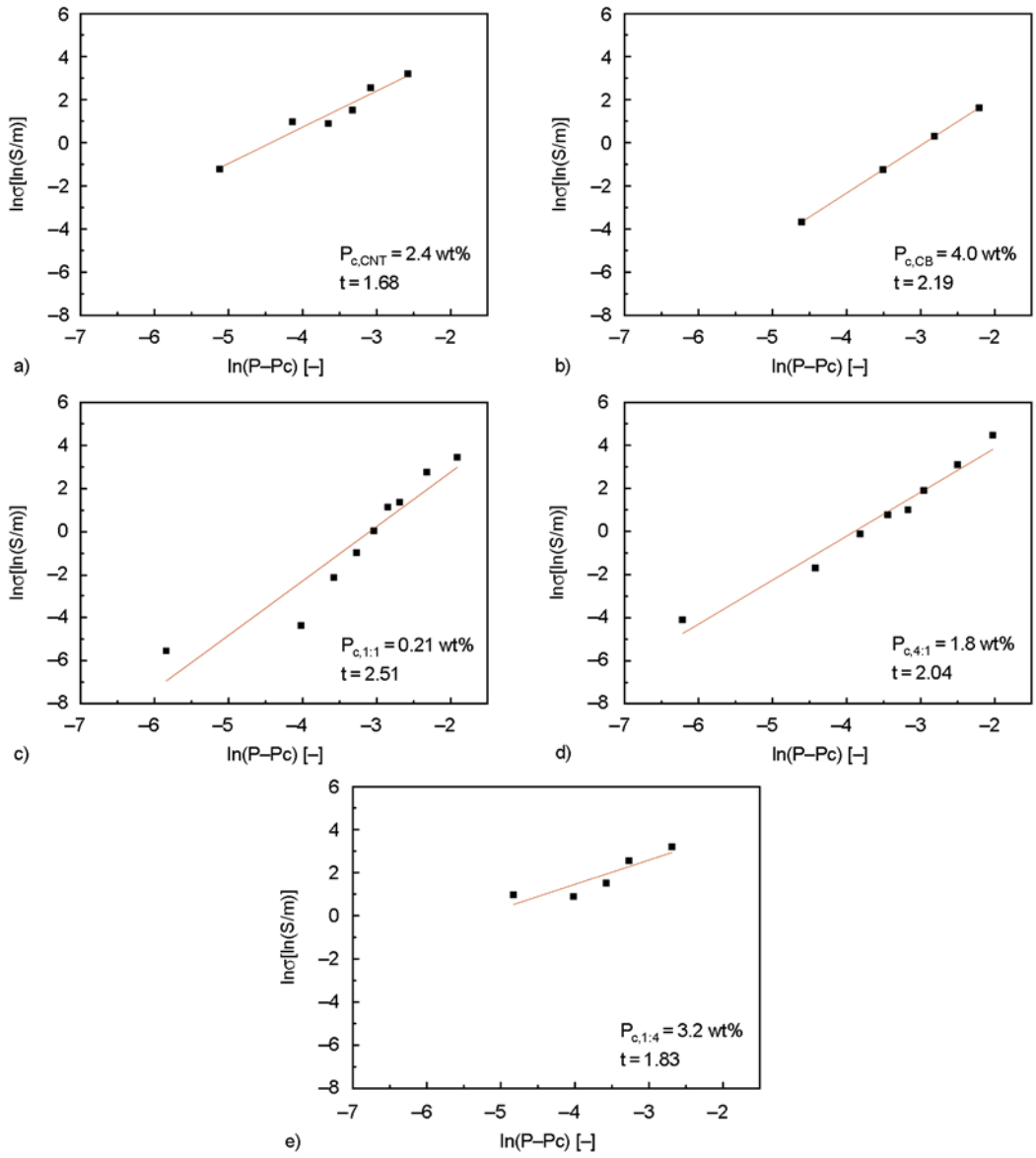

Figure 2. Plots of classical percolation threshold theory fitting of the composites: (a) CPC-MWNT; (b) CPC-CB; (c) CPC-$MWNT_1$-CB_1; (d) CPC-$MWNT_4$-CB_1; (e) CPC-$MWNT_1$-CB_4. R^2 of these curves are: (a) R^2 = 0.94; (b) R^2 = 1.00; (c) R^2 = 0.87; (d) R^2 = 0.96; (e) R^2 = 0.73.

Recently, it is reported that the percolation threshold of ternary systems containing two types of conductive fillers can be estimated by using an equation derived from the excluded volume approach [26, 29, 33] (Equation (3)):

$$\frac{m_{CNT}}{P_{c,CNT}} + \frac{m_{CB}}{P_{c,CB}} = 1 \quad (3)$$

where m_{CNT} and m_{CB} are the mass fraction in the ternary systems, $P_{c,CNT}$ and $P_{c,CB}$ are the percolation thresholds in the binary systems for CNT and CB, respectively. Therefore, the theoretical percolation threshold of the binary systems can be calculated using Equation (3). Using the system of CPC-$MWNT_1$-CB_1 as an example, it is possible to calculate the filler content of each particle for the ternary system using Equation (4) taking into account the percolation threshold of the binary systems shown in Figure 2:

$$m_{CNT} = m_{CB} = 1.5 \text{ wt\%} \quad (4)$$

Thus, the theoretical percolation threshold of the ternary system is calculated as shown in Equation (5):

$$P_{c,1:1} = 2m_{CNT} = 2m_{CB} = 3.0 \text{ wt\%} \quad (5)$$

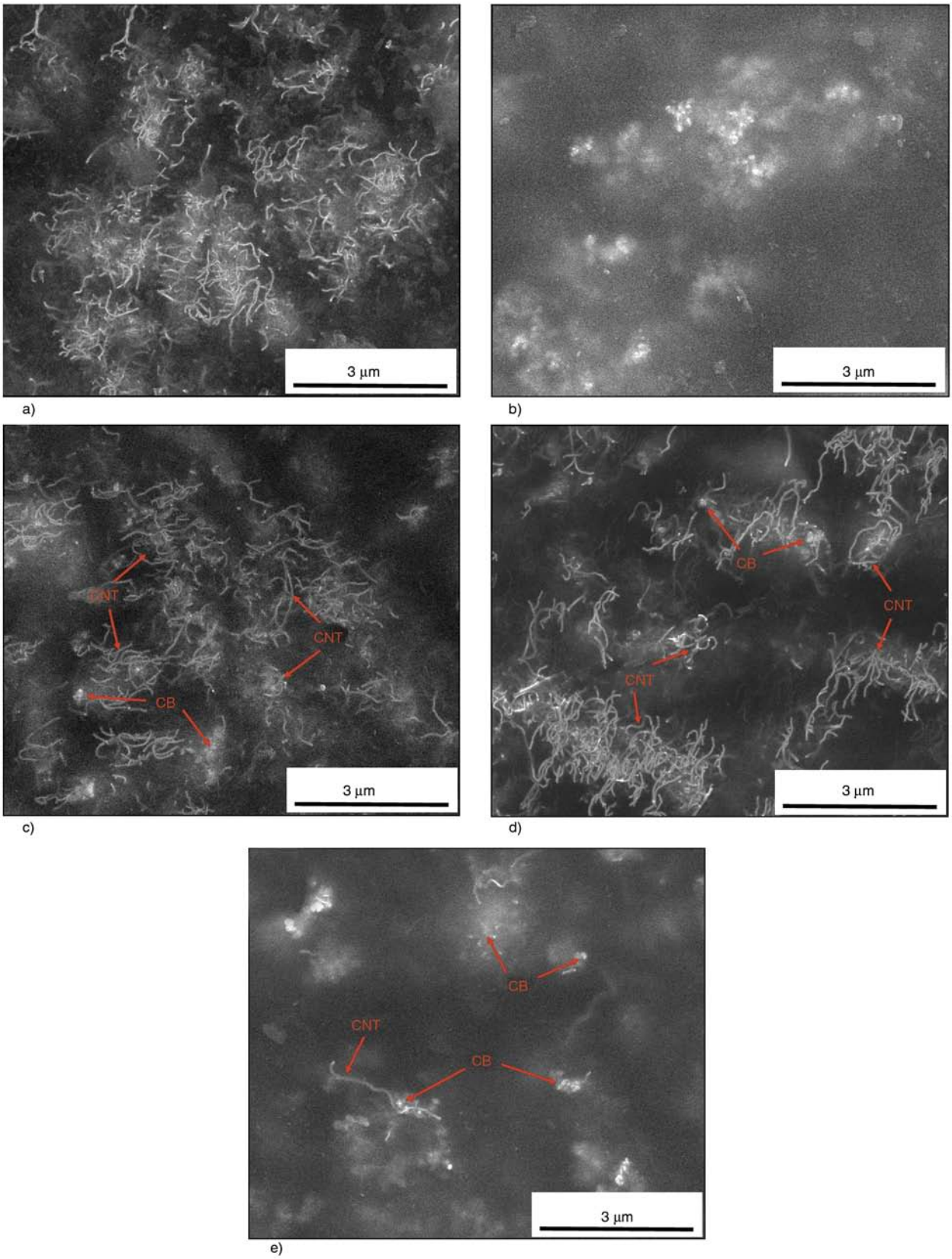

Figure 3. SEM micrographs of isotropic CPCs: (a) MWNTs (10 wt%)/E43/co-PP; (b) CB (10 wt%)/E43/co-PP; (c) MWNTs (5 wt%)/CB (5 wt%)/E43/co-PP; (d) MWNTs (8 wt%)/CB (2 wt%)/E43/co-PP; (e) MWNTs (2 wt%)/CB (8 wt%)/E43/co-P

An obvious difference can be observed between the experimental percolation threshold (0.21 wt%) and calculated theoretical one (3.0 wt%) for CPC-$MWNT_1$-CB_1. Unlike reported in previous literature [29], the difference between experimental percolation threshold (0.5 wt%) and the theoretical one (3.0 wt%) is rather obvious. As discussed above, a measurable resistivity is obtained in MWNTs (0.25 wt%)/CB (0.25 wt%)/E43/co-PP while the resistivity of the composites filled with MWNTs alone could only become conductive for the filler contents above 2 wt%, thus, a statement on the presence of synergistic effect in percolation dynamics in such a system can be made. As revealed in Figure 3, MWNTs and CB are evenly dispersed in the polymer matrix and the electrical pathways are co-formed by MWNTs and CB. Additionally, $P_{c,4:1}$ and $P_{c,1:4}$ can be calculated using the same method as 2.6 and 3.5 wt%, respectively. Both of them are similar with the experimental values shown in Figure 2 (1.8 and 3.2 wt%). This indicates that there is no synergistic effect in CPC-$MWNT_4$-CB_1 and CPC-$MWNT_1$-CB_4.

3.2. Morphology of the composites

To understand the synergistic effect between MWNTs and CB, SEM was carried out to investigate the morphology of the composites with different filler contents and proportions. High accelerating voltage is applied to give enriched secondary electrons to perform voltage contrast imaging as demonstrated in literature [34–36]. Figure 3a and 3b shows the morphology of the conductive network formed by MWNTs and CB, respectively, and Figure 3c, 3d and 3e shows that of hybrid fillers, where the bright phase is conductive filler and the black background is co-PP matrix.

As shown in Figure 3, isotropic conductive networks are obtained in the composites for the conductive networks formed by MWNTs and CB. Because of the high aspect ratio and fibrous shape, MWNTs filled composite showed such a network that MWNTs are entangled to form conductive pathways. However, the network formed by CB is obviously different from that formed by MWNTs as CB is a three dimensional, sphere shaped filler. And the conductive pathway was formed through the aggregations of CB particles. It is noted that the conductive networks formed with mixed fillers (see Figure 3) demonstrate a complex nanostructure of multiple MWNTs bridging adjacent CB particles. Since the natural structure and proportions of the fillers in ternary system are different, the morphology displays diverse features.

Since these CPCs demonstrate interesting electrical percolation behavior while hybrid fillers are contained. More SEM study is carried out to further investigate their morphology. Figure 4a shows the morphology for CPCs containing 0.25 wt% MWNTs and 0.25 wt% CB. It is noted that clear conductive network can be observed, nevertheless, no network can be observed in the representative picture from CPCs containing 0.5 wt% hybrid filler (MWNTs:CB) in the ratio of: 4:1, 1:4, 5:0, 0:5. This further con-

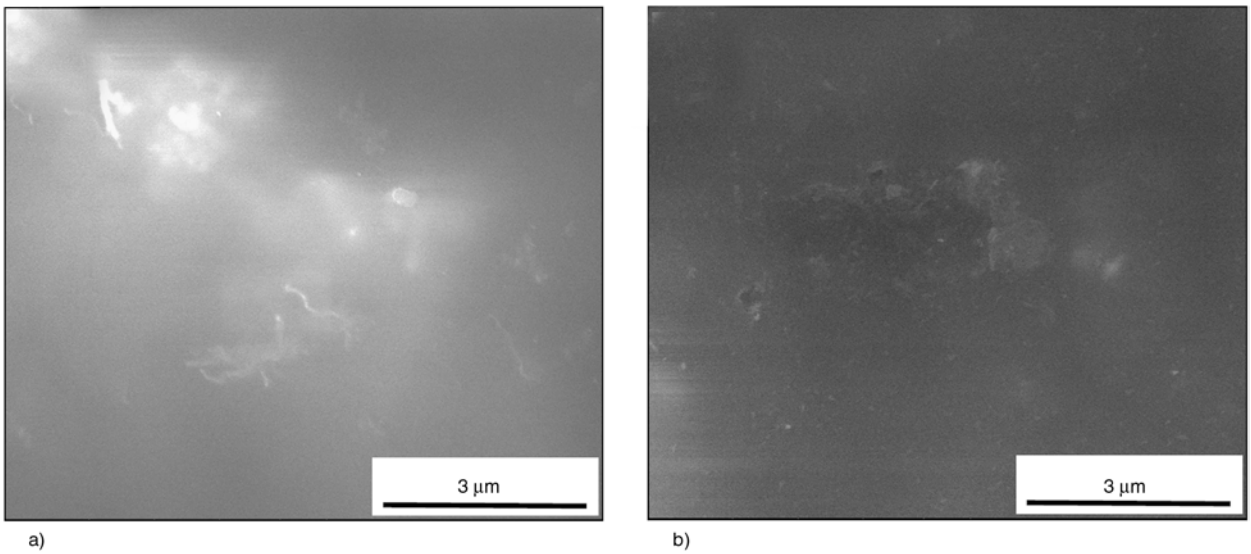

Figure 4. SEM image for CPCs containing a total filler content of 0.5 wt% (a) CPC-$MWNT_1$-CB_1 (b) a representative picture of CPC-$MWNT_4$-CB_1, CPC-$MWNT_1$-CB_4, CPC-MWNT and CPC-CB

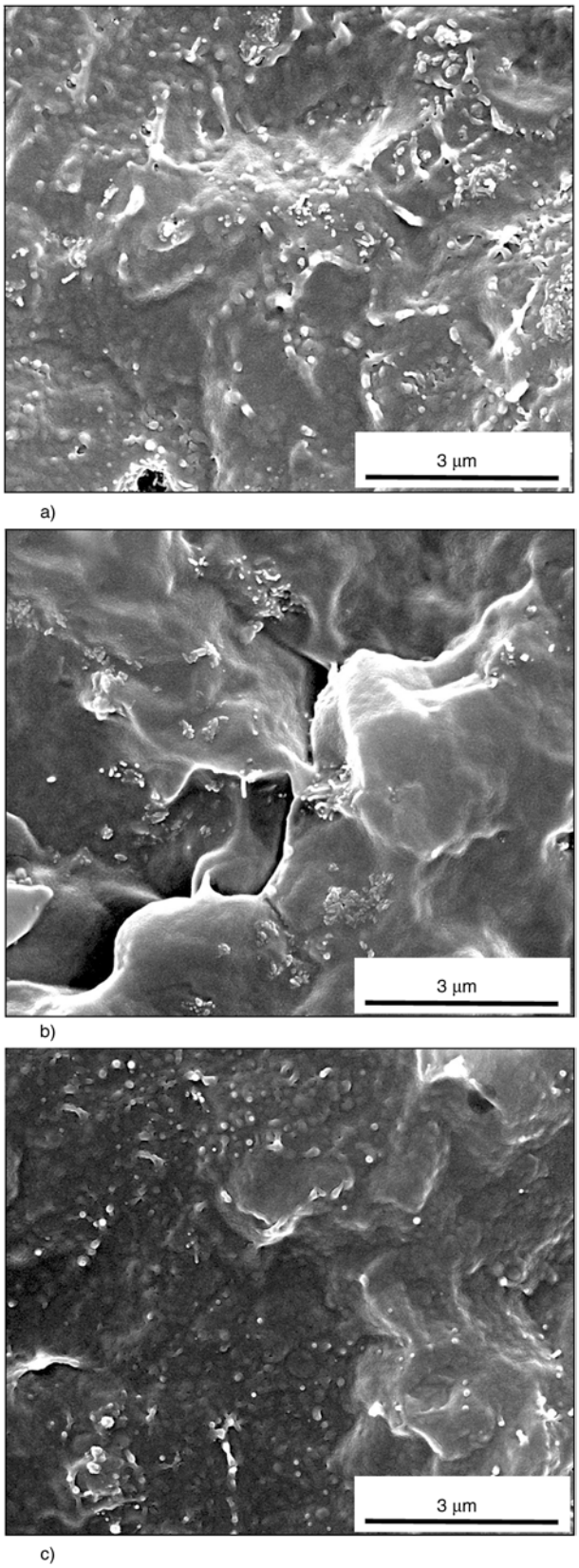

Figure 5. Fracture surface of CPCs containing 0.5 wt% of hybrid filler, (a) CPC-$MWNT_1$-CB_1, (b) CPC-$MWNT_4$-CB_1 and (c) CPC-$MWNT_1$-CB_4

firms the presence of conductive network in the CPCs containing 0.25 wt% MWNTs and 0.25 wt% CB, and the absence of that in the rest, as non-conductive specimens are charged up during voltage contrast imaging in SEM [35, 36].

It is well known that MWNTs has higher conductivity than CB. Nevertheless, it is observed that the no measurable conductivity is obtained for CPC-$MWNT_4$-CB_1 and CPC-$MWNT_1$-CB_4 containing 0.5 wt% hybrid filler, while CPC-$MWNT_1$-CB_1 containing the same amount of hybrid filler is conductive, despite of the fact that less highly conductive MWNTs is contained comparing with CPC-$MWNT_4$-CB_1. To try to understand this, the morphology of the gold coated fracture surface of these CPCs containing hybrid fillers is investigated with SEM (see Figure 5). It is noted that MWNTs are more entangled in the CPCs containing more MWNTs. Similar effect is often observed in CNT/polymer composites [37]. Therefore, the extra MWNTs contained in CPC-$MWNT_4$-CB_1 are entangled in these bundles, and not being used to building up conductive networks effectively. This might be responsible for the effect observed.

3.3. The mechanism of conductive network formation

According to the observation and discussion above, the following mechanism is proposed to explain the electrical percolation behavior observed. Comparing CPC-CB with CPC-MWNT, a higher percolation threshold and higher resistivity are obtained in the former system. It is caused by the lower aspect ratio, lower specific surface area and higher intrinsic resistivity of CB comparing with MWNTs. Regarding the ternary systems containing both CB and MWNTs, co-supporting networks are formed with two types of fillers. For the CPCs containing low filler content (e.g. 0.5 wt%, see Figure 6a, 6b, 6c), conductive networks are obtained in CPC-$MWNT_1$-CB_1 thanks to the bridges provides by CB to MWNTs local networks. For CPC-$MWNT_4$-CB_1, the MWNTs become more entangled, and not being efficiently used to build up conductive network. While for CPC-$MWNT_1$-CB_4, the amount of high aspect ratio filler is too low to build conductive networks. Therefore, CPC-$MWNT_1$-CB_1 demonstrates much lower percolation threshold than the rest of the CPCs.

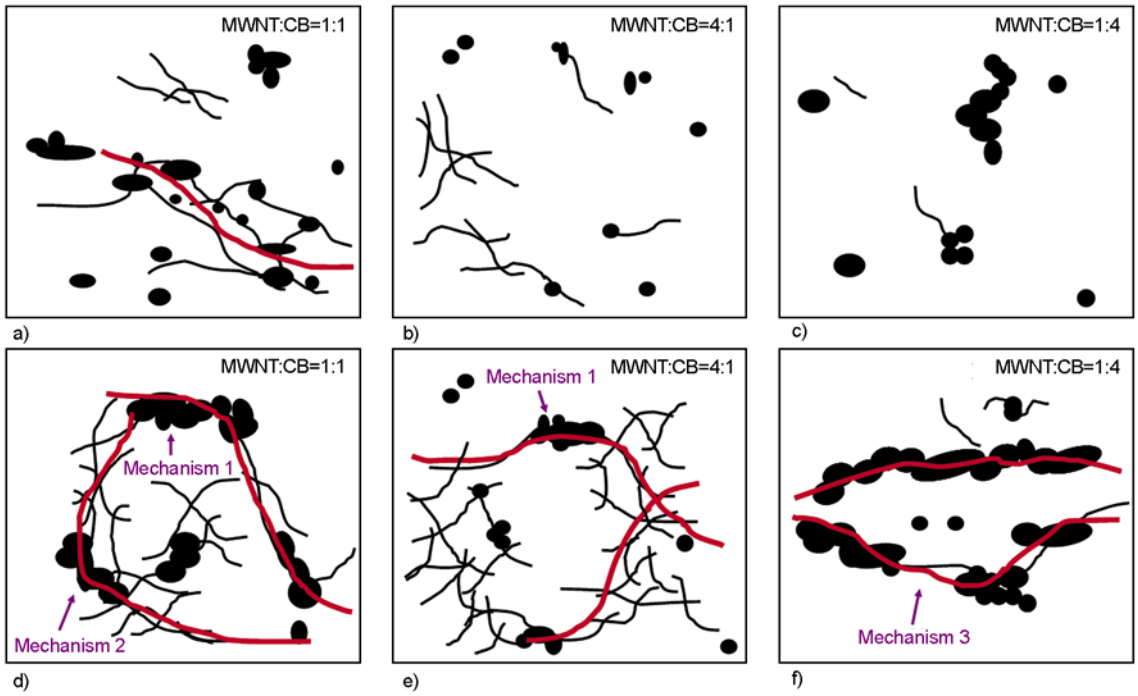

Figure 6. Mechanism for the formation of conductive pathways by MWNTs and CB in ternary systems: (a, b, c) are composites filled with insufficient filler content; (d, e, f) are composites filled with sufficient filler content

In the CPCs containing relative high filler content, the electrical resistivity is higher in the CPCs containing more MWNTs. This might be due to the fact that the conductive network is already established at these filler contents, therefore, CPC-$MWNT_1$-CB_1 is not demonstrating any synergistic effect in conductivity comparing with other CPCs. It is thought that there are three different mechanisms of conductive network formation in such a ternary system (see Figure 6d, 6e, 6f). Mechanism 1: shortcut of 'dead' network branches caused by new active branches of networks co-formed by CB [29]; mechanism 2: incorporation of CB into active 'MWNT' networks through bridging MWNT local networks with CB [29]; and mechanism 3: bridging local contacts between CB clusters through MWNTs. In the different ternary systems investigated in current study, mechanism 3 might be dominant in CPC-$MWNT_1$-CB4, as most of the conductive networks are formed by CB. Therefore, slightly higher resistivity is observed for these CPCs at higher filler content due to the higher intrinsic resistivity of CB comparing with MWNTs (see Figure 1). Mechanism 1 might dominate in CPC-$MWNT_4$-CB_1, as most of the conductive networks are formed by MWNTs. As shown in Figure 6d, both mechanisms might occur simultaneously in CPC-$MWNT_1$-CB_1.

4. Conclusions

With the effort to partially replace high price filler (MWNTs) with lower ones (such as CB), a melt processing based method is used to fabricate CPCs filled with carbon nanofillers in different dimensions: MWNTs and CB. Morphological difference of the conductive network formed by the nanofillers is observed due to difference in dimension between these fillers. Moreover, synergistic effect between carbon nanofillers is demonstrated in isotropic CPCs. The percolation threshold of hybrid fillers filled CPCs is much lower than that of MWNTs or CB filled CPCs, and it can be reduced from 2.4 to 0.21 wt% by replacing half of the MWNTs with CB. Regarding the effect of different filler ratio, it is demonstrated that the lowest percolation threshold is observed while the ratio is 1:1. With increasing ratio, more entanglements between filler are observed in the system, this might be responsible for the increase percolation threshold. Nevertheless, the CPCs containing more MWNTs at filler content well above percolation are demonstrating lower resistivity despite of the filler ratio, this is thought to be caused by the fact that relative stable conductive network are already building at these filler contents. This work could provide interesting method for the preparation of low cost, high performance CPCs.

Regarding future work, it would be interesting to investigate the effect of surface properties of carbon nanofillers on the synergistic effect observed, since the surface properties of CB is reported to be closely related with its electrical percolating behavior in CPCs [38]. This might give explanation for the difference between current study and the ones report in literature, where such a synergistic effect was not observed in similar systems [26, 29].

Acknowledgements

We express our sincere thanks to the National Natural Science Foundation of China for financial support (51003063, 51011130160, 50873063). We also would like to thank Prof. Z. M. Li for providing us with the carbon black used in this study.

References

[1] Deng H., Skipa T., Bilotti E., Zhang R., Lellinger D., Mezzo L., Fu Q., Alig I., Peijs T.: Preparation of high-performance conductive polymer fibers through morphological control of networks formed by nanofillers. Advanced Functional Materials, **20**, 1424–1432 (2010). DOI: 10.1002/adfm.200902207

[2] Ramasubramaniam R., Chen J., Liu H. Y.: Homogeneous carbon nanotube/polymer composites for electrical applications. Applied Physics Letters, **83**, 2928–2930 (2003). DOI: 10.1063/1.1616976

[3] Thostenson E. T., Chou T-W.: Carbon nanotube networks: Sensing of distributed strain and damage for life prediction and self healing. Advanced Materials, **18**, 2837–2841 (2006). DOI: 10.1002/adma.200600977

[4] Zhang R., Baxendale M., Peijs T.: Universal resistivity–strain dependence of carbon nanotube/polymer composites. Physical Review B, **76**, 195433/1–195433/5 (2007). DOI: 10.1103/PhysRevB.76.195433

[5] Gao L. M., Thostenson E. T., Zhang Z., Chou T-W.: Sensing of damage mechanisms in fiber-reinforced composites under cyclic loading using carbon nanotubes. Advanced Functional Materials, **19**, 123–130 (2009). DOI: 10.1002/adfm.200800865

[6] Bouvree A., Feller J-F., Castro M., Grohens Y., Rinaudo M.: Conductive polymer nano-bioComposites (CPC): Chitosan-carbon nanoparticle a good candidate to design polar vapour sensors. Sensors and Actuators B: Chemical, **138**, 138–147 (2009). DOI: 10.1016/j.snb.2009.02.022

[7] Feller J. F., Langevin D., Marais S.: Influence of processing conditions on sensitivity of conductive polymer composites to organic solvent vapours. Synthetic Metals, **144**, 81–88 (2004). DOI: 10.1016/j.synthmet.2004.02.006

[8] Castro M., Lu J., Bruzaud S., Kumar B., Feller J-F.: Carbon nanotubes/poly(ε-caprolactone) composite vapour sensors. Carbon, **47**, 1930–1942 (2009). DOI: 10.1016/j.carbon.2009.03.037

[9] Tae Kim A., Kim H. S., Lee S. S., Park M.: Single-walled carbon nanotube/silicone rubber composites for compliant electrodes. Carbon, **50**, 444–449 (2012). DOI: 10.1016/j.carbon.2011.08.070

[10] Connolly T., Smith R. C., Hernandez Y., Gun'ko Y., Coleman J. N., Carey J. D.: Carbon-nanotube–polymer nanocomposites for field-emission cathodes. Small, **5**, 826–831 (2009). DOI: 10.1002/smll.200801094

[11] Alexandrou I., Kymakis E., Amaratunga G. A. J.: Polymer–nanotube composites: Burying nanotubes improves their field emission properties. Applied Physics Letters, **80**, 1435–1437 (2002). DOI: 10.1063/1.1449537

[12] Stauffer D., Aharony A.: Introduction to percolation theory. Taylor and Francis, London (1994).

[13] Li Z., Luo G., Wei F., Huang Y.: Microstructure of carbon nanotubes/PET conductive composites fibers and their properties. Composites Science and Technology, **66**, 1022–1029 (2006). DOI: 10.1016/j.compscitech.2005.08.006

[14] Martin C. A., Sandler J. K. W., Shaffer M. S. P., Schwarz M-K., Bauhofer W., Schulte K., Windle A. H.: Formation of percolating networks in multi-wall carbon-nanotube–epoxy composites. Composites Science and Technology, **64**, 2309–2316 (2004). DOI: 10.1016/j.compscitech.2004.01.025

[15] Wang Q., Dai J., Li W., Wei Z., Jiang J.: The effects of CNT alignment on electrical conductivity and mechanical properties of SWNT/epoxy nanocomposites. Composites Science and Technology, **68**, 1644–1648 (2008). DOI: 10.1016/j.compscitech.2008.02.024

[16] Zhang L., Wan C., Zhang Y.: Morphology and electrical properties of polyamide 6/polypropylene/multi-walled carbon nanotubes composites. Composites Science and Technology, **69**, 2212–2217 (2009). DOI: 10.1016/j.compscitech.2009.06.005

[17] Gao X., Zhang S., Mai F., Lin L., Deng Y., Deng H., Fu Q.: Preparation of high performance conductive polymer fibres from double percolated structure. Journal of Materials Chemistry, **21**, 6401–6408 (2011). DOI: 10.1039/C0JM04543H

[18] Bryning M. B., Islam M. F., Kikkawa J. M., Yodh A. G.: Very low conductivity threshold in bulk isotropic single-walled carbon nanotube–epoxy composites. Advanced Materials, **17**, 1186–1191 (2005). DOI: 10.1002/adma.200401649

[19] Sandler J. K. W., Kirk J. E., Kinloch I. A., Shaffer M. S. P., Windle A. H.: Ultra-low electrical percolation threshold in carbon-nanotube-epoxy composites. Polymer, **44**, 5893–5899 (2003).
DOI: 10.1016/S0032-3861(03)00539-1

[20] Grunlan J. C., Mehrabi A. R., Bannon M. V., Bahr J. L.: Water-based single-walled-nanotube-filled polymer composite with an exceptionally low percolation threshold. Advanced Materials, **16**, 150–153 (2004).
DOI: 10.1002/adma.200305409

[21] Zhou Y. X., Wu P. X., Cheng Z-Y., Ingram J., Jeelani S.: Improvement in electrical, thermal and mechanical properties of epoxy by filling carbon nanotube. Express Polymer Letters, **2**, 40–48 (2008).
DOI: 10.3144/expresspolymlett.2008.6

[22] Bauhofer W., Kovacs J. Z.: A review and analysis of electrical percolation in carbon nanotube polymer composites. Composites Science and Technology, **69**, 1486–1498 (2009).
DOI: 10.1016/j.compscitech.2008.06.018

[23] McNally T., Pötschke P., Halley P., Murphy M., Martin D., Bell S. E. J., Brennan G. P., Bein D., Lemoine P., Quinn J. P.: Polyethylene multiwalled carbon nanotube composites. Polymer, **46**, 8222–8232 (2005).
DOI: 10.1016/j.polymer.2005.06.094

[24] Deng H., Zhang R., Bilotti E., Loos J., Peijs T.: Conductive polymer tape containing highly oriented carbon nanofillers. Journal of Applied Polymer Science, **113**, 742–751 (2009).
DOI: 10.1002/app.29624

[25] Alig I., Lellinger D., Dudkin S. M., Pötschke P.: Conductivity spectroscopy on melt processed polypropylene–multiwalled carbon nanotube composites: Recovery after shear and crystallization. Polymer, **48**, 1020–1029 (2007).
DOI: 10.1016/j.polymer.2006.12.035

[26] Sun Y., Bao H-D., Guo Z-X., Yu J.: Modeling of the electrical percolation of mixed carbon fillers in polymer-based composites. Macromolecules, **42**, 459–463 (2009).
DOI: 10.1021/ma8023188

[27] Otten R. H. J., van der Schoot P.: Continuum percolation of polydisperse nanofillers. Physical Review Letters, **103**, 225704/1–225704/4 (2009).
DOI: 10.1103/PhysRevLett.103.225704

[28] Ma P-C., Liu M-Y., Zhang H., Wang S-Q., Wang R., Wang K., Wong Y-K., Tang B-Z., Hong S-H., Paik K-W., Kim J-K.: Enhanced electrical conductivity of nanocomposites containing hybrid fillers of carbon nanotubes and carbon black. ACS Applied Materials and Interfaces, **1**, 1090–1096 (2009).
DOI: 10.1021/am9000503

[29] Sumfleth J., Adroher X. C., Schulte K.: Synergistic effects in network formation and electrical properties of hybrid epoxy nanocomposites containing multi-wall carbon nanotubes and carbon black. Journal of Materials Science, **44**, 3241–3247 (2009).
DOI: 10.1007/s10853-009-3434-7

[30] Etika K. C., Liu L., Hess L. A., Grunlan J. C.: The influence of synergistic stabilization of carbon black and clay on the electrical and mechanical properties of epoxy composites. Carbon, **47**, 3128–3136 (2009).
DOI: 10.1016/j.carbon.2009.07.031

[31] Feller J. F., Bruzaud S., Grohens Y.: Influence of clay nanofiller on electrical and rheological properties of conductive polymer composite. Materials Letters, **58**, 739–745 (2004).
DOI: 10.1016/j.matlet.2003.07.010

[32] Deng H., Bilotti E., Zhang R., Loos J., Peijs T.: Effect of thermal annealing on the electrical conductivity of high-strength bicomponent polymer tapes containing carbon nanofillers. Synthetic Metals, **160**, 337–344 (2010).
DOI: 10.1016/j.synthmet.2009.11.001

[33] Balberg I., Anderson C. H., Alexander S., Wagner N.: Excluded volume and its relation to the onset of percolation. Physial Review B, **30**, 3933–3943 (1984).
DOI: 10.1103/PhysRevB.30.3933

[34] Deng H., Zhang R., Reynolds C. T., Bilotti E., Peijs T.: A novel concept for highly oriented carbon nanotube composite tapes or fibres with high strength and electrical conductivity. Macromolecular Materials and Engineering, **294**, 749–755 (2009).
DOI: 10.1002/mame.200900151

[35] Loos J., Alexeev A., Grossiord N., Koning C. E., Regev O.: Visualization of single-wall carbon nanotube (SWNT) networks in conductive polystyrene nanocomposites by charge contrast imaging. Ultramicroscopy, **104**, 160–167 (2005).
DOI: 10.1016/j.ultramic.2005.03.007

[36] Li W., Buschhorn S. T., Schulte K., Bauhofer W.: The imaging mechanism, imaging depth, and parameters influencing the visibility of carbon nanotubes in a polymer matrix using an SEM. Carbon, **49**, 1955–1964 (2011).
DOI: 10.1016/j.carbon.2010.12.069

[37] Deng H., Bilotti E., Zhang R., Peijs T.: Effective reinforcement of carbon nanotubes in polypropylene matrices. Journal of Applied Polymer Science, **118**, 30–41 (2010).
DOI: 10.1002/app.30783

[38] Pantea D., Darmstadt H., Kaliaguine S., Roy C.: Electrical conductivity of conductive carbon blacks: Influence of surface chemistry and topology. Applied Surface Science, **217**, 181–193 (2003).
DOI: 10.1016/S0169-4332(03)00550-6

eXPRESS Polymer Letters Vol.6, No.2 (2012) 169–176
Available online at www.expresspolymlett.com
DOI: 10.3144/expresspolymlett.2012.18

Formation mechanism of porous hollow SnO_2 nanofibers prepared by one-step electrospinning

X. Xia[1,2], *X. J. Dong*[1], *Q. F. Wei*[1*], *Y. B. Cai*[1], *K. Y. Lu*[3]

[1]Key Laboratory of Eco-textiles, Jiangnan University, 214122 Wuxi, People's Republic of China
[2]Xinjiang University, Xinjiang, 830046 Wulumuqi, People's Republic of China
[3]State Key Laboratory of Food Science and Techology, 214122 Wuxi, People's Republic of China

Received 27 June 2011; accepted in revised form 16 September 2011

Abstract. The present study investigates the formation mechanism of hollow SnO_2 nanofibers and the form of nanograin growth in nanofibers. SnO_2 hollow nanofibers were fabricated by directly annealing electrospun polyvinylpyrrolidone (PVP)/Sn precursor composite nanofibers. In this approach, an appropriate proportion of PVP/Sn precursor with co-solvents established a system to form core/shell PVP/Sn precursor structure, and then PVP was decomposed quickly which acted as sacrificial template to keep fibrous structure and there existed a Sn precursor/SnO_2 concentration gradient to form hollow SnO_2 nanofibers due to the Kirkendall effect and surface diffusion during the calcination process. This deduction was also confirmed by experimental observations using transmission electron microscopy. The study suggested that surface diffusion and lattice diffusion were both driving force for nanograin growth on the surface of SnO_2 nanofibers. As supporting evidence, the tetragonal rutile SnO_2 hollow nanofibers were also characterized by X-ray diffraction, scanning electron microscopy and Brunauer–Emmett–Teller analysis.

Keywords: *nanomaterials, SnO_2, hollow nanofiber, electrospinning, Kirkendall effect*

1. Introduction

SnO_2 is an oxide semiconductor with many applications in the areas of sensors [1, 2] and optoelectronic devices [3, 4]. The properties of SnO_2 in various forms such as nanoparticles [5], nanowires [6], nanobelts [7] and other one-dimensional nanostructures have been extensively studied. In comparison with solid one-dimensional nanomaterials, nanotubes gain the advantages in practical applications to catalysts and gas sensors, owing to their higher surface-to-volume ratio. Generally, the conventional methods for preparing SnO_2 nanotubes by self-assembly [8] and templates directed process [9] often suffer from strict synthesis conditions or tedious procedures. Electrospinning has been considered as a simple and efficient method for fabricating nanofibers including organic and inorganic materials. However, templates and the co-electrospinning technique [10] had to be used for forming inorganic nanotubes. Herein, one-step method for the fabrication of SnO_2 hollow nanofibers by directly annealing electrospun composite nanofibers was proposed in this work. Though Cheng *et al.* and Li's group have reported the fabrication of hollow TiO_2 nanofibers [11] and porous SnO_2 nanofibers [12] by the similar technique, respectively; there has been no report about the detailed analysis on the formation mechanism and the growth behavior of nanograins on the nanofiber surface. Generally, the formation mechanism of hollow nanofibers which were fabricated via the electrospinning process, followed by heat treatment is attributed to the decomposition of sacrificial template of organic polymer at the high temperature.

*Corresponding author, e-mail: qfwei@jiangnan.edu.cn

In this work, a systematic investigation into the structures of as-spun nanofiber, the effect of calcination and crystallite growth was conducted for understanding the formation mechanism of SnO_2 hollow nanofibers. In addition, the growth kinetics SnO_2 nanograin in individual nanofiber was also proposed.

2. Experimental

2.1. Preparation of porous hollow SnO_2 nanofibers

Stannic chloride pentahydrate ($SnCl_4 \cdot 5H_2O$), ethanol and N,N-dimethylformamide (DMF) were purchased from Sinopharm Chemical Reagents Co., Shanghai, China. Polyvinylpyrrolidone (PVP, M_w = 1300 000 g·mol^{-1}) was supplied by Qi Fuqin Materials Technology Co., LTD. Shanghai, China. Transparent spinning solution was prepared by adding 3 g of $SnCl_4 \cdot 5H_2O$ into 10 wt% PVP in ethanol/DMF solvent mixture (weight ratio 1:1), and the weight ratio of PVP and $SnCl_4 \cdot 5H_2O$ was also 1:1, followed by magnetic stirring at ambient temperature. Subsequently, the solution was electrospun from the stainless steel needle with an electrostatic voltage of 18 kV, and formed a fibrous mat on a collector of aluminum foil. The distance between the needle and collector was 22 cm. The electrospun fibers were then calcinated at 600°C for 3 hrs with a heating rate of 0.5°C/min.

2.2. Structural observations

The structures of the electrospun nanofibers were observed by a scanning electron microscope (SEM; Hitachi S-4800, Japan) and a high-resolution transmission electron microscope (TEM; JEOL-2100, Japan). The electrospinning specimens were sputter coated with gold before SEM observation, while the SnO_2 nanofibers were examined without any further treatment. For TEM observation, the electrospun composited nanofibers were directly collected on the copper grids for about 30 seconds during electrospinning, while the SnO_2 nanofibers were dispersed ultrasonically in ethanol, and then transferred onto copper grids before TEM observation.

2.3. XRD and TGA analyses

The crystal structure analysis was performed on D8 Advance X-ray diffraction (Bruker AXS, Germany), over the 2θ range of 10–80º. Thermogravimetric studies were carried out using an SDT 851 thermal analyzer system (Mettler, Germany) at a heating rate of 10°C/min.

2.4. Surface area measurement

The porosity and specific surface areas of the electrospun fibers were measured by N_2 adsorption-desorption isotherm at 77 K with a Micromeritics NOVA2000e apparatus (Quantachrome, America).

3. Results and discussion

3.1. Structure observations

Figure 1 demonstrates the morphologies of the electrospun nanofibers before and after calcination at 600°C. The as-spun PVP/SnO_2 nanofibers have a variable diameter ranged between 50 and 300 nm and form a self-supporting network, as shown in Figure 1a. The TEM image clearly reveals the core-shell structure with clear boundary of a phase sepa-

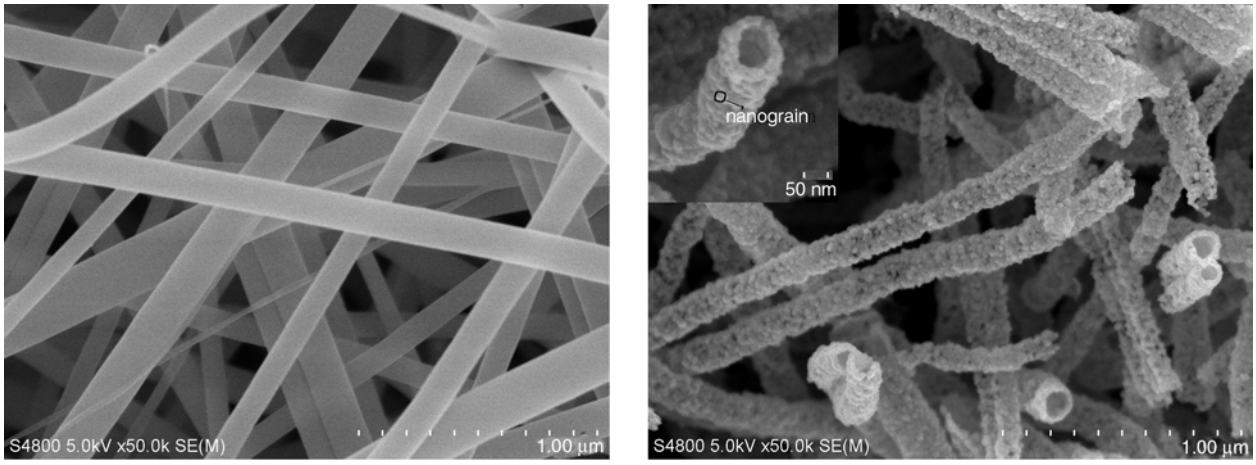

Figure 1. SEM images of (a) as- spun PVP/SnO_2 nanofibers (b) porous hollow SnO_2 nanofibers after calcination at 600°C

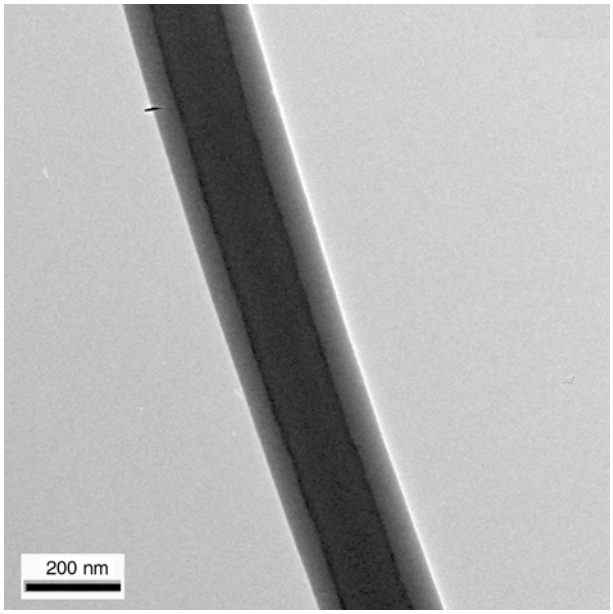

Figure 2. TEM images of as-spun PVP/SnO_2 nanofibers at room temperature

ration between PVP and Sn precursor, as presented in Figure 2.

Figure 1b shows the image of SnO_2 nanofibers obtained by the calcination treatment of as-spun core-shell PVP/SnO_2 nanofibers. It can be clearly seen that these fibers have a tubular structure with dense shells, which consist of nanograins of approximately 17 nm in diameter, as revealed in Figure 1b. Besides SnO_2 nanofibers have a relatively uniform diameter, the outer diameter of the hollow fibers is decreased compared to that of the as-spun PVP/SnO_2 fibers shown in Figure 1a.

3.2. Formation of porous hollow SnO_2 nanofibers

The forming process of hollow SnO_2 nanofibers experiences 5 stages during electrospinning and calcination. Based on the TEM observations combined TGA/DTGA analysis, the formation process of SnO_2 nanofibrous structures can be traced. At the initial stage during electrospinning, the core-shell fibers are fabricated via single capillary electrospinning from homogeneous polymer-sol-double solvents system due to solvent evaporation and rapid phase separation [13]. Various factors may have strong influences on the morphology of the electrospun fibers due to the complexity of hydrolysis and condensation reactions during the gelation of sol as well as the process of fiber formation. The hydrolysis reaction of $SnCl_4$ in water is schematically illustrated in Figure 3. In this work, excessive ethanol was applied to prepare Sn precursor but insufficient H_2O was used to make it partially hydrolyzed. Thus, the polymerization and polycondensation reactions of tin dioxide could be limited to a very low level. Furthermore, a kind of more volatile solvent ethanol evaporates rapidly at the edge of the fiber and a contrary concentration gradient of ethanol and DMF along the radial direction of the fiber will be formed during electrospinning. Especially, ethanol, the 50% weight ratio of solvents, which was used for preparation tin alkoxide, on the surface of the fibers is too little to form large solvent-rich regions during the phase separation because of the rapid evaporation. The high molecular weight PVP and high concentration solution contribute to retain less ethanol to form porous surface as well. So the smooth and compact surface without any porous structures can be observation by TEM, as revealed in Figure 2. At the same time, Sn precursor in nature has a very much higher solubility in ethanol than in PVP [14]. So, it would diffuse from the surface to the core of the fiber. As a result, Sn precursor tends to congre-

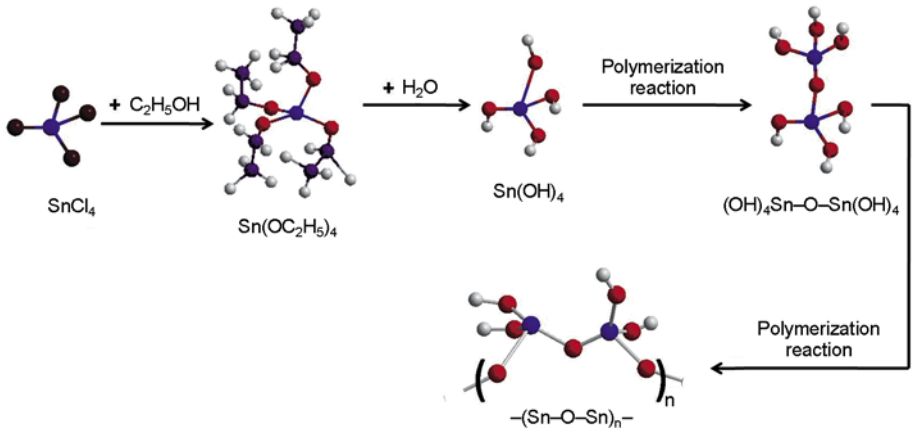

Figure 3. Schematic illustration of the hydrolytic–polymeric reaction of $SnCl_4 \cdot 5H_2O$. Tin, blue; oxygen, red; carbon, purple; hydrogen, white; chlorine, brown.

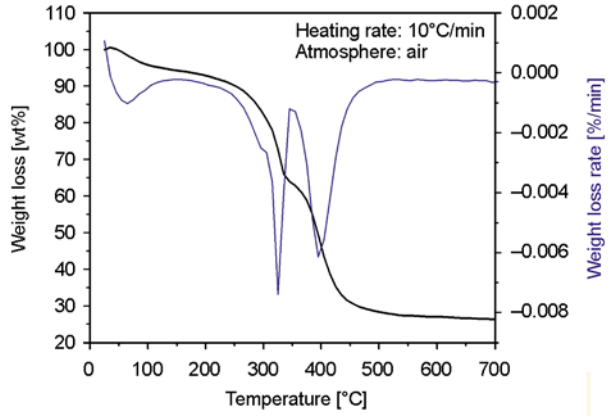

Figure 4. TGA-DTGA graph of thermal decomposition of electrospun PVP/SnO_2 composite nanofibers

gate at the center of the fiber by the driving force of the concentration gradient of ethanol, resulting in a clear core/shell structure.

At the second stage, the first weight loss stage which coincides with the decomposition of PVP chain at the temperature around 280 to 330ºC occurs [15], as shown in Figure 4. The core-shell nanofibers still exist though the diameter of fiber decreases and the boundaries between core and shell are blurred, as indicated in Figure 5a. Eventually, the core-shell structure disappears after the second endothermic peak from 350–480ºC (Figure 4) due to the almost complete decomposition of PVP, in which the process

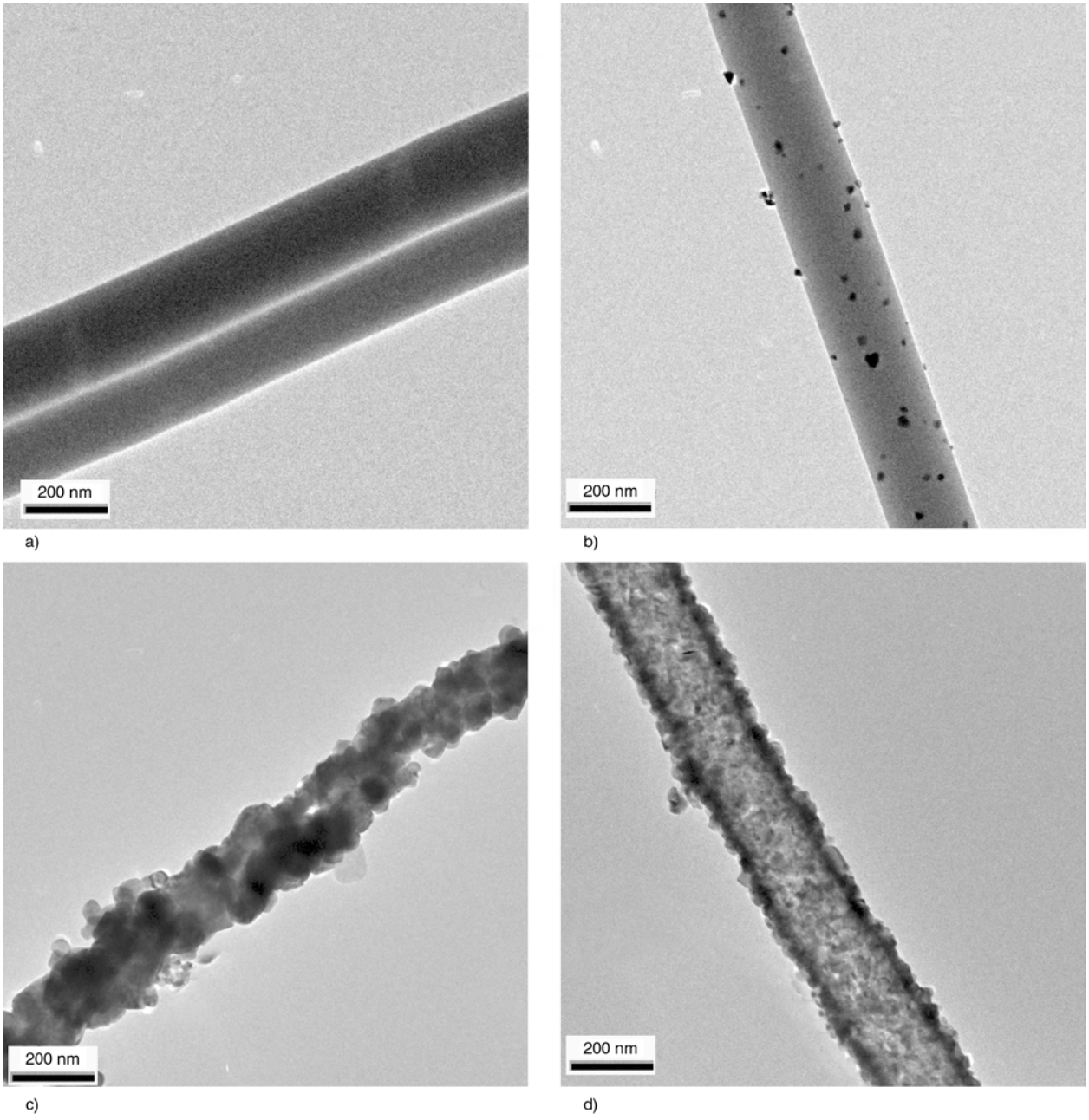

Figure 5. TEM images of PVP/SnO_2 nanofibers (a) calcined at 300ºC, (b) calcined at 400ºC, (c) calcined at 500ºC, (d) calcined at 600ºC

enters the third stage. At this stage, the Sn precursor on the surface region of the electrospun nanofibers is exposed to air, leading to the decomposition and oxidation of the precursor and resulted in the formation of SnO_2. Thus some small SnO_2 particles are presented on the surface whereas most Sn precursor inside the fibers remains unreacted due to the absence of oxygen, leading to solid fiber structure with particles on surface, as illustrated in Figure 5b. When the forming process enters the fourth stage which is a complicated transformation process including grain formation, grain growth and grain reorganization. Figure 5c may be one of morphological situation during this process. Nanograins are the main components to build solid body though the fibers appear to be irregular. Finally, the hollow SnO_2 nanofibers are formed with porous nanograins on the shell, as shown in Figure 5d

According to TEM observations of the hollow SnO_2 nanofibers formation, it is clearly revealed that PVP and Sn precursor are the main constituents of core-shell as-spun nanofibers. Then PVP is gradually decomposed during the calcination process. In this process, PVP plays the role of sacrificial template, which is the key effect to maintain fibrous structures. The decomposition of PVP, to some extent, reduces the final fiber diameters. The key mechanism responsible for the formation of hollow nanofibers is attributed to the interaction between Sn precursor and SnO_2 which will be discussed in the next section.

3.3. Analysis of formation mechanism

As mentioned above, the main components after the complete decomposition of PVP are some SnO_2 particles on the surface region and the massive Sn precursors in the core to form a concentration gradient, which lead to a Kirkendall effect [16]. Kirkendall effect is associated with the phenomenon of a considerable amount of compounds moving in or out of a sphere due to the diffusion coupled with different diffusion rates [17]. When the solid fiber consists of Sn precursor and SnO_2 (Figure 6a), the outward transport of fast-moving Sn precursor molecules (short as J_a in Figure 6) move through the oxide layer and a balancing inward flow of vacancies traverse to the vicinity of the Sn precursors and Sn precursors/SnO_2 mixture interface (*a*/*ab* interface) and vacancies assisted exchange of material depends on the way of bulk inter-diffusion, as illustrated in Figure 6b. Then, the voids are just like sinks to transfer the inward flux of vacancies ($J_c = J_a - J_b$) and the voids coalesce into bigger ones so as to touch the compound layer *ab*. Such new bridges are established as fast transport paths for the remaining Sn precursors (Figure 6c). At this stage, the surface diffusion takes over the dominant material transport process because the porous surface owns much lower apparent activation energy than those of bulk diffusion [18]. Sn precursors can be quickly oxidized at the surface of ab layer and redistribute themselves via fast surface diffusion, while the ab layer remains bulk inter-diffusion associated with Kirkendall effect until the whole Sn precursors turn into SnO_2. Therefore, SnO_2 stands on the shell and vacancies are continuously generated and flow inward to build a hollow core, as shown in Figure 6d. In all, the fibrous structure is established by PVP template and Kirkendall effect contributions to form hollow structure. Furthermore, surface diffusion also plays an important role to build hollow fibers.

The surface diffusion is also beneficial to the nano-sized grains growth. In the experiments, the annealing time (≤4 hrs) obeys the parabolic kinetic equation of grain growth for isothermal annealing as Equation (1):

$$D^m - D_0^m = Kt \tag{1}$$

where t is the annealing time, D is the average grain size after annealing for time t, D_0 is the initial grain size, m is the grain growth exponent, and K is a temperature dependent rate constant $=1.04 \cdot 10^{13}$ at 600ºC [19].

The average grain size after 3 hrs calcination is obtained by calculating the size of three intense peaks, (110), (101) and (211) of SnO_2 from XRD

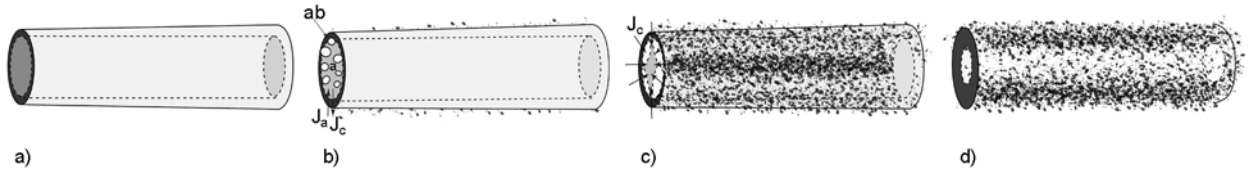

Figure 6. The model for hollow structure formation of SnO_2 nanofibers (see text for details)

patterns. When D_0 is neglected, the estimated m value is 13.2, which is inconsistent with the classical grain growth value (m = 2~4) [20], which means the grain growth of the nanograins observed in the individual nanofibers cannot be primarily ascribed by lattice diffusion in a pore controlled scheme. When the new bridges are established to transport the mass materials as mentioned above, the connection for lattice diffusion are broken and surface diffusion will enhance the local voids, meanwhile acts as the driving force for grain growth, leading to acceleration in the speed of coarse grains by the reduction of the free energy of the system. However, the growth kinetics of nanograins in hollow SnO_2 fibers is complicated and needs further investigation. Heating rate should be studied to control the morphology of fibers while using the temperature and duration of calcination as a tool to obtain desired nanograins on nanofiber surfaces have already been reported by Park *et al*. in Ref [20].

XRD patterns in Figure 7 confirm the formation of SnO_2 fibers. The fibers after calcination at 300ºC show a broad continuum indicating that the crystallization of tin oxide just starts at this temperature but not sufficient enough to produce the diffraction patterns. However, the XRD patterns of the fibers after calcination at 400ºC show the emergence of tetragonal rutile tin oxide crystals with distinct peaks due to the decomposition of PVP and oxidation of some Sn precursors on the fiber surface. The diffraction peaks become much sharper and well defined after calcination at 500 and 600ºC, without altering their positions but with high intensity because of better crystallization. All the diffraction peaks are indexed to the tetragonal rutile SnO_2, the only crystalline phase existing in the obtained nanofibers.

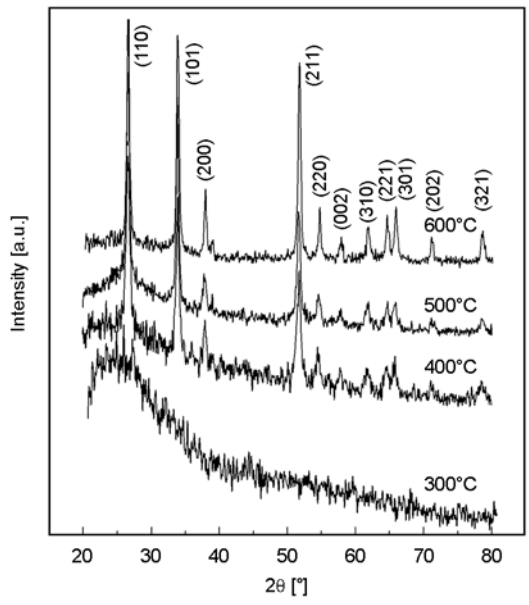

Figure 7. XRD patterns of SnO_2 nanofibres at different temperature

3.4. Surface areas

Brunauer–Emmett–Teller (BET) gas sorption measurement reveals the surface area of the hollow SnO_2 fibers. The N_2 adsorption–desorption isotherm curve of the porous SnO_2 fibers is shown in Figure 8. It exhibits the characteristic of mesopore structures, especially even owns an adsorption at high P/P_0, which was also reported as an aggregation of plate-like particles giving rise to slit-shaped pores [21]. The porous structure is confirmed by the SEM observations shown in Figure 1b. The average pore size in the porous SnO_2 fibers is approximately 16.2 nm, and the corresponding BET specific surface area is about 35.8 m^2/g (BJH method).

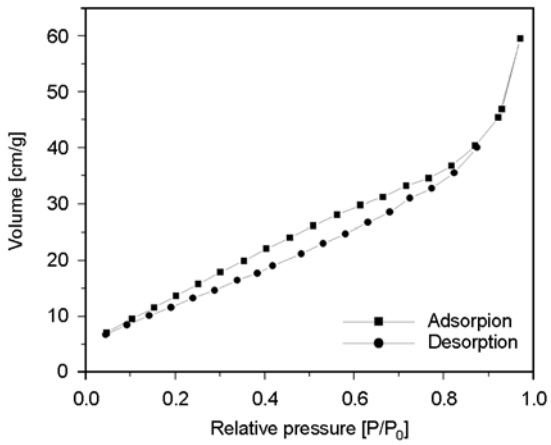

Figure 8. Nitrogen adsorption/desorption isotherms of the hollow SnO_2 nanofibers

4. Conclusions

In this work, porous hollow SnO_2 nanofibers were successfully prepared by electrospinning technique via a single capillary from PVP/Sn precursors/dual solvents system with calcination treatment. During the electrospinning process, a stringent component matching contributes to core-shell structure which provided advantages for preserving fibrous structures based on sacrificial PVP template. Hollow structures initiated by the Kirkendall effect owing to the concentration gradient of Sn precursors and SnO_2, suggesting that surface diffusion processes

might be the dominant mass flow mechanism responsible for the enlargement of the interior pores after initially formation induced by the Kirkendall effect. This deduction was also confirmed by the calculated grain growth value which was higher than the classical one, which means the grain growth mechanism occurred not only by the lattice diffusion but also through surface diffusion. This mechanism should also apply to the synthesys of other hollow nanofibers. The technique described here will be extendible to many other materials for fabricating such hollow inorganic nanofibers with potential applications in catalysis, microelectronics, and optics.

Acknowledgements

The research was supported by the specialized Research Fund for the Doctoral Program of higher education (No.20090093110004) and National Natural Science Foundation of China (No.51006046 and No.51163014).

References

[1] Song X., Qi Q., Zhang T., Wang C.: A humidity sensor based on KCl-doped SnO_2 nanofibers. Sensors and Actuators B: Chemical, **138**, 368–373 (2009). DOI: 10.1016/j.snb.2009.02.027

[2] Zhang Y., Li J. P., An G. M., He X.: Highly porous SnO_2 fibers by electrospinning and oxygen plasma etching and its ethanol-sensing properties. Sensors and Actuators B: Chemical, **144**, 43–48 (2010). DOI: 10.1016/j.snb.2009.10.012

[3] Zhang Z., Shao C., Li X., Zhang L., Xue H., Wang C., Liu Y.: Electrospun nanofibers of ZnO–SnO_2 heterojunction with high photocatalytic activity. Journal of Physical Chemistry C, **114**, 7920–7925 (2010). DOI: 10.1021/jp100262q

[4] Yang Z., Du G., Feng C., Li S., Chen Z., Zhang P., Guo Z., Yu X., Chen G., Huang S., Liu H.: Synthesis of uniform polycrystalline tin dioxide nanofibers and electrochemical application in lithium-ion batteries. Electrochimica Acta, **55**, 5485–5491 (2010). DOI: 10.1016/j.electacta.2010.04.045

[5] Gong S., Liu J., Xia J., Quan L., Liu H., Zhou D.: Gas sensing characteristics of SnO_2 thin films and analyses of sensor response by the gas diffusion theory. Materials Science and Engineering B: Advanced Functional Solid-State Materials, **164**, 85–90 (2009). DOI: 10.1016/j.mseb.2009.07.008

[6] Xu L., Dong B., Wang Y., Bai X., Liu Q., Song H.: Electrospinning preparation and room temperature gas sensing properties of porous In_2O_3 nanotubes and nanowires. Sensors and Actuators B: Chemical, **147**, 531–538 (2010). DOI: 10.1016/j.snb.2010.04.003

[7] Soares A. J., Perry R. J.: Modeling and simulation of a single tin dioxide nanobelt FET for chemical sensors. IEEE Sensors Journal, **10**, 235–242 (2010). DOI: 10.1109/JSEN.2009.2032154

[8] Qiu Y., Chen P., Liu M.: Evolution of various porphyrin nanostructures via an oil/aqueous medium: Controlled self-assembly, further organization, and supramolecular chirality. Journal of the American Chemical Society, **132**, 9644–9652 (2010). DOI: 10.1021/ja1001967

[9] Park J. Y., Choi S-W., Kim S. S.: A synthesis and sensing application of hollow ZnO nanofibers with uniform wall thicknesses grown using polymer templates. Nanotechnology, **21**, 475601 (2010). DOI: 10.1088/0957-4484/21/47/475601

[10] Chen H., Wang N., Di J., Zhao Y., Song Y., Jiang L.: Nanowire-in-microtube structured core/shell fibers via multifluidic coaxial electrospinning. Langmuir, **26**, 11291–11296 (2010). DOI: 10.1021/la100611f

[11] Cheng Y., Huang W., Zhang Y., Zhu L., Liu Y., Fan X., Cao X.: Preparation of TiO_2 hollow nanofibers by electrospining combined with sol–gel process. CrystEngComm, **12**, 2256–2260 (2010). DOI: 10.1039/b922564a

[12] Li L., Yin X., Liu S., Wang Y., Chen L., Wang T.: Electrospun porous SnO_2 nanotubes as high capacity anode materials for lithium ion batteries. Electrochemistry Communications, **12**, 1383–1386 (2010). DOI: 10.1016/j.elecom.2010.07.026

[13] Zhang K., Wang X., Yang Y., Wang L., Zhu M., Hsiao B., Chu B.: Aligned and molecularly oriented semihollow ultrafine polymer fiber yarns by a facile method. Journal of Polymer Science Part B: Polymer Physics, **48**, 1118–1125 (2010). DOI: 10.1002/polb.22003

[14] Wang W., Zhou J., Zhang S., Song J., Duan H., Zhou M., Gong C., Bao Z., Lu B., Li X., Lan W., Xie E.: A novel method to fabricate silicananotubes based on phase separation effect. Journal of Materials Chemistry, **20**, 9068–9072 (2010). DOI: 10.1039/C0JM02120B

[15] Loría-Bastarrachea M. I., Herrera-Kao W., Cauich-Rodríguez J. V., Cervantes-Uc J. M., Vázquez-Torres H., Ávila-Ortega A.: A TG/FTIR study on the thermal degradation of poly(vinyl pyrrolidone). Journal of Thermal Analysis and Calorimetry, **104**, 737–742 (2010). DOI: 10.1007/s10973-010-1061-9

[16] Yin Y., Rioux R. M., Erdonmez C. K., Hughes S., Somorjai G. A., Alivisatos A. P.: Formation of hollow nanocrystals through the nanoscale Kirkendall effect. Science, **304**, 711–714 (2004).
DOI: 10.1126/science.1096566

[17] Kong J., Tan H. R., Tan S. Y., Li F., Wong S. Y., Li X., Lu X.: A generic approach for preparing core–shell carbon–metal oxide nanofibers: Morphological evolution and its mechanism. Chemical Communications, **46**, 8773–8775 (2010).
DOI: 10.1039/C0CC03006F

[18] Fan H. J., Knez M., Scholz R., Hesse D., Nielsch K., Zacharias M., Gösele U.: Influence of surface diffusion on the formation of hollow nanostructures induced by the Kirkendall effect: The basic concept. Nano Letters, **7**, 993–997 (2007).
DOI: 10.1021/nl070026p

[19] Lai J. K. L., Shek C. H., Lin G. M.: Grain growth kinetics of nanocrystalline SnO_2 for long-term isothermal annealing. Scripta Materialia, **49**, 441–446 (2003).
DOI: 10.1016/S1359-6462(03)00296-3

[20] Park J. Y., Asokan K., Choi S-W., Kim S. S.: Growth kinetics of nanograins in SnO_2 fibers and size dependent sensing properties. Sensors and Actuators B: Chemical, **152**, 254–260 (2011).
DOI: 10.1016/j.snb.2010.12.017

[21] Sing K. S. W., Everett D. H., Haul R. A. W., Moscou L., Pierotti R. A., Rouquérol J., Siemieniewska T.: Reporting physisorption data for gas/solid systems with special reference to the determination of surface area and porosity. Pure and Applied Chemistry, **57**, 603–619 (1985).
DOI: 10.1351/pac198557040603